

國立交通大學  
物理研究所  
碩士論文

量子點在高壓下的發光效應和量子點模型  
建構

Modeling and high pressure experiment of  
CdSe/ZnS Colloidal QDs

研究生：邱奎霖

指導教授：褚德三

民國九十五年六月二日

# 量子點在高壓下的發光效應和量子點模型建構

學生：邱奎霖

指導教授：褚德三

國立交通大學物理研究所

## 摘要

本論文主要是研究膠狀的複層量子點，核為 CdSe 外殼為 ZnS，在高壓下的發光效應，實驗是量測量子點的 Raman, PL, 和 life time 光譜。從這些光譜中我們研究量子點能階隨壓力的變化、晶體結構隨壓力可能之改變，以及量子光學理論對於這種介於原子和固體中間之尺度的量子點之適用程度。

從拉曼和 PL 光譜中我們發現量子點也存在壓力所引起的相變點，但由於外層 ZnS 的保護，使得它的相變壓力比起塊材的相變壓力(3GPa)來的大，要到 7GPa 才會相變。而由於相變後 PL 不存在也讓我們猜測相變後的內層 CdSe 是呈金屬相，即如同塊材 CdSe 相變後的 rocksalt 結構，由第一原理計算知道其導帶與價帶重疊因而為金屬相。而從退壓拉曼我們發現當壓力又小於 7GPa 時，CdSe LO 譜峰會重現但 2LO 模卻消失，因此我們也猜測 CdSe 經過一次相變後就算壓力回覆仍然不能回到之前的相；即這個相變是不可逆相變。而 ZnS 的 LO 模加壓退壓曲線幾乎重合，因此可知，此複層量子點的 ZnS 殼僅僅隨壓力而壓縮而未發生相變。

我們也由 PL 光譜佐以拉曼光譜來研究量子點能隙隨著壓力的變化。我們知道量子點隨著加壓除了電子結構改變所引起的能階改變外，仍有電子-聲子的交互作用能量(polaron 能量)的貢獻，而經由拉曼 CdSe 的 LO, 2LO 模的 Grüneisen 參數顯示晶體的離子性會隨壓力降低，這會減低 polaron 形成的能力，也會減低電子-聲子的交互作用能量。故我們可以預期隨著加壓，量子點的 polaron 能量會降低，所以再高壓時，能階曲線會呈現較為平滑的趨勢。我們也在第三章對這個現象做一個簡單模型的討論。

至於量子點輻射的時間解析部分，我們結合量子光學中一個理想二能階原子的輻射衰退率公式，和在塊材中加一個侷限位勢的量子點模型，並利用費米黃金定律所解出之受激輻射衰退率公式。利用這兩種理論的結合來討論我們所作到的 life time 光譜在加壓中可能會有什麼趨勢。基本上我們懷疑再加壓過程中隨著電子結構改變的電子等效質量會對輻射衰退率有所影響。這個模型也在第三章會做

一些說明。

另外學生由一篇 PRL 的第一原理計算論文,我們建立了量子點模型的幾何方法,利用幾何原理發展出新的建立量子點結構的方法,可以得出由切割塊材維持一樣的外型但尺寸由小變大的 CdSe 量子點。且我們找到 CdSe 量子點結構的一些限制(可能只存在切割塊材的結構)。

這些建構量子點模型的工作都是爲了將來可能要計算隨著加壓量子點結構變化所引起的能階改變,目前已經能算 CdSe 塊材的加壓電子結構改變,但由於量子點的計算需要破壞計算平台的週期性輸入,使得計算量大增,故將此工作視爲將來工作的延伸。以後若能完成此部分工作將對許多由電子結構改變所引起的能階變化有更精準的處理方法(而不是帶入塊材的參數),此爲此部分工作的重要性。這些建構量子點模型的方法,以及第一原理計算的一些背景理論都在第四章有一介紹,第四章末則是原子輻射衰退率的量子光學導證。

第五章則是我們的工作的總結和未來的展望。



# Modeling and high pressure experiment of CdSe/ZnS Colloidal QDs

Student : Kui-Lin Chiu

Advisor : Der-San Chuu

Institute of Physics  
Nation Chiao-Tung University

## ABSTRACT

In this thesis we study the Raman, PL and time resolve spectrum of the colloid core/shell CdSe/ZnS quantum dot under high pressure. From our experiment result, we want to find out the curve of the energy band gap of QD versus pressure, and the possible structure of QDs under high pressure. Finally, we also want to verify the quantum optic theorem by our time resolve experiment.

From the Raman and PL spectrum of QDs, we find that QD exist the pressure induced phase transition which is at 7GPa than bulks (3GPa). Due to the bigger bulk modulus of ZnS (75GPa for ZnS, 53GPa for CdSe), we reasonably deduce this retarded phase transition is coming from the “pressure screen effect” of ZnS.

When the pressure is less than 7GPa in unloading pressure process, we find the LO mode of CdSe in Raman spectrum reappear again while the 2LO mode of CdSe remain disappeared. This deduces that the phase transition is an irreversible one. The LO mode of ZnS in Raman spectrum while loading pressure is consistent to the curve of unloading process. From this we believe that the lattice constant of ZnS may only be compressed/relaxed while loading/unloading pressure.

We also study the contribution of polaron effect in energy band gap at high pressure. This pressure induced polaron effect is independent of the shift in  $E_g$  induced by structure difference under high pressure and is correlated to the ionicity of lattice. By analyzing the Grüneisen parameter in Raman spectrum, we find that the lattice become more and more covalent with loading pressure, and this will decrease the electron-phonon interaction, thus reduce the polaron energy. This can explain why the

pressure dependence of  $E_g$  becomes non-sensitive in high pressure. All the discussion will be explained in chapter3.

In the time resolved spectrum study, we will combine a formula of spontaneous radiative decay rate in a two level atom and a formula of stimulated decay in QD to predict the pressure dependence of our time resolved spectrum. Actually we doubt that the effective mass of electron will be changed in loading pressure and this effect may influence the slope of decay rate/ $E_g^3$  in loading process.

Finally we study the possible model of QD by following a PRL paper. We find out some constrains of constructing the model of zinc-blende QD. We also develop a method to construct QD with the same shape but size from small to big.

These works of modeling QD are for the purpose of first-principle calculation. We wish to study the band edge shift induced by the structure change of QD at high pressure by first-principle calculation. However, the calculation in QD needs a large order of computation volume due to the destruction of lattice periodicity. For this reason I regard this job as an extended work. All the works for model are put in chapter4 and chapter5 is the conclusion and further work.



# 誌謝

很快的兩年時間過去了,意味著從母校嘉義大學畢業的時間也已經兩年了。當初在大學要找研究所老師時因為羅光耀系主任的一句:你想做理論?那找褚老師就對了!順便學習一下長者的風範。於是我進入了褚老師的實驗室,也開啓了我在交大的兩年充實的生活。

要感謝的人事物實在很多,首先要謝謝褚老師在這兩年中常常鼓勵我,並且在身教言教上常常為我們學生的典範!猶記得剛找老師做研究時,自己常常很急躁,凡事都想獲得立即的成效;老師那時就提醒我:不要急,慢慢來,物理是很有趣的,你要懂得享受物理。(那一陣子,“享受物理”這四個大字就出現在我的牆壁上~)說起來我高中轉組自修物理時唸的也是老師編的教科書,原來我在高中就受惠於老師了!(並且也是由那時候確定將來要唸物理)也要感謝老師讓我再做實驗之餘還能讓我轉做理論,使我的碩士論文有實驗有理論,並且學到了不少東西,而且研究做得很快樂!

也感謝我們實驗室的另一位周武清老師,感謝周老師在實驗上的意見及提供的學術資源。

接下來要感謝我的實驗室學長姐和同學。謝謝裕煌學長,你總是很照顧學弟妹,每次有問題你總是不留餘力的幫我們解決。也要謝謝你常常戴我們實驗室大夥出遊。高進學長,謝謝你的網球,另外我很佩服你在物理上的執著。岳男學長,厲害的理論實力就不用說了,更要謝謝你給我的建議和在理論上的幫忙。繼組和彥承學長,我們是一起實驗共患難的夥伴,也謝謝你們常為實驗室帶來笑聲,希望你們繼續加油。瑞文學姐,常常受妳照顧了,從碩一以來就發現你人實在很好,希望學姊能順利畢業!英彥學長,學長是一個很古意的人,謝謝你常常鼓勵我。英瓊學長,你是我們研究室最年輕的學長,因為代溝很小所以感覺跟同輩一樣,謝謝你都陪我運動。光胤,謝謝你常常幫助我一些事情,不管是日常上或是研究上。耿榮,謝謝你常常陪我聊天。哲豪,我們是實驗室的好夥伴,那段時間常常彼此加油打氣,也謝謝你常常關心我。

也感謝教我做高壓的竹教大林志明老師,以及第一原理計算的淡江薛宏中老師,有您們在實驗及理論上的協助與幫忙,才能讓我論文能順利的完成,真的十分感謝你們。也要謝謝薛老師實驗室的學長及同學們,尤其是黃冠璋學長,有你的幫忙我才能很快的熟悉 vasp 的操作。

然後感謝我研究所的同學,德明,老皮,老王,等等的人。然後還有我的好室友佳唯,有你這個基督徒室友真的十分棒,感謝你常常鼓勵我給我意見跟我去教會,還常陪我吃飯。

感謝大學的師長以及同學們,你們的教導與幫忙是我很大的助力。

最後感謝一路栽培我的父母,感謝你們在我國高中生命最晦暗的時候支撐

我，你們的鼓勵永遠是我的動力來源。也感謝我的弟弟，總是很快的幫哥哥解決電腦問題。

最後感謝天父上帝,若沒有你的指引,萬事皆不能成！



# Contents

Part I : EXPERIMENT .....	10
Chapter1 : Introduction.....	10
1-1 Introduction of high pressure.....	10
1-2 Introduction of QDs.....	10
1-3 How to produce CdSe/ZnS QD .....	14
1-4 Research motivation .....	14
Chapter2 : Experiment apparatus.....	15
2-1 High pressure technique .....	15
2-1-1 Principle of applying pressure.....	15
2-1-2 Diamond Anvil Cell.....	16
2-1-3 Gasketting, and Pressure Medium.....	18
2-1-4 Pressure Calibration .....	20
2-1-5 The high pressure experiment process .....	21
2-2 Raman scattering experiment .....	23
2-3 PL and photon lifetime spectrum experiment.....	25
2-3-1 Instrument Introduction.....	25
2-3-2 Configuration and Standard Components .....	27
2-3-3 Overview .....	28
Chapter3 : Experiment result and discussion .....	29
3-1 Result .....	29
3-1-1 Raman spectrum.....	29
3-1-2 Photon luminescence.....	35
3-1-3 Photon life time result .....	37
3-2 Discussion.....	41
3-2-1 Raman discussion.....	41
3-2-2 Raman and PL discussion.....	45
3-2-3 Life time discussion .....	49
Part II : THEORETICAL CALCULATION.....	54
Chapter4 : Electrons structure of QD .....	54
4-1 The concept of constructing Diamond structure QD model.....	54



4-1-1 Dodecahedron core.....	55
4-1-2 smallest size tetrahedron cell.....	55
4-1-3 middle size tetrahedron cell.....	56
4-1-4 giant size tetrahedron cell.....	57
4-2 Model a bulk like QD from small to big .....	59
4-3 The introduction of first-principle calculation.....	62
4-3-1 Hatree and Hatree-Focd Equations.....	62
4-3-2 Density Functional Theory .....	65
4-3-3 Kohn-Shan theory and Local Density Approximation (LDA).....	67
4-4 Relation between $E_g$ and photon lifetime .....	68
<b>Chapter5 : Conclusion .....</b>	<b>71</b>
<b>Appendix A : The preparation of non-colloid sample .....</b>	<b>73</b>
<b>Appendix B : Alignment of Raman Scattering System .....</b>	<b>73</b>
<b>Appendix C : The optical element of time resolved system .....</b>	<b>74</b>
Main Optical Unit .....	74
Sample Holder.....	75
Detector .....	75
TCSPCD Data Acquisition.....	75
<b>Appendix D : Construction of the QD model with Zinc-Blend structure.....</b>	<b>76</b>
<b>Reference .....</b>	<b>80</b>

# **Part I : EXPERIMENT**

## **Chapter1 : Introduction**

### **1-1 Introduction of high pressure**

Besides the physical parameter such as temperature and the chemical composition, pressure effect can efficiently decrease the distance between atoms.

In general, high-pressure researches can be mainly classified into two parts.

One is to investigate phenomena that occur only or primarily at high pressure. The other is to gain a better understanding and characterization of matter or processes, which occur at atmosphere pressure. In our purpose, we employ high pressure technique to change the size of quantum dot and its structure to alter the energy band gap to see which might alter the photon lifetime in transmission. Pressure induced phase transition of semiconductor to metal is also important in studying on characteristic of the semiconductor QD. In general, metallic behavior is expected for most semiconductors at high pressures since pressure-induced structural phase transformations occur when the atoms become more closely packed. Although we can not overemphasize the importance in understanding the effects of pressure on structural and electronic properties of semiconductors, however studies of these materials under high pressure are not only interesting but also heuristic. In particular, the pressure-induced structural phase transition from semiconductor to metal is one of the major subjects in theoretical and experimental researches for decades. In order to investigate the novel physical properties of nano-crystal at high pressure, several high-pressure techniques were developed. For instance, thick-walled cylinders, multiple piston apparatus, and high-pressure pistons etc. are all instruments for generating high pressure. Among these technologies, diamond anvil cells (DACs) are usually used.

### **1-2 Introduction of QDs**

QDs, which are only a few nanometers in diameter, exhibit discrete size-dependent energy levels. As the size of the nanocrystal increases, the energy gap decreases, yielding a size-dependent rainbow of colors. Extensive tunability, from ultraviolet to infrared, can be achieved by varying the size and the composition of QDs (**Fig1-1**),

enabling simultaneous examination of multiple molecules and events. For example, small CdSe nanocrystals ( $\sim 2$  nm) emit light with wavelength in the range between 495 to 515 nm, whereas larger CdSe nanocrystals ( $\sim 5$  nm) emit between 605 and 630 nm.

QDs have several dramatically different properties compared to organic fluorophores, one of which is their unique optical spectra. As illustrated in **Fig1-2**, organic dyes typically have narrow absorption spectrum, which means that they can only be excited within a narrow window of wavelengths. Furthermore, they have asymmetric emission spectra broadened by a red-tail. In contrast, QDs have broad absorption spectra, enabling excitation by a wide range of wavelengths, and their emission spectra are symmetric and narrow. Consequently, multicolor nanocrystals of different sizes can be excited by a single wavelength shorter than their emission wavelengths, with minimum signal overlap.

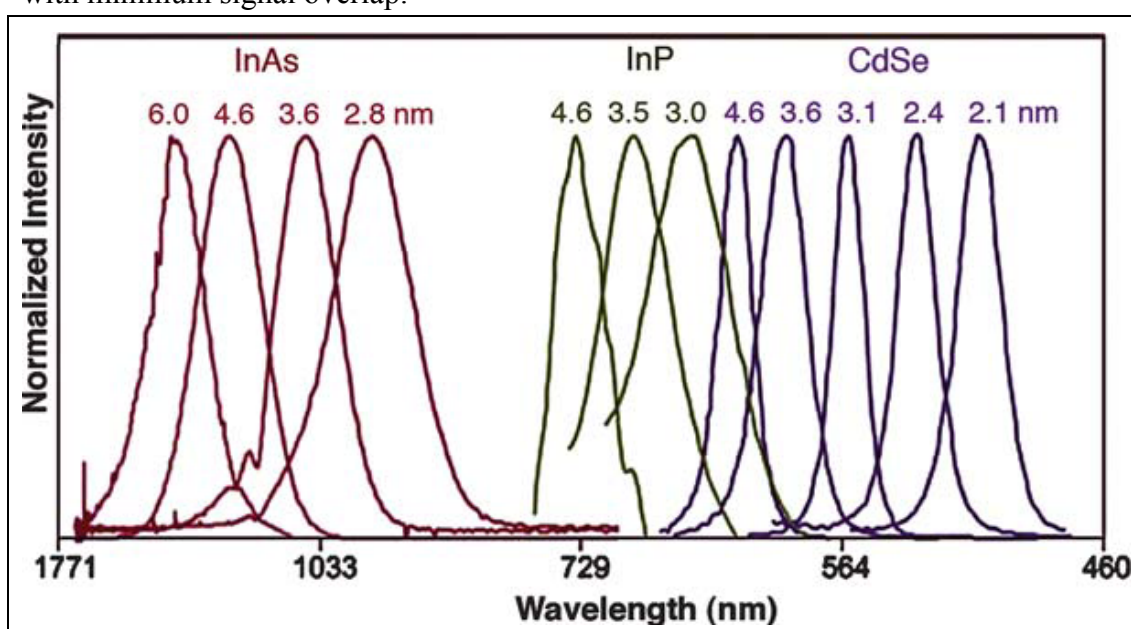


**Figure 1-1** : Emission spectra of several semiconductor nanocrystals showing their size- and composition-dependent emission character. Red, green, and blue series represent different-sized InAs, InP, and CdSe nanocrystals, respectively. The sizes of the nanocrystals are indicated above their corresponding spectra.

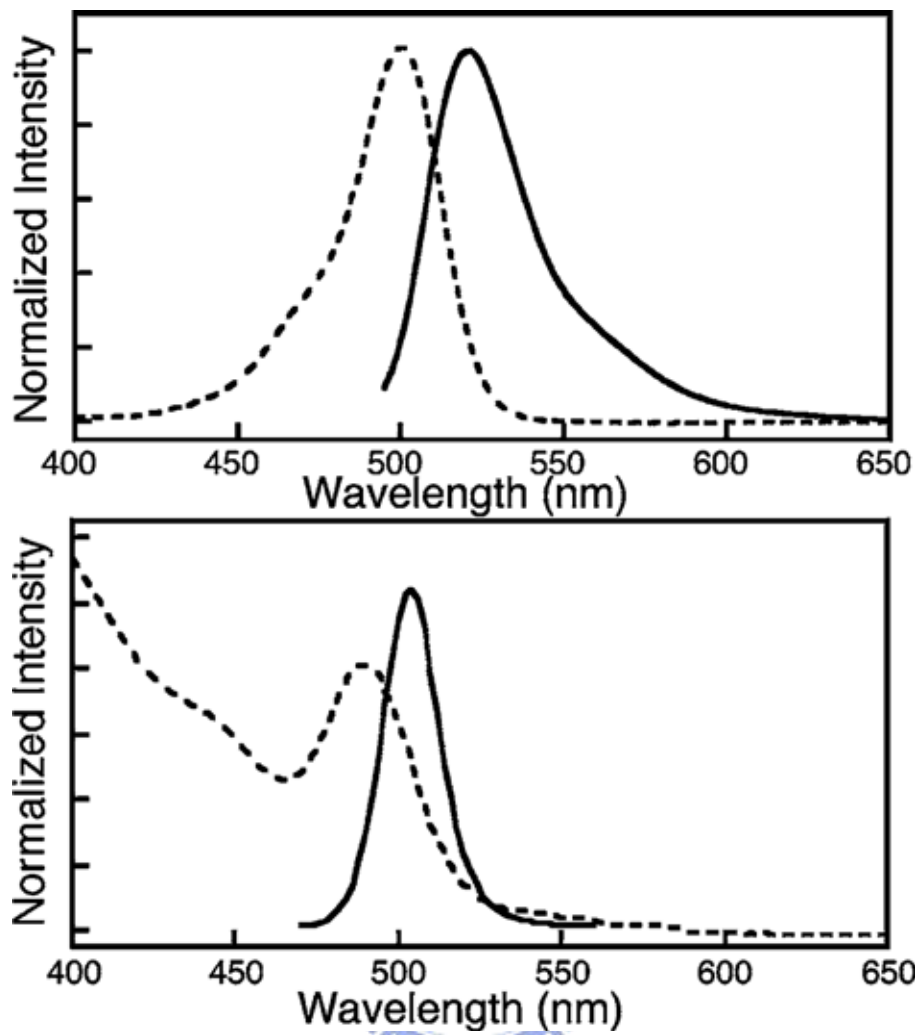


**Figure 1-2** : Excitation (dotted line) and fluorescence (solid line) spectra of fluorescein (top) and a typical water-soluble QD (bottom). The excitation wavelength was 476 nm and 355 nm for fluorescein and QD, respectively.

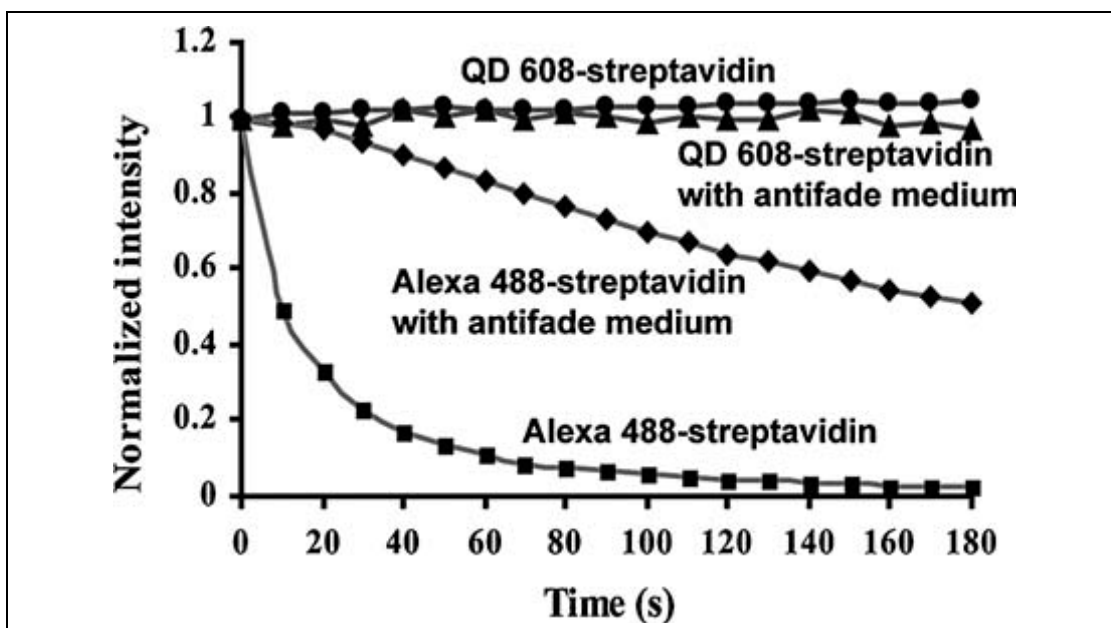


**Figure1-3** : Comparison of fluorescence intensities between QD 608 (emission at 608 nm) and Alexa 488 after continuous illumination.

QDs are stable light emitters owing to their inorganic composition, making them less susceptible to photobleaching than organic dye molecules.

This feature has been demonstrated in a number of biological labeling experiments where the photostability of QDs was compared with commonly used fluorophores, such as rhodamine, fluorescein, and Alexa-Fluor (**Fig1-3**). This extreme photostability makes QDs very attractive as the probes for imaging thick cells and tissues over long time periods—a challenging task that necessitates collection of multiple optical sections without damaging the specimen. In addition, the two-photon cross-section of QDs is significantly higher than that of organic fluorophores, making them quite well suited for examination of thick specimens and in vivo imaging using multiphoton excitation.

Another interesting characteristic of QDs is their fluorescence lifetime of 10 to 40 ns, which is significantly longer than typical organic dyes or auto-fluorescent flavin proteins that decay on the order of a few nanoseconds.

Combined with pulsed laser and time-gated detection, the use of QD labels can produce images with greatly reduced levels of background noise.

There are also some photophysical properties of QDs that can, in some cases, be disadvantageous. One of these is the property referred to as blinking, that is, QDs randomly alternate between an emitting state and a non-emitting state. This intermittence in emission of QDs is universally observed from single dot, which imposes some limitations in QD applications requiring single-molecule detection.

However, there is limited evidence suggesting that QD blinking can be suppressed on some timescale by passivating the QD surface with thiol moieties, or when using QDs in free suspension. It has also been reported that QD fluorescence intensity increases upon excitation, an event referred to as photobrightening. Although in most cases this property can be advantageous, it is problematic in fluorescence quantization studies. Both blinking and photobrightening are linked to mobile charges on the surfaces of the dots, and although the prospects are good that they can be eliminated, for the time being these should be considered as limitations of QDs.

### **1-3 How to produce CdSe/ZnS QD**

The investigated colloidal core/shell CdSe/ZnS QDs were synthesized by the following procedure. 0.30 g of cadmium oxide (CdO), 1.30 g of tetradecylphosphonic acid (TDPA) and 25.0 g of tri-n-octylphosphine oxide (TOPO) were loaded into a 250 mL flask and heated to 320 °C under argon flow. After the CdO was totally dissolved in TDPA and TOPO, the solution was cooled to 300 °C and 4.45 mL of selenium stock solution (0.5 M of selenium solution in tributylphosphine, TOP) was injected. 1.5 mL of precursor solution (made by mixing a 1.75 mL of ZnMe<sub>2</sub> (2.0 M in toluene) and S (Si(CH<sub>3</sub>)<sub>2</sub>)<sub>2</sub> in TBP) was then added drop-wise into the mixture to cover a layer of ZnS. A 20 mg of TOP/TOPO capped CdSe/ZnS QDs was mixed with a 200 mg 11-mercaptopundecanoic acid (MUA) in a reaction vessel to synthesize the carboxylated QDs. Methanol was added and the pH value was adjusted to about ten with tetramethylammonium hydroxide. The mixture was heated under reflux for 2 hours. After it was cooled to room temperature, the resulting water-soluble QDs were precipitated with tetrahydrofuran and separated by centrifugation.

### **1-4 Research motivation**

High pressure technology is one of the important techniques in the study of lattice structures. Our purpose is to study the structure change of QD induced by high pressure. The optical spectrum, ex Raman, PL, and time resolved spectrum were used to study the structure change induced by pressure.

Raman vibration mode presents some knowledge about the lattice composition, the vibration type of atoms and the ionicity or covalency of lattice. The pressure dependence of energy band edge in QDs can be gotten by measuring PL spectrum in high pressure. However, we know the shift of emission wavelength under high

pressure is not only depend on the lattice structure change of QDs induced by the pressure, but also on the contribution of electron-phonon interaction. These all need to be realized by measuring the Raman and PL simultaneously.

Secondly it is interested to realize the mechanism of radiative decay rate in QDs i.e. base on the quantum optics to predict pressure dependence of radiative decay rate of QDs. By the measurement of time resolve spectrum, it is hopeful to verify the theoretical result by our experiment.

Finally we wish to study the band edge shift induced by the structure change of QD at high pressure by first-principle calculation, and hope to find out some possible conclusion in our study.

## **Chapter2 : Experiment apparatus**

In this chapter, we will introduce the experimental set-up and the technique that were used in our experiment. These techniques include : the high pressure technique, Raman Scattering spectrum measurement, photo luminance measurement and time-resolved spectrum measurement

### **2-1 High pressure technique**



#### **2-1-1 Principle of applying pressure**

The instruments and methods that have been employed for the generation of high pressure are probably more diverse than those in any other field of instrumentation. Pressure-generation method can be divided into three categories corresponding to existing domains of high-pressure method. The first category deals with hydraulic technique for the compression of fluids. This concerns, as a rule, pressures up to 1.4GPa, or at most 1.8GPa, which are applied to large volumes of fluid ( 1mm<sup>3</sup> ) . The second category deals with the compression of large-volume solid samples in the range from 2 to 20-30GPa. This is the domain of high-temperature high-pressure experiments in material science and geophysical studies. In these studies, quite different instrument and methods must be used. The third category deals with diamond anvil cell ( DACs ) . Although, in principle, these cells are not difficult, in practice they have such original characteristics and widespread applications that is almost the most popular instrument used in high-pressure experiments.

The amount of experimental data collected on semiconductors under high pressure



has grown rapidly since the development of the diamond anvil cell. The principle of the technique is as follows. A sample incorporated with fluid, which acts as a pressure-transmitting medium, is placed inside a small aperture drilled through a thin sheet of metal called gasket. Pressure is applied to the sample plus fluid system by mechanically forcing the two diamond faces closer together. Depending on the gasket material, aperture size, and the diameter of diamond face, pressures in the order of one mega-bar can now be achieved in the laboratory.

## 2-1-2 Diamond Anvil Cell

We use diamond-anvil cell (DAC) to generate high pressure in our experiment. It is currently the most popular instrument for the study of materials under high pressure. It has revolutionized high-pressure research, not only because it can easily reach a pressure near that in the center of the earth, but also because it admits varied measurement techniques for the study of matters under such conditions. **Fig2-1** shows the basic set-up of DAC. It is the outer part of the whole DAC. The diamond mounts are sticking on the hemispherical mount (**Fig2-2**). These are called the “rockers”. They can be translated for centering and is locked in position by adjusting the x and y axes, and the rocker can be tilted in its socket to secure parallel alignment of the anvil flats, as determined by the optical interference fringe pattern. In **Fig2-3**, a metal gasket with a drilled hole is placed between the two opposed diamond anvils. The hole was drilled on the gasket as sample chamber. In this chamber, the sample, pressure media, and ruby powder were placed.

This chamber is subjected to pressure when a force squeezes the two opposed diamond anvils together. Samples are compressed by the turn of DAC’s screw, making the two opposed diamonds pressing mutually. A huge pressure is then created. The cell can routinely be used to ~ 60kbar pressure, depending on the diamond size. In most DAC, the diamond is usually in the 0.2~0.4 carot range (1 carot = 1/15 gram), and within this range the smaller the face is usually better. Diamonds for the anvil are usually selected from brilliant-cut gem stones. The selection of the diamonds and size depend upon the type of DAC and the nature of the investigation.





Fig2-1 : The basic set-up of DAC

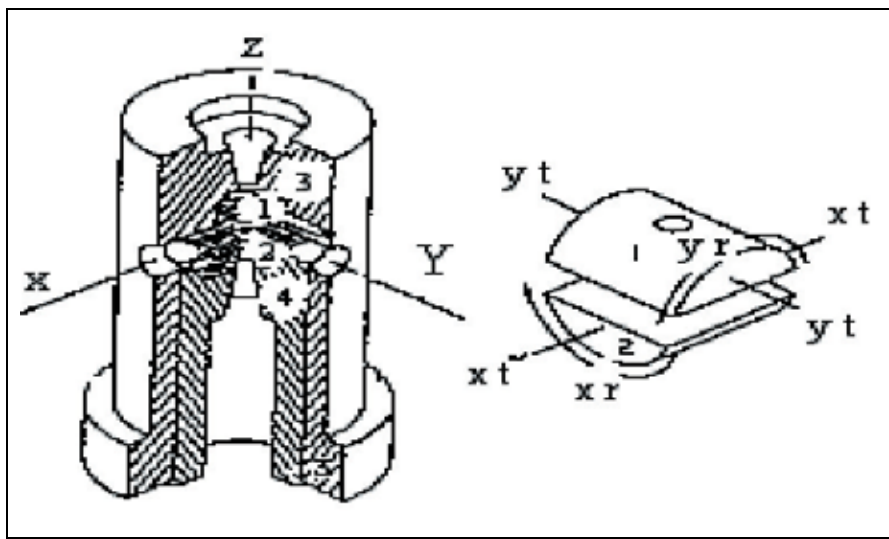
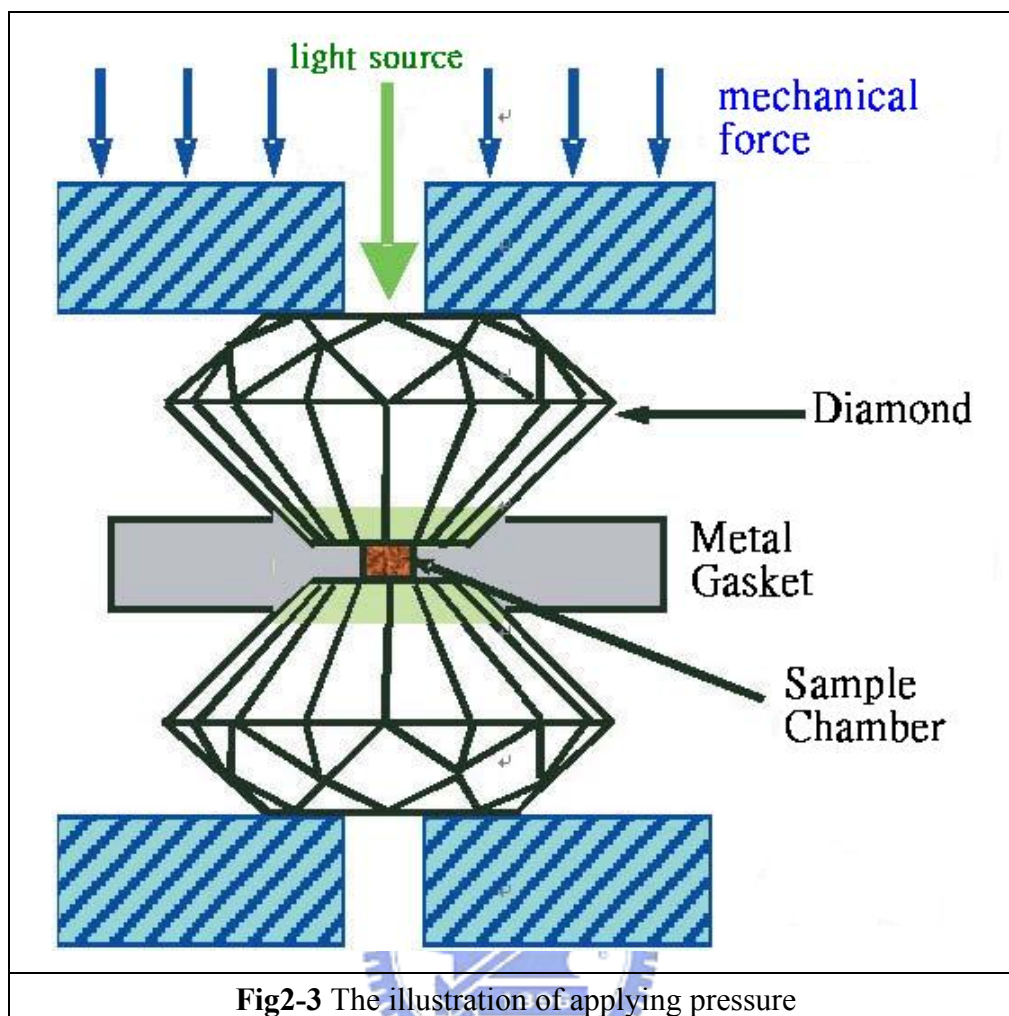


Fig2-2 : The inner part of DAC



**Fig2-3** The illustration of applying pressure

### 2-1-3 Gasketing, and Pressure Medium

The early work performed in the DAC was done on solids that were pressed between the diamond anvils without the use of a gasket. These conditions provided a highly non-hydrostatic environment for the solid.

Studies demonstrated that a pressure gradient existed under these conditions that were parabolic in nature, with pressures in the center reaching 1.5 times those on the edges. Thus, any pressure measured under these conditions was basically an average pressure. Van Valkenburg (1963) first used a gasket with the DAC. The use of a gasket inserted between the diamond anvils and the immersion of crystals in a fluid were major advances in the use of the DAC. **Fig2.4** shows the sectional view of the gasket indentation and the sample chamber. The metal gasket not only extends the life of a pair of anvil, but also allowed the sample to be compressed in a fluid pressure-transmitting medium, so they can provide a truly hydrostatic environment for the sample. In a non-hydrostatic situation, the pressure of unknown value often becomes a serious problem in the interpretation of measurement. Thus the use of a

gasket for the containment of the pressure medium is a very important point for hydrostatic pressure creation in DAC. Some debate exists as to whether simply using a gasket between the diamond anvils without fluid provides sufficiently hydrostatic conditions to allow the worker a degree of confidence that the calibration of pressure in this situation is not an average pressure. It is probably true that the use of a gasket will reduce the pressure gradient more than those obtained when no gasket is used, but the uncertainty as to the quantity of the applied load absorbed by the gasket presents a problem.

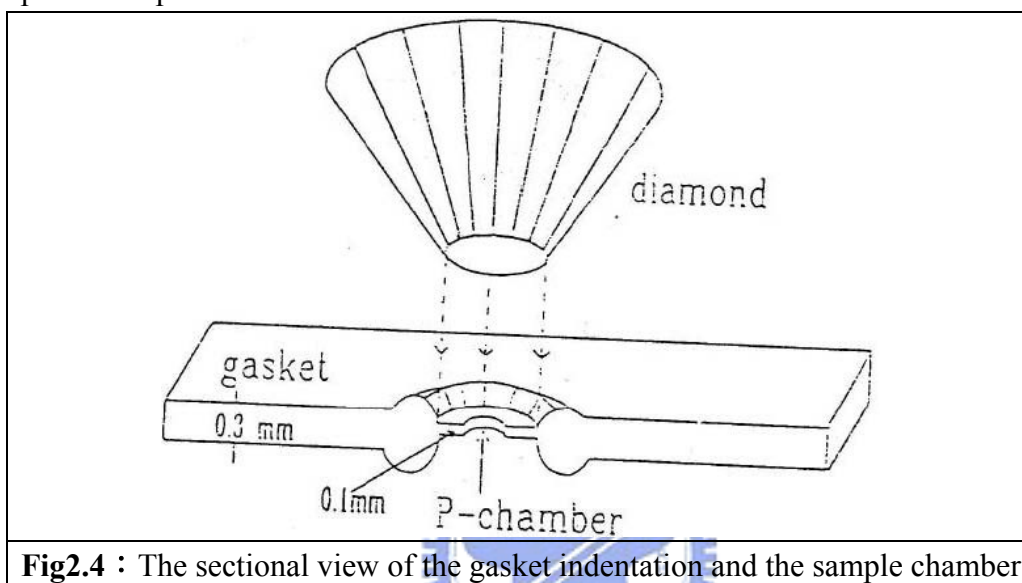


**Fig2.4 :** The sectional view of the gasket indentation and the sample chamber

In order to generate a hydrostatic pressure environment for sample, a fluid pressure medium is required. In this technique, placed the solid of interest under virtually hydrostatic conditions, and pressure calibrations became more meaningful, especially when one could observe changes under a microscope. Various fluids have been used, but a 4:1 methanol-ethanol mixture has proved to be very popular. Unfortunately, the use of fluids is valid only to  $\sim 100$  kbar, since most liquids become solids above this pressure. De-ionized water (DI water) is also considered to be a pressure medium, but it transfers to solid ice VI and ice VII at 0.6 and 2.1 GPa, respectively. However, previous study showed that the R1-R2 splitting in ruby fluorescence was maintained well up to 16.7 GPa; therefore, it seems not to be a serious problem before reaching to this pressure.

In the work of Lin et al, [ref7] such a splitting was well recorded up to 36 GPa. Hence, DI water seems to be a suitable pressure medium in high-pressure studies. For this reason we choose DI water as the pressure-transmitting medium in our experiment.

## 2-1-4 Pressure Calibration

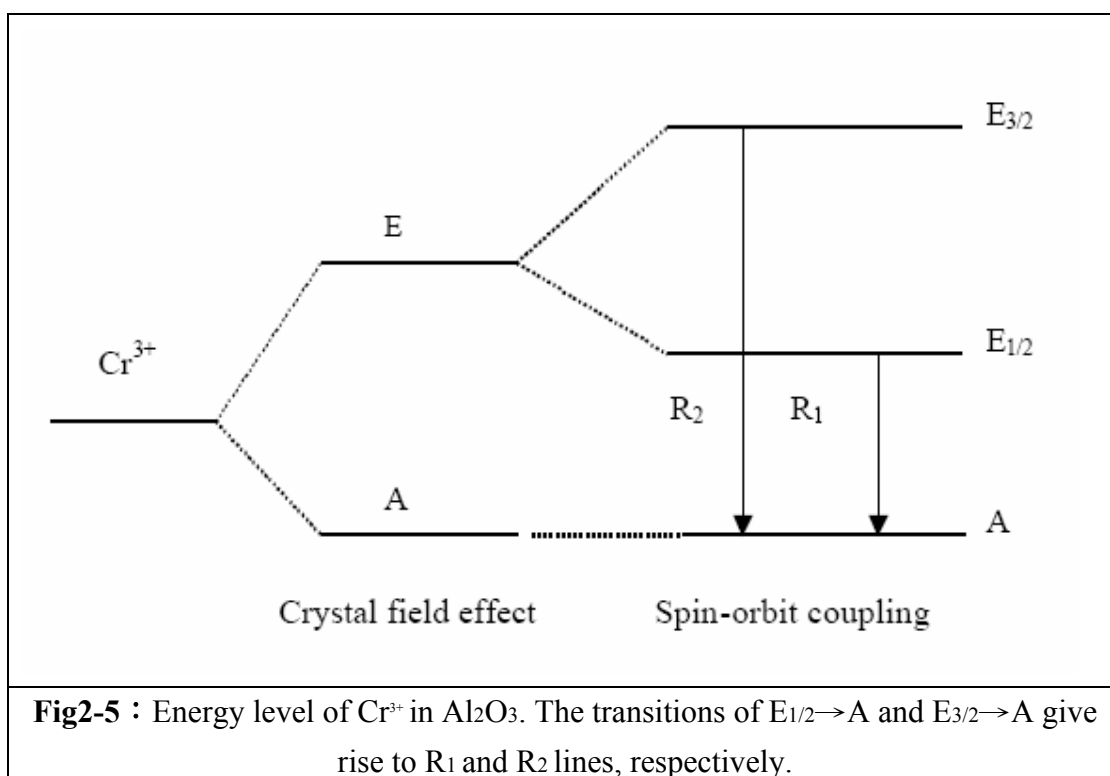
Various methods of pressure calibration involving the DAC have been used. In early years pressure in the DAC was estimated by calculating force over area, the known fixed point, and internal markers such as NaCl or silver in high-pressure X-ray studies. These methods are not convenient and are often proved to be inaccurate.

In 1972 a major development occurred in the calibration of pressure in the DAC. This breakthrough was successful because of the use of visual microscopic studies in the DAC. Foreman et al. first calibrated the shift of the R-line ruby fluorescence peaks as a function of pressure in the DAC, and demonstrated that this shift could be used as a convenient internal pressure-calibrator. The technique incorporates a ruby crystal with the sample of interest and measures the pressure dependence of the sharp ruby R1 line fluorescence. Actually, two kinds of fluorescence with different wavelength are excited (R1 and R2 at 692.8 and 694.2 nm), and both dependencies can be followed simultaneously. The fluorescence's are induced by an Ar<sup>+</sup> or a Cd-He laser.

Ruby consists of Al<sub>2</sub>O<sub>3</sub> doped with Cr<sub>2</sub>O<sub>3</sub>, in which some of the Al<sup>3+</sup> ions replaced by Cr<sup>3+</sup>. Normally, Cr<sup>3+</sup> in a cubic field would show a single band due to the spin transition  ${}^2E \rightarrow {}^4A_2$ . In ruby the Cr<sup>3+</sup> occupies an Al<sup>3+</sup> site, but being of different size, such that it assumes a lower symmetry. This splits the states of the Cr<sup>3+</sup> ion, forming an A-symmetric quartet ground state and a doubly degenerate first-excited state with E symmetry, as shown in **Fig2-5**. The combined effects of the trigonal field and spin-orbit coupling further splits the first excited state into E<sub>3/2</sub> and E<sub>1/2</sub> states separated by 3.6meV. The electronic transition E<sub>1/2</sub> → A and E<sub>3/2</sub> → A give rise to the R1 line at 6942Å and R2 line at 6928Å, respectively. Those so called R-lines are the active transitions in the ruby laser. Under high pressure these shifts to higher wavelengths and the shift is measured linearly with increasing pressure. The accepted value for the ruby R-line shift is 0.365Åkbar<sup>-1</sup>. In addition to this linear dependence of fluorescence on pressures, the line shape of the ruby fluorescence spectrum can also be used as a measure of the degree of hydrostaticity in the DAC sample chamber. Due to its high intensity and sharp line width (7.5 Å), only a small ruby chip is necessary for pressure calibration. Also, because of the acceptable pressure dependency (0.36 Å kbar<sup>-1</sup>) and linearity at lower pressures ruby scale is really a rapid and dependable method. Despite of these advantages, ruby calibration still has its limitation. First of all, ruby has a significant temperature coefficient (0.068 Å °C<sup>-1</sup>) in the same direction (red) for both temperature and pressure. Its thermal line broadens with pressure, causing R1 and R2 to overlap and limiting its use for pressure calibration to 300°C. Less heating of the ruby will cause expansion along the axis, which results in lower symmetry, and spin-orbit coupling will increase R2  $\Delta R \sim 29.3$

$\text{cm}^{-1}$  at 150 K to  $29.7 \text{ cm}^{-1}$  at 293 K.

Since both temperature and pressure cause a decrease in R1 and R2 frequencies, it is possible to overestimate the pressure if local heating occurs (e.g., heating in a laser). Second, there are some uncertainty in linearity of extrapolated dependency at mega bar pressure and pressure broadening of both R1 and R2 at pressures  $> 1\text{Mbar}$ . Also, the requirement of laser excitation for fluorescence may be prohibitive in small laboratories or schools (the fluorescence of ruby is very weak at low pressure; a highly sensitive spectrophotometer is needed to measure this fluorescence). Finally, values of  $\Delta R$  will change under non-hydrostatic pressures.



## 2-1-5 The high pressure experiment process

### A. Sample Preparation

Our samples are the colloidal quantum dots which are already in the di-water: the most common pressure media. We can load our sample in drilled gasket directly. On the contrary, samples are not colloidal ex:  $\text{Al}_{1-x}\text{In}_x\text{P}$  which is bulk sample that we need to deal with carefully. (See appendix A)

### B. The diamond anvil cell alignment

The procedures for adjusting the diamond anvil cell include the correctly setting of axial and tilt alignment of DAC without a gasket. The main purpose of this procedure is to make the two diamond anvils contacted each other and paralleled mutually in order to support huge force uniformly over the whole diamond flat. Before alignment, we must first clean the faces of diamonds thoroughly with Q-tips moistened by acetone. This cleaning action must be done under a microscope in order to check if the faces are completely clean. The faces should be free of any dirt otherwise it will cause misalignment. After cleaning, it is ready to begin the cell alignment in two parts.

1. **Axial alignment:** Bring carefully the two diamond anvils in direct contact and make sure that they are coaxially centered. If the two flats are not in suitable positions, use the two “adjusting screws” set in mutually perpendicular directions to adjust the rocker of cell until the faces of diamond become flat and parallel.

2. **Newton ring alignment:** By applying the theorem of Newton ring, we are able to check further the parallelism between two diamond faces.

If the two anvil faces are not parallel, we will observe some optical interference fringes, which are formed from white light transmitted through the contact diamonds, under a microscope.

### C. Gasket preparation

In our work, we use stainless steel T304, which can maintain pressure up to about 35GPa, as the material of gasket. The procedure for gasket preparation can mainly be divided into two parts. First we have to pre-press the stainless steel gasket to about 15GPa. Before this step, it is necessary to clean the gasket thoroughly. And also, the distance between gasket and diamond flat must keep at about 200  $\mu$  m in order to provide enough space for gasket pre-pressing. The whole procedure is listed below:

1. Choose suitable rings to make the distance between gasket and diamond below the gasket being around 200  $\mu$  m and seat the gasket on the diamond below.
2. Bring the two diamond cells in direct contact and compress the cell to make a slight indentation on the gasket.
3. Separate the two diamond cells, and put a few ruby chips in the indentation made previously. Here ruby is used for pressure calibration.
4. Bring the two cells in contact again, and then put it in the body for generating high pressure. Turn the screw head clockwise slowly until the pressure necessary is reached and then loose the screw. Taking the gasket out of the cell, we can see a deeper indentation under a microscope.

After the process described above, the thickness of this indented gasket is now around



150  $\mu$  m, which is much smaller than the initial value (around 300  $\mu$  m). Now we have to drill a hole at the center of the indentation of the gasket. This hole is drilled by the micro electric discharge drilling system. Usually the gasket hole is 90  $\mu$  m in diameter. In order to make a whole circular hole, it is necessary to make sure that the drilling needle is straight and perpendicular to the indentation surface.

For this purpose, it is helpful to flatten the gasket blank.

## D. Sample loading

The hole on the gasket is prepared as a chamber for sample loading.

Since the size of this chamber is very small, our samples must be thinned and cleaved into a size smaller than the pressure chamber. This way, the chamber can thoroughly surround the sample without destroying the sample. Sample loading is therefore quite difficult and must be carried out under a microscope. The procedure of sample loading is described as follows:

1. Choose suitable rings to make the indentation of the gasket directly contact with the flat of the diamond and seat the gasket on the diamond anvil below.
2. Uniformly place a few ruby chips (about 1  $\mu$  m) on the upper diamond flat for pressure calibration.
3. Using needle inhale a little sample (colloidal quantum dot in di-water) to inject into sample chamber, by the way, di-water is pressure transmitting medium.

Then bring the two cells in contact as soon as possible (this is to prevent sample from coagulating) and turn the screw to tighten it a little. Now we can start various optical measurements.

## 2-2 Raman scattering experiment

**Figure2-6** is our Micro Raman Scattering experiment setup in NHCTC. The system is composed of a Kr ion laser, main microscope, CCD detector, spectrometer, and data analysis computer shown as figure. You can see the laser reflected by two mirrors is going into the main microscope and is focus by objective then meet the sample to produce Raman scattering process. In this chapter, we will introduce how these components work.

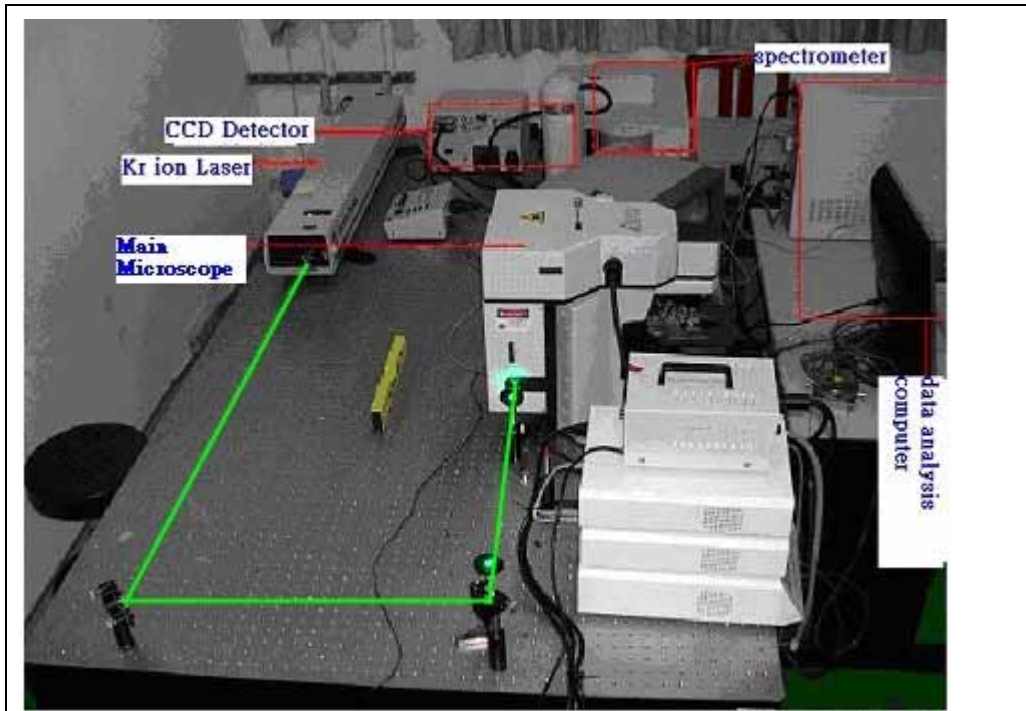
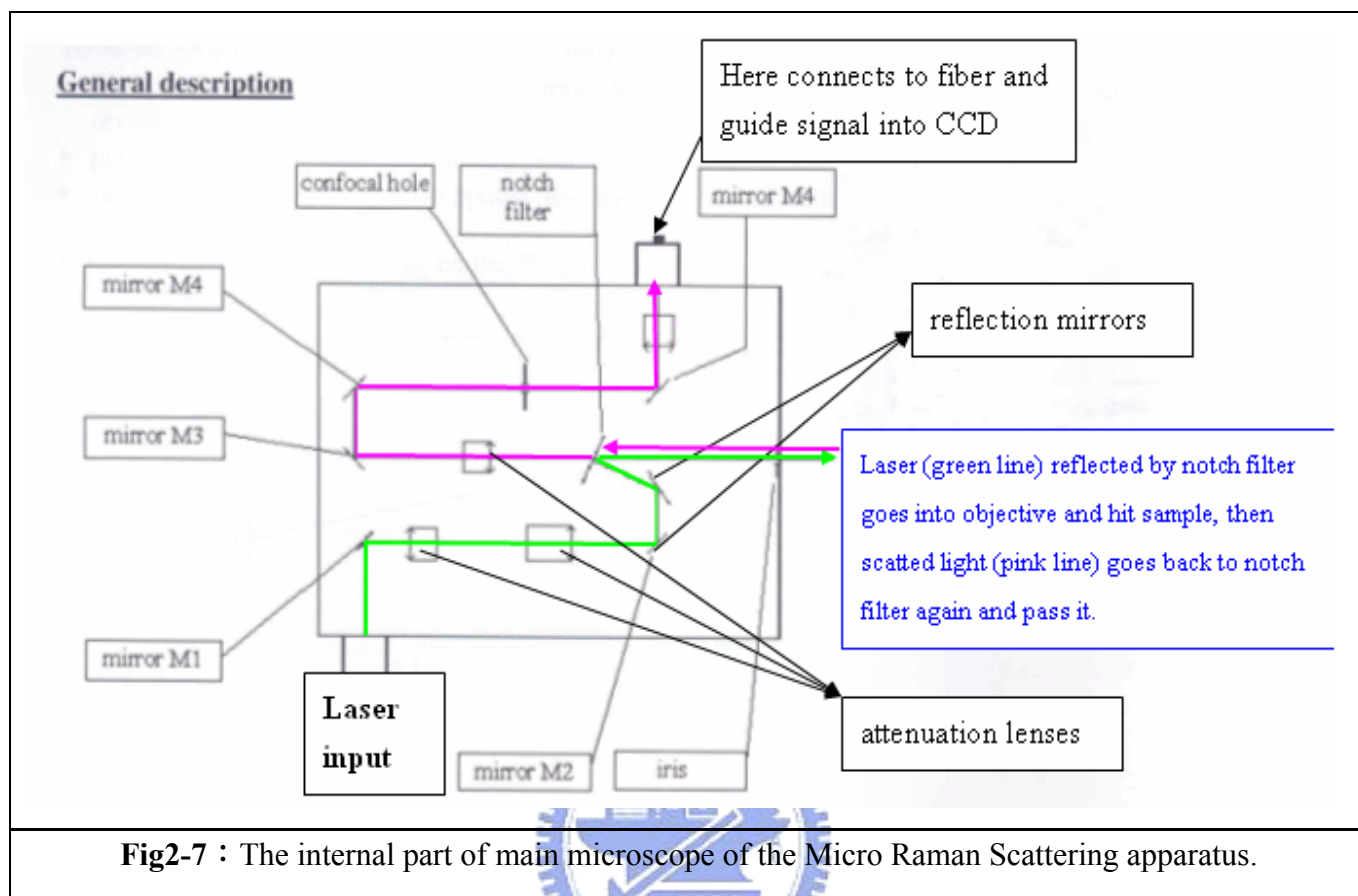


**Fig2-6 :** The configuration of Micro Raman Scattering experiment in NHCTC.

At first we simply introduce the process of Raman spectrum measuring experiment. The rough figure of the internal part of main microscope is shown in **Fig2-7**. See from Fig2-7, the laser ( green line ) is coming from input and is reflected by mirror M1, after passing two attenuation lenses then arrive mirror M2. After two reflection by a pair of reflection mirrors, laser light achieves notch filter which like a beamsplitter can reflect incoming laser (i.e.: the green line) and filter unwanted laser in scatted light ( i.e.: the pink line ) . Notch filter plays an important role to avoid the intensity of backing laser exceeding the scatted light which is relatively weak than laser. The laser reflected by notch filter ( green line ) goes into the objective and is focus to hit sample to produce Raman scattering process. The scatted light ( pink line ) also collected by objective then comes back to notch filter again. It is important that noise laser is filtered by notch filter; only the scattering light can pass. The passed light is reflected by M3 and M4 mirrors and goes into the confocal hole which is set to make sure the single is coming from the focal point of incident laser. By passing through confocal hole, single is reflected by mirror M5, then finally go into the fiber and enter into spectrometer. The spectrometer divides light into many different wavelength regions and CCD detector count intensity of different wavelength light. By properly choosing integrating time and average times, computer shows the Raman scattering spectrum to us. The alignment of the optical units in our Raman experiment is described in **Appendix B**.





## 2-3 PL and photon lifetime spectrum experiment

### 2-3-1 Instrument Introduction :

In order to exploit the merits of a powerful analysis tool such as time-correlated fluorescence spectroscopy, one must in some way or other record the time dependent intensity profile of the emitted light. While in principle, one could attempt to record the time decay profile of the signal from a single excitation-emission cycle; there are practical problems to prevent such a simple solution in most cases. First of all the decay to be recorded is very fast. Typical fluorescence from organic fluorophores lasts only some hundred picoseconds to some hundred nanoseconds. In order to recover fluorescence lifetimes as short as e.g. 500ps, one must be able to resolve the recorded signal at least to such an extent, that the exponential decay is represented by some tens of samples. This means the transient recorder required would have to

sample at e.g. 50ps time steps. Clearly this is hard to achieve with ordinary electronic transient recorders. Secondly the light available may be simply too weak to sample an analog time decay. Indeed the signal may consist of just a few photons per excitation/emission. Then the discrete nature of the signal itself prohibits analog sampling. Even if one has some reserve to increase the excitation power to obtain more fluorescence light, there will be limits, e.g. due to collection optic losses, spectral limits of detector sensitivity or photo-bleaching at higher excitation power. **The solution is Time-Correlated Single Photon Counting (TCSPC). Since with periodic excitation (e.g. from a laser) it is possible to extend the data collection over multiple cycles, one can reconstruct the single cycle decay profile from single photon events collected over many cycles.**

The method is based on the repetitive precisely timed registration of single photons of e.g. a fluorescence signal. **The reference for the timing is the corresponding excitation pulse.** As a single photon sensitive detector, one can use a **Single Photon Avalanche Photodiode (SPAD)**. Provided that the probability of registering more than one photon per cycle is low, the histogram of photon arrivals per time bin represents the time decay one would have obtained from a single shot time-resolved analog recording. The precondition of single photon probability can (and must!) be met by simply attenuating the light level at the sample if necessary. If the single photon probability condition is met, there will actually be no photons at all in many cycles. Figure2-8 and Figure2-9 illustrate how the histogram is formed over multiple cycles :

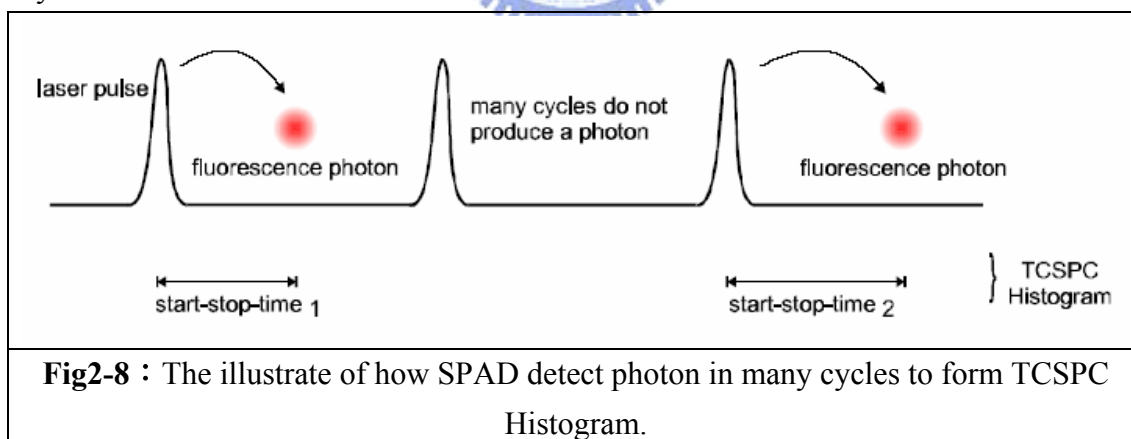


**Fig2-8 :** The illustrate of how SPAD detect photon in many cycles to form TCSPC Histogram.

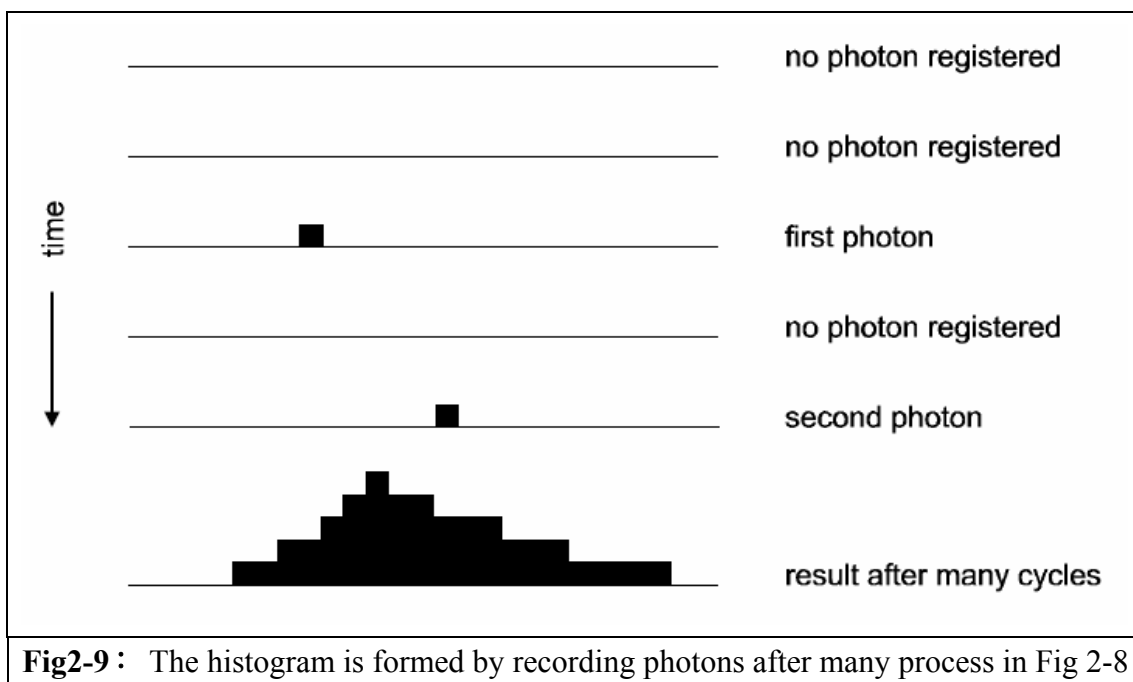


**Fig2-9 :** The histogram is formed by recording photons after many process in Fig 2-8

The histogram is collected in a block of memory, where one memory cell holds the photon counts for one corresponding time bin. These time bins are often referred to as time channels.

In practice the registration of one photon involves the following steps: first the time difference between the photon event and the corresponding excitation pulse must be measured. For this purpose both signals are converted to electric signals. **For the fluorescence photon this is done via the single photon detector mentioned before. For the excitation pulse it may be done via another detector** if there is no electrical sync signal supplied by the laser. Obviously all conversion to electrical pulses must preserve the precise timing of the signals as accurately as possible. The actual time difference measurement is done by means of fast electronics which provide a digital timing result. This digital timing result is then used to address the histogram memory so that each possible timing value corresponds to one memory cell or histogram channel. Finally the addressed histogram cell is incremented. All steps are carried out by fast electronics so that the processing time required for each photon event is as short as possible.

When sufficient counts have been collected the histogram memory can be read out. The histogram data can then be used for display and e.g. fluorescence lifetime calculation.

### **2-3-2 Configuration and Standard Components :**

Our system is called “Micro-Time 200 fluorescence lifetime microscope system”,

which is a powerful, newly-developed instrument capable of Fluorescence Lifetime Imaging with Single Molecule Detection sensitivity. It contains the complete optics and electronics needed for recording virtually all aspects of the fluorescence dynamics of microscopic samples or femto-liter volumes. The instrument gains its exceptional sensitivity and flexibility in combination with an unprecedented ease of use from a unique fusion of miniaturised and highly sophisticated state-of-the-art technologies. For the first time, these technologies enable to run an instrument of comparable complexity and power to be operated in routine work, without having to spend more time on instrument maintenance than on original scientific content. The underlying key technologies are the proven Pico-second Diode Lasers and the Time-Correlated Single Photon Counting electronics developed by PicoQuant, complemented by state-of-the-art piezo-scanning technology and optics from industry leaders. The insight of “Micro-Time 200 fluorescence lifetime microscope system” is shown in **Fig2-10**.

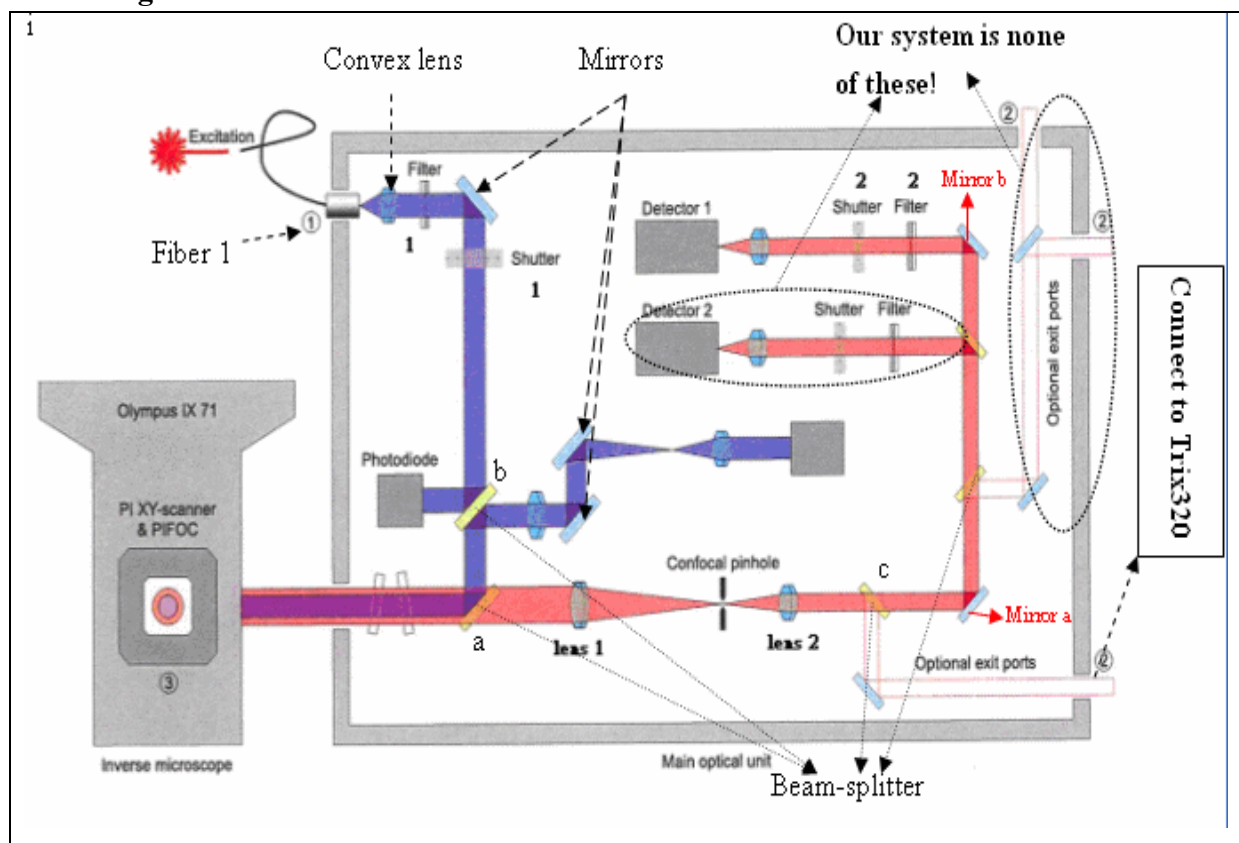


**Fig2-10** : The insight of Micro-Time 200 fluorescence lifetime microscope system. (blue line is the incoming laser and pink line is the signal of laser excitation.)

### 2-3-3 Overview :

Now we are going to explain how this system operates. See from **Fig2-10**, the

excitation which come from **fiber1** entering into the main optical unit is collected by a convex lens with that become a parallel light( **blue color** ). After reflecting by a mirror, this parallel light comes to **beam-splitter b** which splitter light into two components; one goes to photodiode while the other directly pass the beam-splitter. Photodiode is an apparatus that told you the intensity of incoming excitation. The passing light is then reflected by **beam-splitter a** and enters the microscope (Olympus IX 71) to excite the sample; then signal (fluorescence of sample ; **pink color**) is collected by objective and come back via the original path and pass **beam-splitter a** again. The signal is then traverse through **lens1, confocal pinhole and lens 2**. Confocal pinhole is making sure the signal is excited from focal point of laser. In order to measure PL and lifetime at the same system, we use **beam-splitter c** to divide light into **optional excite port 2** which is connected to a spectrometer (Trix320) while the other light pass through beam-splitter c. The passing light reflected by two mirrors ( Mirror a,b) enters **dector1** to record life time. Near dector1 there are filter2 to decrease light intensity and shutter2 to control light passing or not. Under this setup, we can use the lock gate to control signal into spectrometer or detector1, the former is used to measure PL while the later is for recording lifetime.

We will introduce in detail the use of the entire component in **Appendix C**.

## **Chapter3 : Experiment result and discussion**

### **3-1 Result**

#### **3-1-1 Raman spectrum**

Our sample in this experiment is the 630nm emission colloidal core/shell CdSe/ZnS QDs with core diameter equal to 10 nm and thickness of shell equal to 1 nm. In this experiment we can find that both the vibration mode of CdSe and ZnS appears in our Raman spectrum. Our data shown in **Fig3-2** 、 **3** agree with the Raman spectrum obtained by Ref1[See **Fig3-1**]. The peaks presented in **Fig3-2** 、 **3** are the CdSe LO mode at  $\sim 210\text{cm}^{-1}$ , CdSe 2LO mode at  $\sim 420\text{ cm}^{-1}$  and ZnS LO mode at  $\sim 300\text{ cm}^{-1}$ . By the way, the data shown in **Fig3-2**, **3** are coming from the same QDs observed at different days for double check.

As we had just mentioned that the experimental data shown below are observed at different days, the data shown in **Fig3-2** is observed on Oct-24/2005. In this experiment, the pressure is added up to 34.11 GPA, and there were only three pressure

observation presented before the occurrence of phase transition. The other experiment data shown in **Fig3-3** is obtained Nov-08/2005 and this data is decomposed into three parts, one is for the process of adding pressure until the peaks of CdSe LO and 2LO disappears (phase transition) [**Fig3-3**], the other is to add pressure up to the highest one(36.72GPA)after phase transition[**Fig3-4**], and the final one is for the decreasing pressure from the highest pressure down to 3.44GPA which is shown in **Fig3-5**. The data shown in **Fig3-6** is the whole Raman spectrum in this experiment ; include the loading pressure and unloading pressure process.

From our experiment data shown in **Fig3-2** and **Fig3-3** , one can easily see that : in the loading process the LO mode, 2LO mode of CdSe and the LO mode of ZnS are all shift to high frequency at first. ( blue shift )

When the pressure approaches nearly 7GPA, we find that both LO peak and 2LO peak of CdSe start to disappear and the ZnS LO mode remains exist up to 35GPA as shown in **Fig3-2** and **Fig3-3**. From this information we deduce that the core CdSe begins phase transition at about 7GPA, compared to the pressure-induced phase transition in bulk CdSe at about 3 GPa. We label this phase transition in QDs as the “Phase Transition I”. Due to the core-shell structure of QDs, we can reasonably assume that this retarded pressure-induced phase transition in core comes from the screening effect of ZnS shell.

By synchronal measuring the PL spectrum and Raman spectrum, we can find some interesting information by comparing these two data. The most important phenomenon is that : the PL spectrum can't be explored after phase transition had been found in QDs from Raman spectrum. This gives us information that the core in QD may become metal phase for two reasons :

1. When QD is under phase transition, the LO peak and 2LO peak of CdSe start to disappear in Raman spectrum; this implies PHI to occur in core of QDs.
2. QD is not under fluorescence after PHI; this verifies that the metal phase of core happens in QD.

From the band diagram of bulk CdSe with rocksalt structure as shown in **Fig3-7**, one can see that the conduction band overlaps the valance band; this verifies the occurrence of the metal phase of CdSe. ( the band diagram is calculated by ab-initio ) We believe the structure difference caused by phase transition in QDs is just the same as it in bulk CdSe whose structure is from zinc-blende to rocksalt. In other words we believe after phase transition the structure of core in QDs is the rocksalt structure the same as the bulk behavior.

After phase transition I, the LO and 2LO mode of CdSe disappears and a new undetermined peak appears nearly  $\sim 156 \text{ cm}^{-1}$ , this new peak is very interesting due to the fix position of this peak as pressure varies! After increasing the pressure so that it

is larger than  $\sim 7$ GPa, the peak is always presented and the position of it unchanged until pressure goes up to 34GPa. Even if the pressure reduced below 7GPa that come to the same situation. (See the data shown in **Fig3-5**, this peak is also present even the pressure is reduce to be lower)

The LO signal of ZnS is very weak in 1108 data, it is almost unrecognizable before phase transition I, but after phase transition I it can be recognized even if it is still weak and nearly disappears at 36.72GPa( See **Fig3-4** ). At first, this pressure might be regarded as another phase transition, however by comparing with the 1024 data

( **Fig3-2** ) , we see the signal of ZnS is always distinguishable up to pressure equal to 34.11GPa. For this reason it should not be another phase transition and may come from the defect of sample.

While in the unloading process, the LO mode of ZnS starts to be red shift along the original path of loading process. ( see **Fig3-5** ) When the pressure reaches 3.44GPa, the LO mode of CdSe appears again and its peak position corresponds to the data of loading process, however, the CdSe 2LO mode does not appear again. This phenomenon makes us to believe that CdSe might not reduce back to the zinc-blende structure again. Thus the phase transition I is an irreversible one.





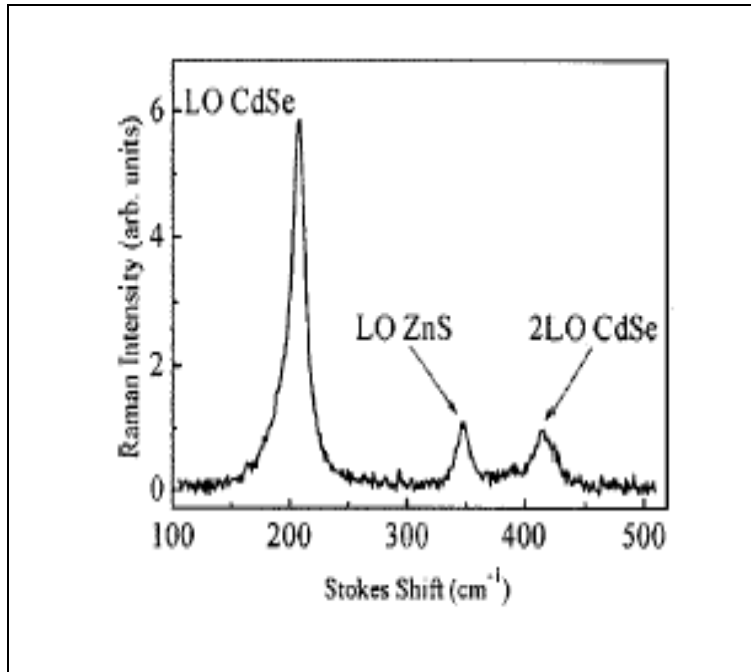


**Fig3-1 : Raman spectrum of CdSe/ZnS QD's with a shell thickness 3.4 ML excited by a 476.5-nm line of an Ar12 laser.**

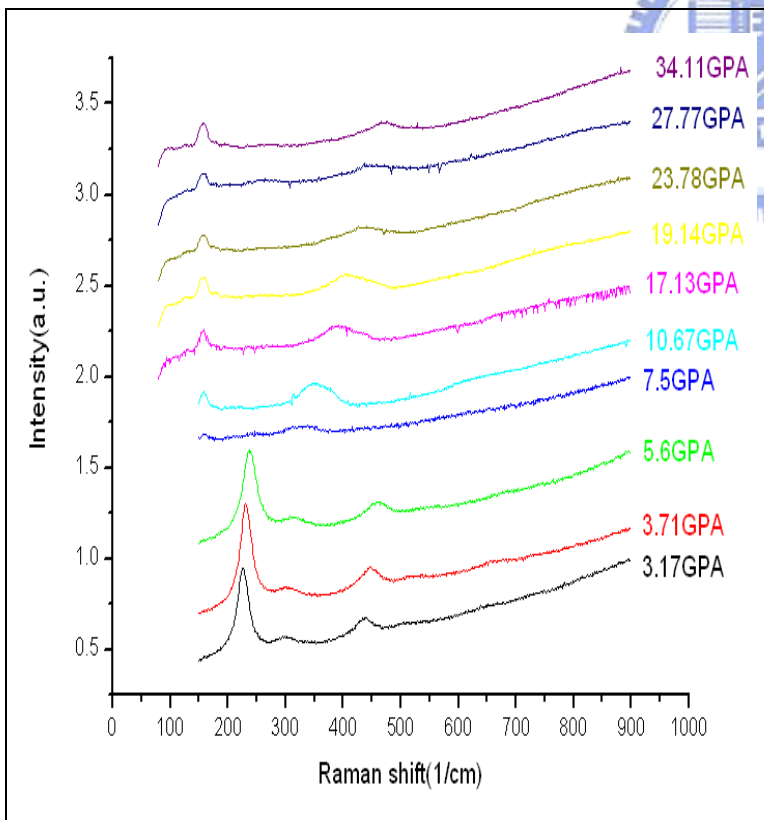


**Fig3-2 : Raman spectrum of CdSe/ZnS QDs in di-water under different pressure. (gotten in 1024)**

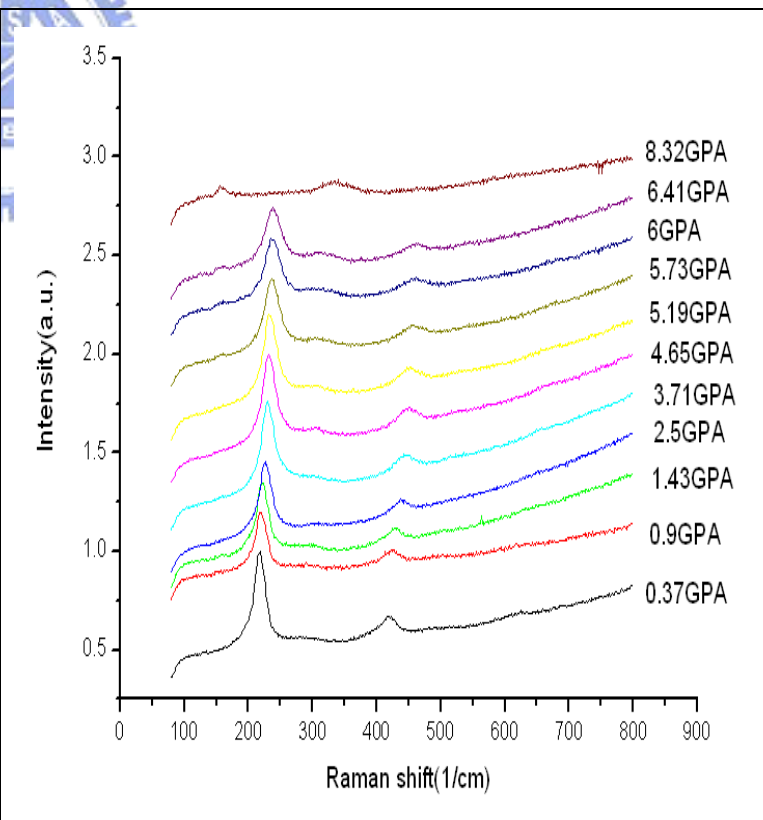


**Fig3-3 : Raman spectrum of CdSe/ZnS QDs in di-water. The pressure is added up to phase transition. (gotten in 1108)**



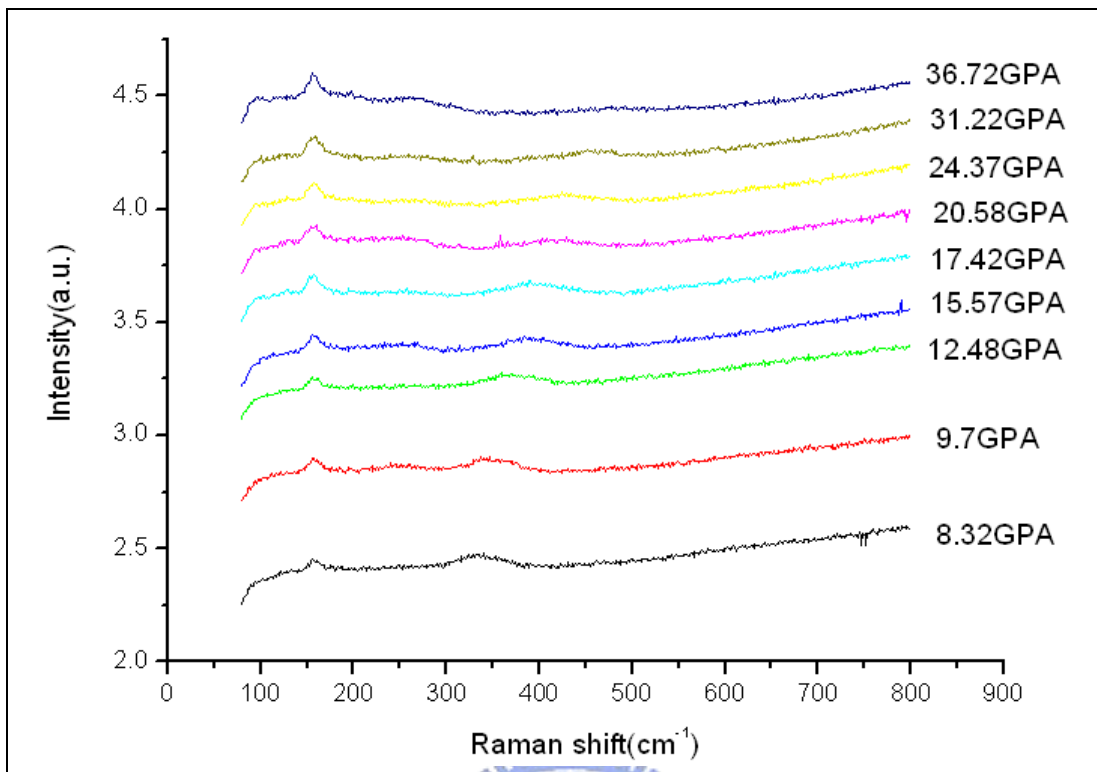


**Fig3-4 : Raman spectrum of CdSe/ZnS QDs in di-water. ( gotten in 1108 )  
Pressure is added ABOVE phase transition up to 36.72GPA.**

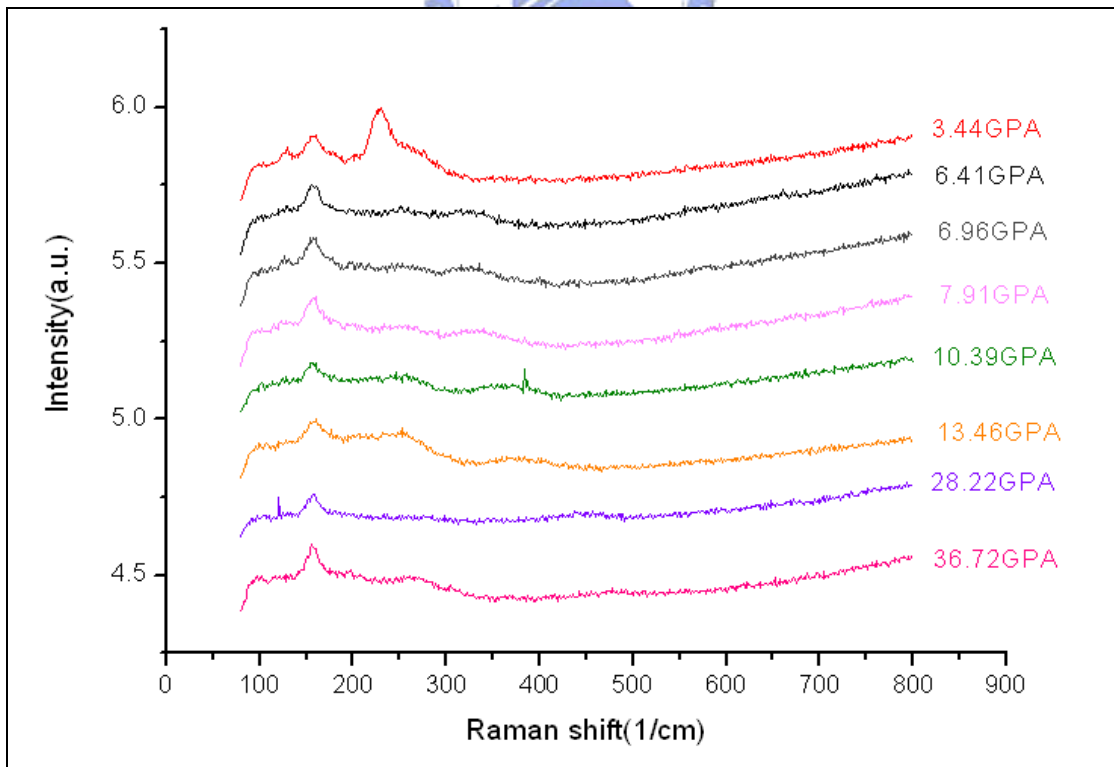


**Fig3-5 : Raman spectrum of CdSe/ZnS QDs in di-water. ( gotten in 1108 )  
Reduce pressure from 36.72GPA to 3.44GPA.**

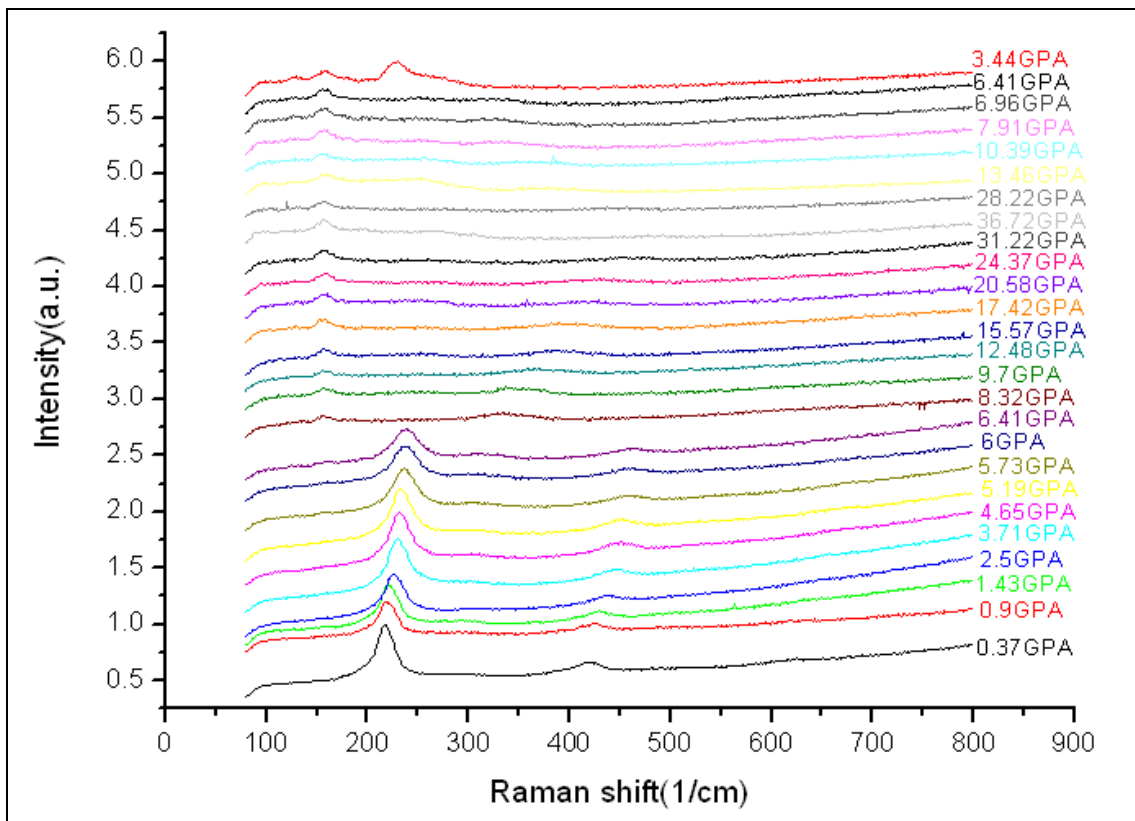


Fig3-6 : Whole Raman spectrum of CdSe/ZnS QDs in di-water. ( gotten in 1108)

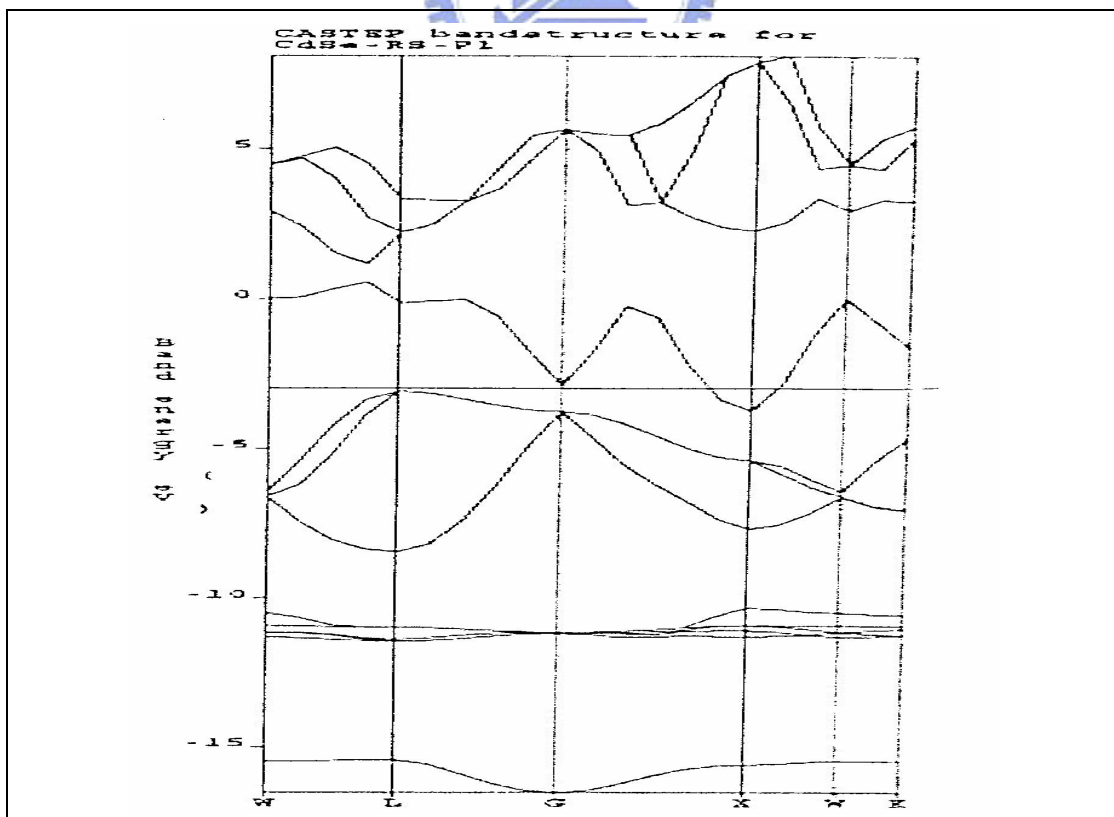


Fig3-7 : Band diagram of CdSe with rocksalt structure calculated by CASTEP.

### 3-1-2 Photon luminescence

In this chapter we only focus on how energy band gap of QDs changed under the applying of pressures. In this experiment, our sample is a quantum dot with radius in 5nm with ZnS shell cladding which thickness is 1nm.

The first thing we need to remark is that only PL spectrum below the pressure of phase transition is obtained. This is because as Raman spectrum exhibits the occurrence of phase transition, the PL spectrum is no longer to be measured.

From our experiment data shown in **Fig3-8** we see the band gap  $E_g$  of QDs has obvious pressure dependence. To explain the reason we follow the discussion in ref. [2] ; in this paper the QD has two size regions for investigating the pressure dependence. ( Rigion1: QD's radius  $< a_0$  ; Rigion2 : QD's radius  $\geq a_0$ , where  $a_0$  is the effective Born radius which is 5.6nm for CdSe ) By the way, the QD in ref. [2] is the pure CdSe QD without shell.

They believe that the mechanism of the shift of band edge under pressure is due to the electron-phonon interaction of polaron. For small size QD, the previous experiment data shows zero pressure parameter( $dE/dP=0$ ) and they interpret that is because the strong coupling of defect levels in QD to the core levels due to the strong confinement of the exciton wave function. This results in an effect that the excitonic levels being primarily perturbed by the particle size instead of electron-phonon (el-ph) interactions. This is because that the el-ph interaction is not dominant in this small size regime and the pressure dependence doesn't occur in low pressure. However for the larger QD size( $r=40\text{\AA}$ ), the bulk like pressure dependence is observed as expected. In this thesis, all the pressure parameters are all obtained for lower pressure (up to 0.25GPa), and no lattice structure change are concerned. They only focus on the variation of the polaron energy with the lattice ionicity for different sizes of QD.

Ref. [2] mainly studied the pressure parameter (  $dE/dP$  ) of different size QDs. The diagram of  $dE/dP$  parameter versus QD' size is shown in **Fig3-9**. The pressure parameter of QDs with a radius of 22.5Å is about 80meVGPa<sup>-1</sup> while that of the QD with radius of 40Å is about 40meVGPa<sup>-1</sup> which is close to the bulk values of 37.5 meVGPa<sup>-1</sup>. From the experiment data of the 5nm (in radius) core/shell CdSe/ZnS QD, the band edge-pressure curve can be fitted by a polynomial, obtain as :

$$E_{gQD}=1.985+0.0354P-0.0014P^2 \text{ eV} \dots\dots\dots (3.1)$$

as shown in **Fig3-10**.

On contrary, the bulk CdSe Eg-pressure curve can be fitted by:

$E_{g,bulk}=1.71+0.0375P$  eV, as shown **Fig.3-11**.

Thus, the pressure parameter ( $dE/dP$ ) of our QDs is almost equal to the bulk's value at low pressure ( for low pressure the term of  $P^2$  can be ignored in (3.1) ) , and this agree with the prediction of ref. [2].

Our result shows that when QDs are in high pressure, the pressure dependence of band edge is reduced, and this is the reason that the negative term is contained in equation (3.1). What cause this phenomenon? This means the lattice become more and more covalent with adding pressure. ( lattice become more and more covalency thus the electron-phonon interaction become weak ; reduce the pressure dependence of  $E_g$  ) We will discuss this effect with quantification in chapter3-2-2.

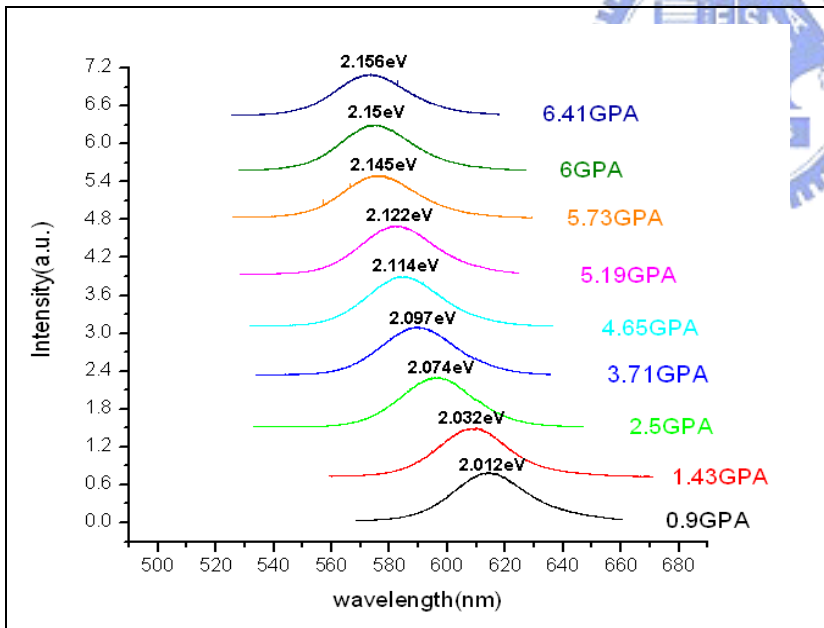


**Fig3-8 : The 5nm radius CdSe/ZnS QDs fluorescence patterns vs pressure. ( gotten in 1108 ) The number above peaks are the correspond energy of fluorescence.**

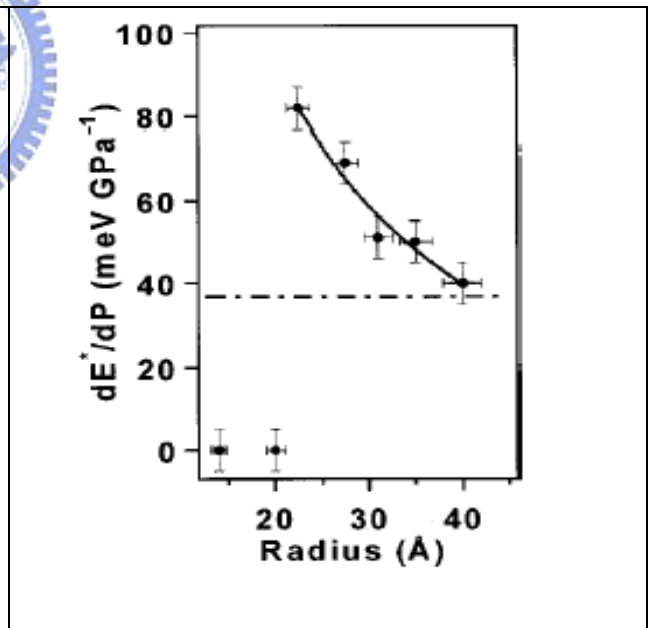


**Fig3-9 : The pressure parameter of different size CdSe QDs.<sup>ref2</sup> The pressure parameter of bulk CdSe is 37.5(meV GPA<sup>-1</sup>)**

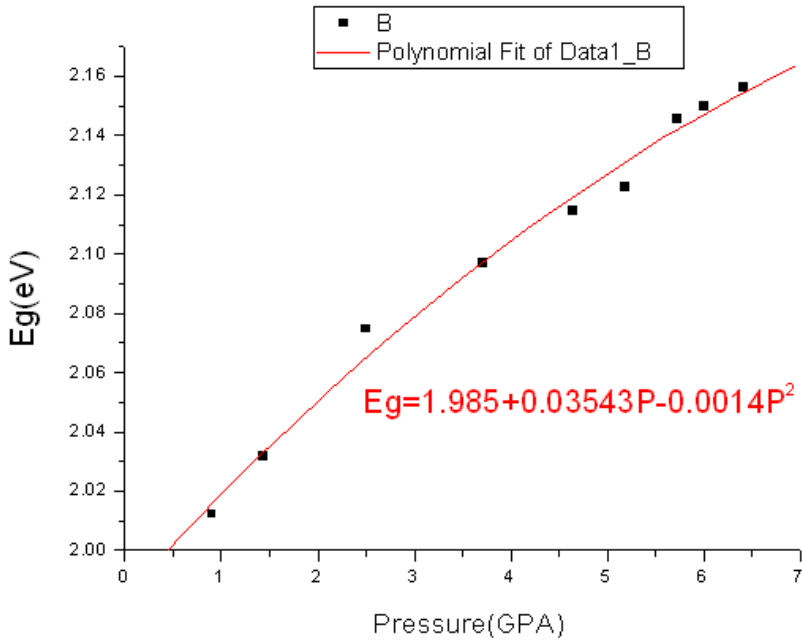


**Fig3-10 : Pressure dependence of band edge ( get from PL peak )in 5nm radius CdSe/ZnS QDs. The dot is the experiment data.**

**The red solid line is the fitting line of experiment data.**

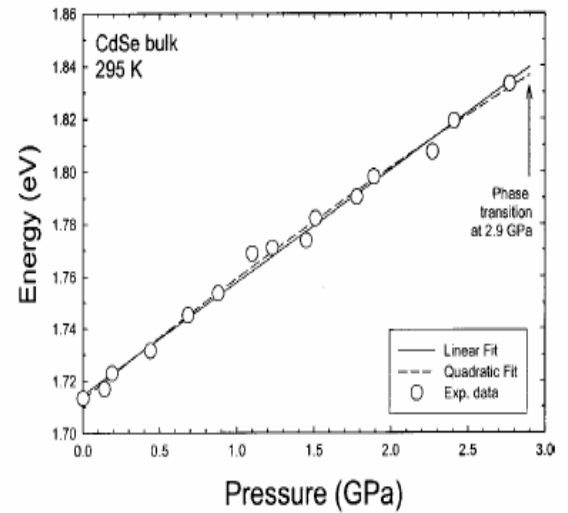


**FIG. 3.** Change of the band-gap energy of CdSe with pressure. The solid line is the best linear fit to the data. The dashed line represents the result of the best quadratic fitting.

**Fig3-11 : Pressure dependence of band edge in bulk CdSe at 295K.**<sup>ref5</sup>

**Phase transition happened at nearly 2.9GPa.**

### 3-1-3 Photon life time result

In this section, we will focus on the experiment data of PL spectrum and photon life time spectrum to investigate the relation between band edge and the radiative life time of QDs. In this experiment, we also study the pressure effect on the photon life time of QD. In our experiment, two different sizes QDs; i.e. 3.5nm radius ( emits yellow color  $\lambda = 530 \text{ nm}$  ) and 5nm radius( emits red color  $\lambda = 630 \text{ nm}$  )CdSe quantum dots and with 1nm thickness ZnS shell cladding are used.

**Fig3-12a, b** show the PL spectrum and life time spectrum under different pressures of 3.5nm radius QD. One can note that the  $E_g$  increases as the pressure is increased; the photon life time becomes faster as the  $E_g$  of QD is increased. (**Fig3-12b**)

For 5nm radius QD, the corresponding result of  $E_g$  and life time are presented in **Fig3-13a**、**b**.

We use a Gaussian curve to fit the PL peak and the fitted data is listed as shown in **Fig3-12b**、**3-13b**. In the fitting of photon life time, the vertical axis is in logarithmic

scale as shown in **Fig (b)**. The curves are then fitted, and the decay rates  $\tau$  are obtained.

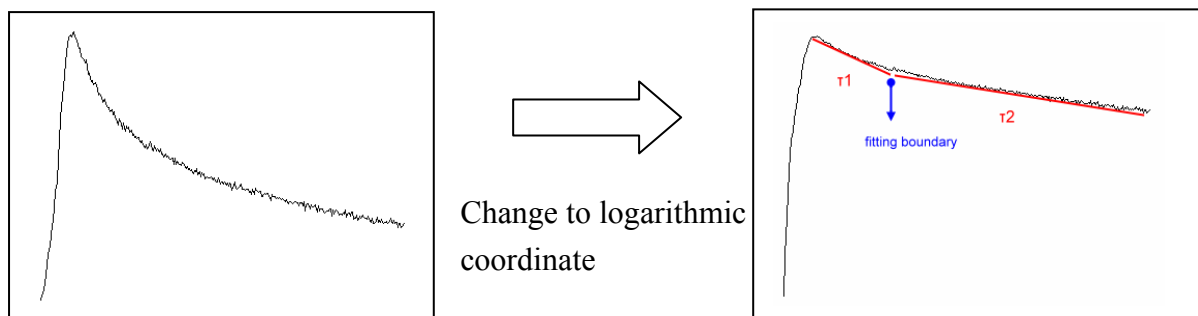


**Fig (a)**

**Fig (b)**

**Fig3-12b** and **Fig3-13b** show the obtained results for 3.5 and 5nm radius QDs. In **Fig3-12b**, one can find that life time  $\tau_1$  is slower and life time  $\tau_2$  is faster. For the 5nm radius QD, its photon life time spectrum is almost dominated by one time scale decay rate  $1/\tau_3$  as shown in **Fig3-13b**.

By following the previous published papers [ref.7], it is believed the one of the decay rate comes from the core state and another comes from the surface state. Thus for the large surface/volume atoms number ratio of our 3.5nm radius QD, two kinds of life times are needed. But for 5nm radius QD, thus only one decay rate is needed. (its volume/surface atoms number ratio is larger)  
The discussion will be given in chapter3-2-3.

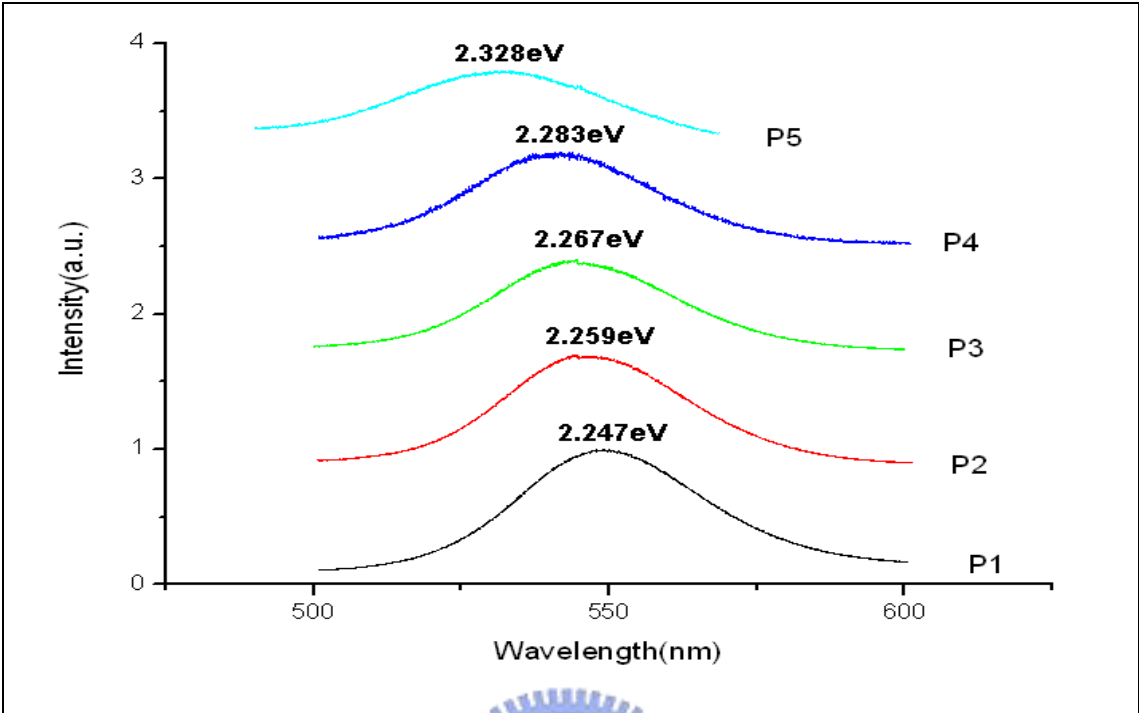


**Fig3-12a : The 3.5nm radius CdSe/ZnS QDs fluorescence patterns vs. pressure. (gotten in 1103)**

**The number above peaks are the correspond energy of fluorescence.**

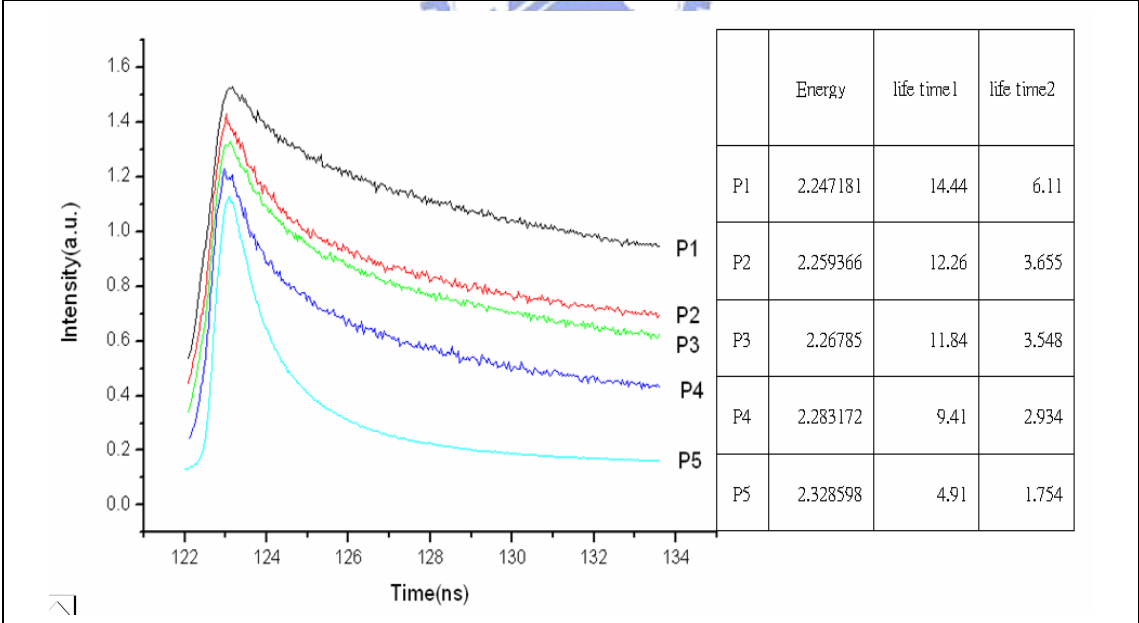


**Fig3-12b : Left : The life time spectrum under different pressure of the 3.5nm radius CdSe/ZnS QDs. (gotten in 1103)**

**Right : Table of band edge, life time1 and life time 2 which are fitted from experiment data.**

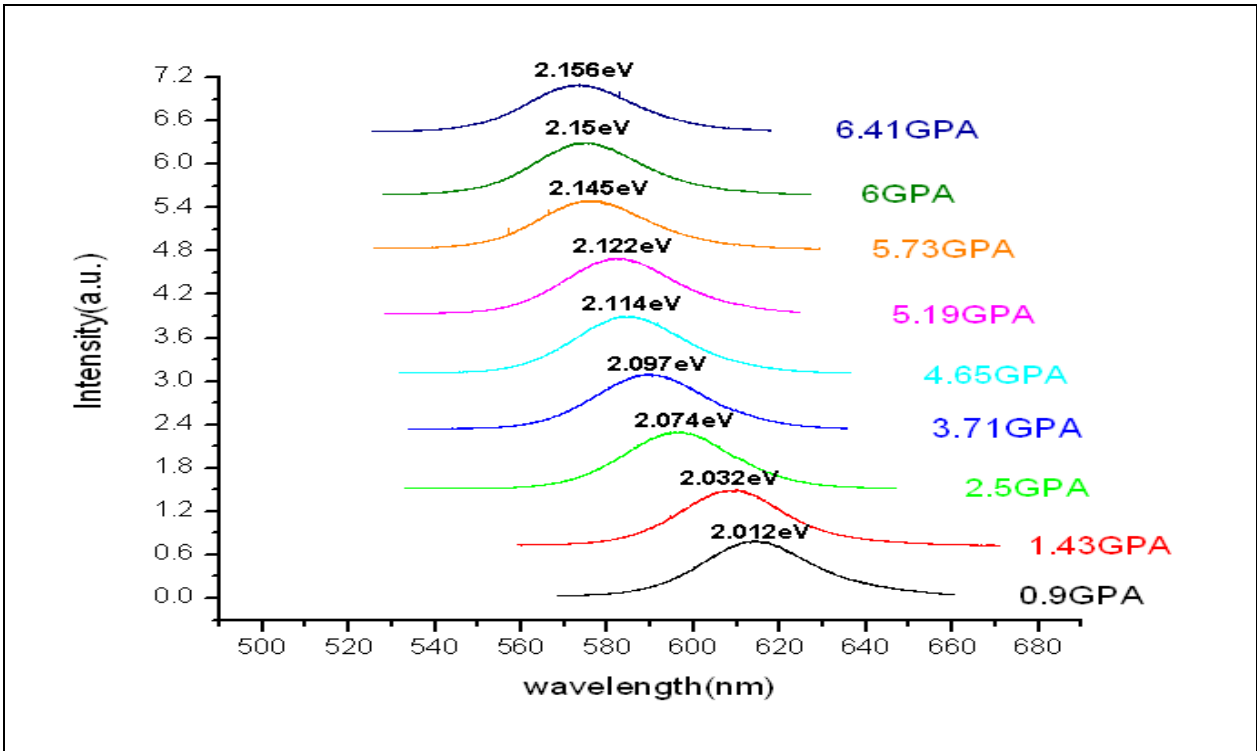


**Fig3-13a : This figure identical to Fig3-8.**

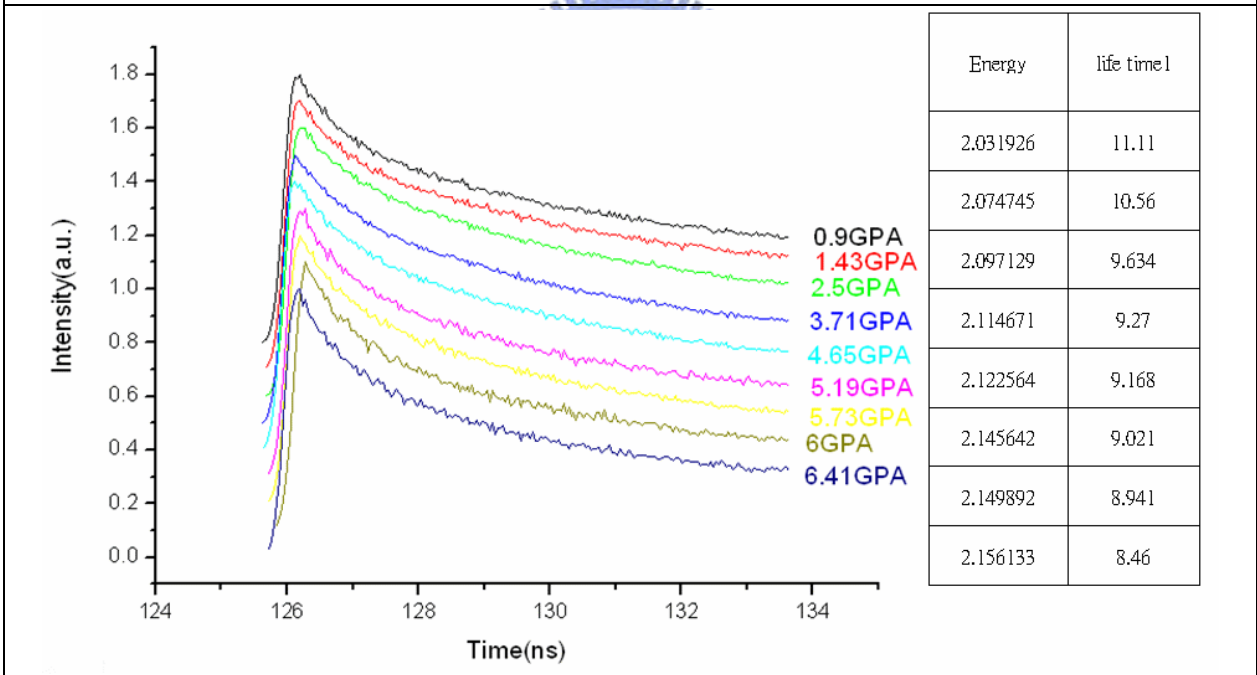


**Fig3-13b : Left : The life time spectrum under different pressure of the 5nm radius CdSe/ZnS QDs. ( gotten in 1108 )**

**Right : Table of band edge and life time which are fitted from experiment data.**



## 3-2 Discussion

### 3-2-1 Raman discussion

A Lorentzian form is used to fit the asymmetry spectrum as shown in **Figs3-2,3,4, 5**; the frequency of different phonon modes and the corresponding pressures are listed in **Table I**.

The loading (black) curve is compared with the unloading curve (red) as shown in **Fig3-15**; it can be found that these two curves are almost consistent with each other. This might be resulted from the reason that the ZnS shell doesn't perform phase transition in the loading/ unloading processes. Only the lattice constant of ZnS (zinc-blende structure) is compressed during the applying of pressure.

The relationships of mode frequencies versus pressure can be obtained by the quadratic polynomial formulae (3.2) \cdot (3.3) and (3.4) .

$$\text{CdSe } \omega_{LO} = 216.766 + 3.932P - 0.077P^2 \text{ (cm}^{-1}\text{)} \dots\dots\dots (3.2)$$

$$\text{CdSe } \omega_{2LO} = 416.569 + 10.057P - 0.398P^2 \text{ (cm}^{-1}\text{)} \dots\dots\dots (3.3)$$

$$\text{ZnS } \omega_{LO} = 268.71 + 9.17P - 0.0958P^2 \text{ (cm}^{-1}\text{)} \dots\dots\dots (3.4)$$

$$\text{Undetermined mode } \omega = 156.33 + 0P \text{ (cm}^{-1}\text{)}$$

From formula (3.2) \cdot (3.3) we can obtain the Grüneisen parameter  $\gamma_i$  from the following definition :

$$\gamma_i = -\frac{\partial \ln \omega_i}{\partial \ln V} = \frac{B_0}{\omega_{i0}} \frac{d\omega_i}{dp} \dots\dots\dots (3.5)$$

where the bulk modulus  $B_0$  is defined as the inverse of the isothermal compressibility (53 GPA for CdSe)

and  $\omega_i = \omega_{i0} + ap + bp^2$  is our fitting formula.

By substituting formula (3.2) \cdot (3.3) into (3.5), we find that the Grüneisen parameter  $\gamma_i$  of CdSe is a function of pressure :

$$\gamma_{LO} = \frac{B_0 = 53}{\omega_{i0} = 216.766} (3.93 - 0.077p) = 0.9608 - 0.0188p \dots\dots\dots (3.6)$$

$$\gamma_{2LO} = \frac{B_0 = 53}{\omega_{i0} = 416.569} (10.057 - 0.398p) = 1.279 - 0.05p \dots\dots\dots (3.7)$$

Grüneisen parameter can be viewed as the degree of interaction between the variations of Raman mode versus lattice constant. One can deduce the lattice is covalent or ionic by this parameter. In generally : if  $\gamma_i$  is small, the lattice is covalent ; if  $\gamma_i$  is large, the lattice is ionic.

In an ionic lattice, the polaron is easy to form i.e. electrons tend to attract the cation and exclude anion and form a quasi-particle-polaron; thus indicate strong electron-phonon interaction, and enhance the pressure dependence of polaron energy. This will be explained again in PL and Raman discussion.

From formula (3.6) · (3.7) we see the pressure tends to decrease the lattice ionization (become more covalent) due to the second negative term of  $\gamma_i$ . **Fig3-16a** is the diagram of Grüneisen parameter versus various sizes QD.<sup>ref2</sup> One can deduce the  $\gamma_{LO}$  of our experiment at nearly 7GPa is about 0.829 which is correspond to the 2.5nm radius QD in the covalent region in this diagram. We plot the Grüneisen parameter of CdSe LO and 2LO modes versus pressure in **Fig3-16b**; one can see both parameters decrease while loading the pressure and the lattice transmit from ionic region into covalent region.

CdSe : before phase transition I (1108data)			ZnS (1024data before PH I, 1108 after PH I)		ZnS decreasing pressure(1108data)		Undetermined Mode(after PH I)
Pressure(GPa)	CdSe LO(cm <sup>-1</sup> )	CdSe2LO(cm <sup>-1</sup> )	pressure(GPa)	ZnS LO(cm <sup>-1</sup> )	pressure(GPa)	ZnS LO(cm <sup>-1</sup> )	Independent of pressure added, peak position is always at 156.33 cm <sup>-1</sup>
0.37	218.433	420	3.17	300.19	28.22	452.13	
0.9	219.83	424.92	3.71	300.73	13.46	374.54	
1.43	221.87	430.09	5.6	312.48	10.39	360.64	
2.5	226.95	440.95	7.5	332.43	7.91	340.76	
3.71	230.87	448.44	8.32	335.87	6.96	319.55	
4.65	232.69	453.68	9.7	349.29	6.41	318.84	
5.19	234.06	456.19	12.48	373.33			
5.73	237.06	461.58	15.57	391.26			
6	238.14	464.09	17.42	396.33			
6.41	238.84	464.44	20.58	416.66			
			24.37	433.15			
			31.22	462.79			

**Table I : Lists of Raman peaks at various pressure in 5nm radius CdSe/ZnS QDs. The data of ZnS are composite of 1024 and 1108 data; others are come from the same day data.**

**PS : PH I means phase transition I.**

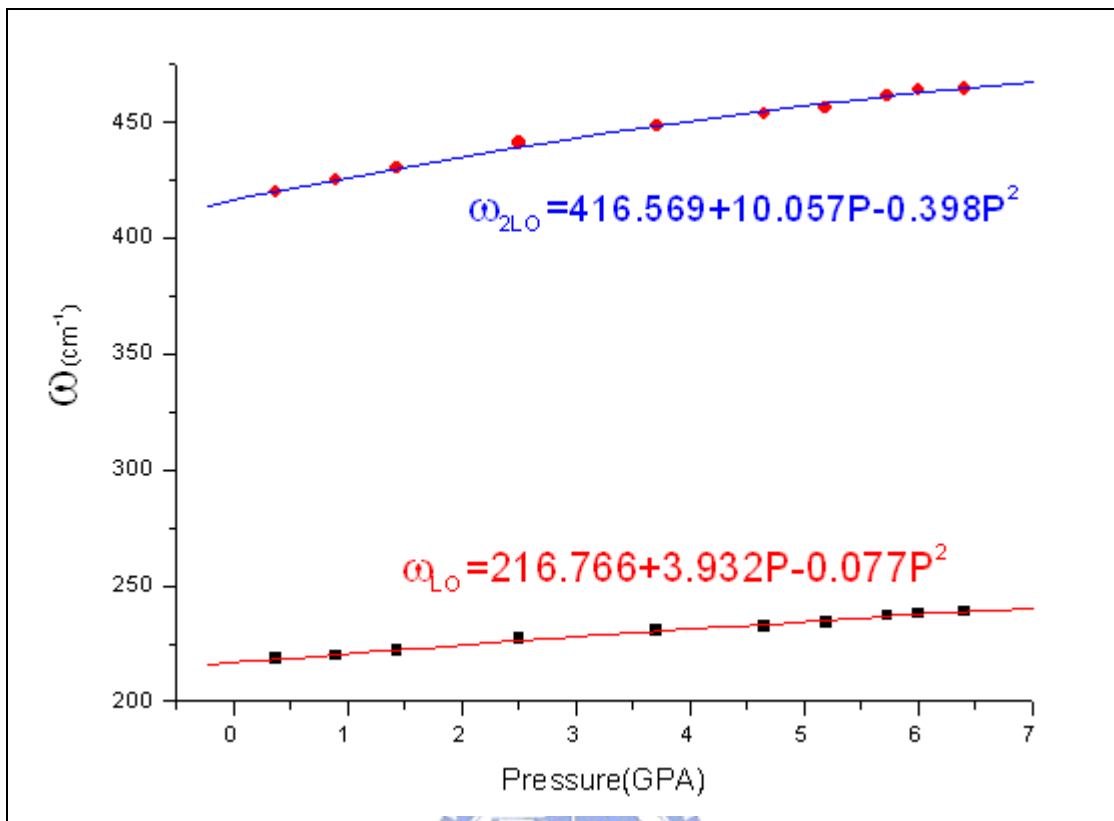


**Fig3-14 : Pressure dependence of CdSe LO and 2LO Raman peaks in 5nm radius CdSe/ZnS QDs. ( gotten in 1108 )**  
**The dots are experiment data. The solid lines are fitting curve.**

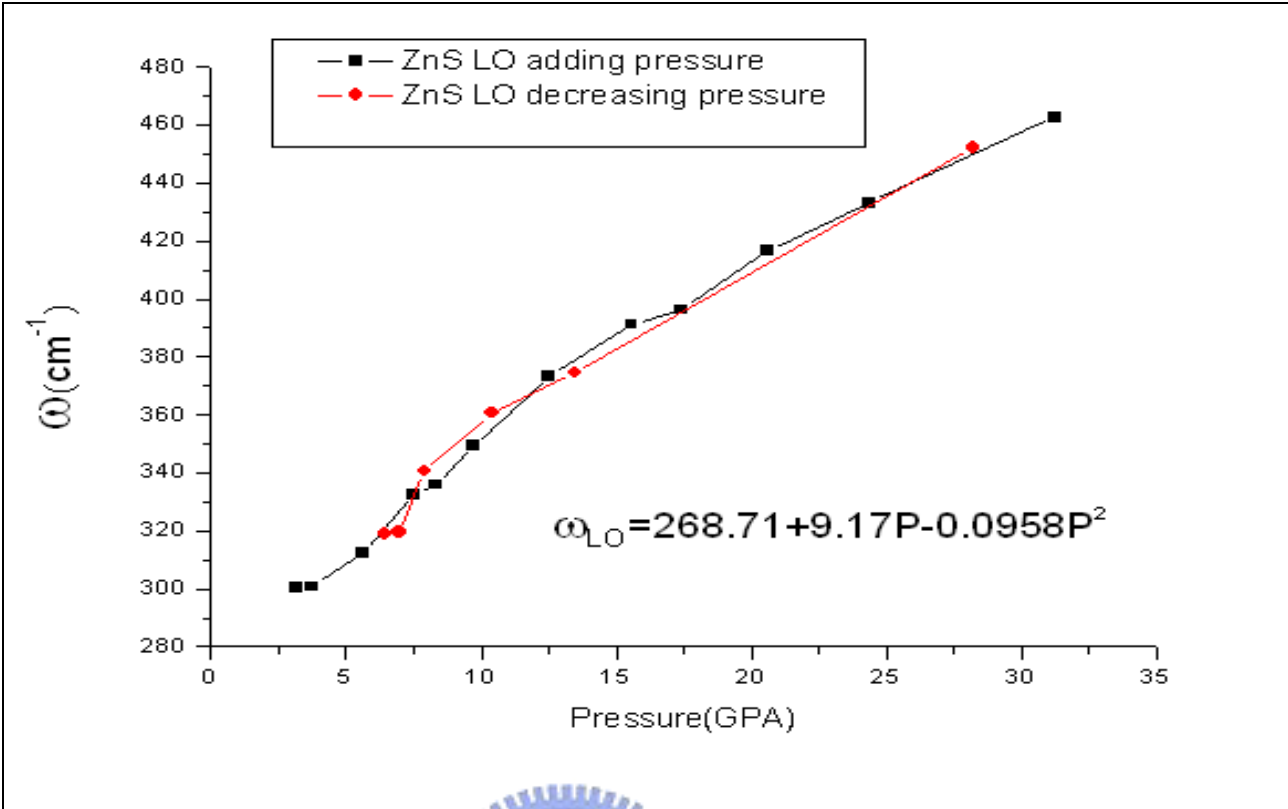


**Fig3-15 : Pressure dependence of ZnS LO Raman peaks in 5nm radius CdSe/ZnS QDs. (gotten in 1108)**  
 The dots are experiment data. The solid lines are guide to eyes.

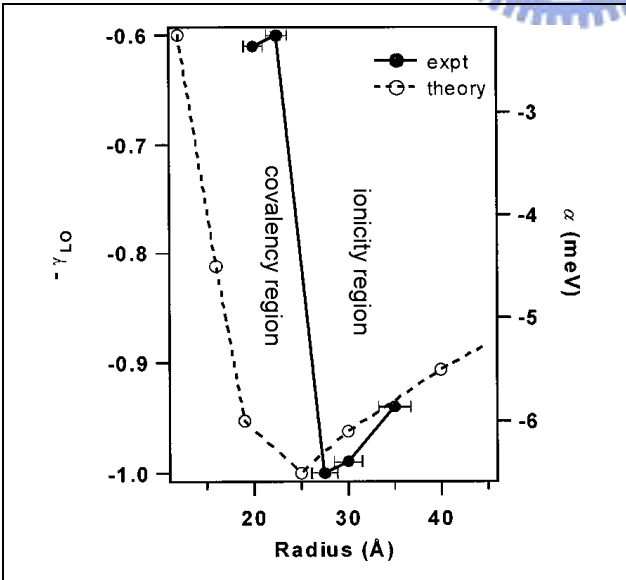


**Fig3-16a : The Grüneisen parameter (exp) and el-ph coupling constant (theory) versus CdSe QD's size.<sup>ref2</sup>**

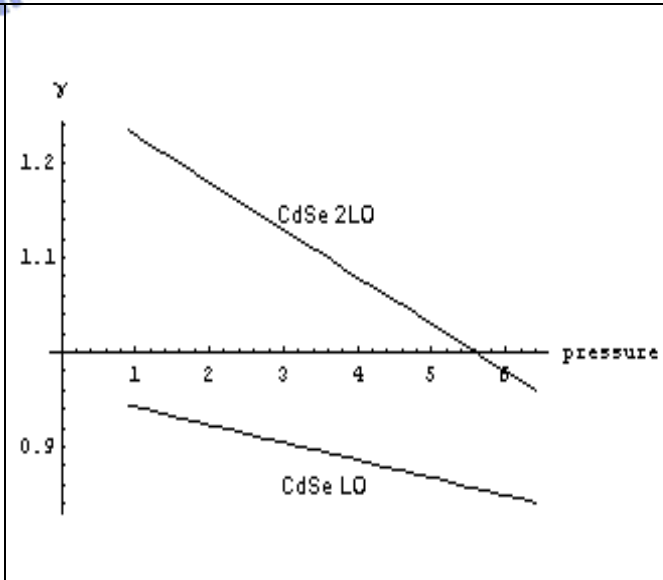


**Fig3-16b : The Grüneisen parameter of CdSe LO (down) and 2LO (up) mode in our 5nm radius CdSe/ZnS QDs.**

### 3-2-2 Raman and PL discussion

As we had explained in chapter 3-2-1 ; when loading pressure the lattice tends to become more covalent. This comes from the second negative term in Grüneisen parameter i.e.  $\gamma_{LO} = 0.9608 - 0.0188p$  and  $\gamma_{2LO} = 1.279 - 0.05p$ . One can see as the pressure is low  $\gamma_{LO} = 0.9608$ ; which is close to the bulk's value 1.1<sup>ref3</sup>, so they have very similar pressure dependence due to the same strength el-ph coupling. But when pressure is about 4 or 5 GPA, the negative term in  $\gamma_{LO}$  becomes non-ignorable ( $\sim 0.094$ ) and the value of  $\gamma_{LO}$  becomes 0.86 which is belonging to the region of covalent lattice.<sup>ref2</sup> The increase in lattice covalency means the polaron difficult to form, thus decrease the electron-phonon interaction. That is the reason why pressure increasing to high we see the pressure dependence of band edge becomes unapparent in QD.

Here, we here will bring up a simple model to explain roughly the data of PL versus pressure.

Imagine what would happen when a QD is under pressure? The effect is that first the lattice constant will be compressed and second is the lattice ionicity will be changed by pressure ; the later will influence the polaron energy in QD. The first effect ( the pressure induced electronic structure difference results in energy band edge shift ) can be simulated by the pressure induced band edge shift in bulk ; however the polaron energy changed by pressure is just the main topic of our model.

At first we write down the Hamiltonian of our model :

$$H = H_e + H_v + \Delta V1$$

$$= \frac{P^2}{2M} + \hbar\omega \int \frac{d^3K}{(2\pi)^3} a_K^+ a_K + i(\sqrt{2}\alpha\pi)^{1/2} \sum_K \frac{1}{K} [a_K^+ e^{-iK \cdot X} - a_K e^{iK \cdot X}]$$

where  $H_e$  is the electron Hamiltonian in solid with effective mass.

The second term is the phonon energy,  $a_K^+, a_K$  are the creation and annihilation operator of phonon with momentum  $\mathbf{K}$ .

The third term is the potential induced by lattice distortion ( polaron potential ) ,

$\alpha = 2 \frac{C}{\hbar\omega_L}$  is the coupling constant in  $\Delta V1$  that describes the el-ph coupling

strength, and C is the lattice deformation energy.  $\omega_L$  is the longitudinal optical phonon frequency of the lattice.

By using perturbation method (for small  $\alpha$ ) the eigenvalue difference except the part

of lattice structure is :  $\Delta E = -\alpha + 1.26\left(\frac{\alpha}{10}\right)^2$

Because  $\frac{1}{2}\alpha = \frac{C}{\hbar\omega_{LO}}$ , where  $\omega_{LO}$  is the vibration frequency of CdSe LO mode, thus

we can deduce  $\alpha$  from our Raman spectrum experiment and gives :

( substitute formula ( 3.2 ) into  $\omega_{LO}$  )

$$\alpha = \frac{2C}{\hbar(216.766 + 3.93p - 0.077p^2)} \quad \text{which is a function of pressure.}$$

Where the  $\frac{2C}{\hbar}$  is still an unknown parameter of our system.

Thus the total eigenvalue of the system is :

(ignore the phonon energy, because it is small)

$E = E_0(p) - \alpha + 1.26\left(\frac{\alpha}{10}\right)^2$ ,  $E_0(p)$  is the electron eigenenergy determined by lattice structure, and the other terms are the energy shift induced by polaron effect.

We assume  $E_0(p)$  is a linear function with pressure (  $E_0(p) = A + bp$  ) Because the “pressure screen effect” of ZnS shell, the inner part of QD reaches 3GPA while the outer pressure is 7GPA. We thus deduce the effective pressure parameter of QD is :  
(come from the structure difference contribution)

$$b = 0.0375 \times \frac{3}{6.4} = 0.0175 \text{ eV / GPA},$$

where the 0.0375eV/GPA is the pressure parameter comes from bulk CdSe experiment.

Thus the total eigenvalue becomes  $E = A + 0.0175p - \alpha(p) + 1.26\left(\frac{\alpha(p)}{10}\right)^2$

To find out the other unknown parameters, we do the differential : ( assume  $\alpha$  is small and ignore the  $\alpha$  square term )

$$\begin{aligned} \frac{\partial E}{\partial p} &= 0.0175 - \frac{\partial \alpha}{\partial p} = 0.0175 - \frac{2C}{\hbar} \frac{\partial(216.766 + 3.93p - 0.077p^2)^{-1}}{\partial p} \\ &= \frac{2C}{\hbar} (216.766 + 3.93p - 0.077p^2)^{-2} (3.93 - 0.077p) + 0.0175 \\ &= \frac{2C}{\hbar} \frac{(3.93 - 0.077p)}{(216.766 + 3.93p - 0.077p^2)^2} + 0.0175 \end{aligned}$$

From the data of PL experiment shown in **Fig3-10**, we know when  $p \doteq 0$  the slope of the experiment data is nearly 0.0354eV/GPA, substitute this value into the formula above it gives :

$$\begin{aligned} \left. \frac{\partial E}{\partial p} \right|_{p \approx 0} &= 0.0175 + \frac{2C}{\hbar} \frac{3.93}{(216.766)^2} = 0.0354 \\ \Rightarrow \frac{2C}{\hbar} \cdot 8.342 \times 10^{-5} &= 0.0179 \\ \Rightarrow \frac{2C}{\hbar} &= \frac{0.0179}{8.342 \times 10^{-5}} = 214.57 \end{aligned}$$

Therefore, the unknown constant  $\frac{2C}{\hbar}$  is determined.

Thus we can obtain a formula to predict the band edge of QDs changed by pressure

$$E(p) = A + 0.0175 p - \alpha(p) = A + 0.0175 p - \frac{214.57}{(216.766 + 3.93 p - 0.077 p^2)} eV$$

.....(3.A)

Although we still don't know the initial energy of the system i.e. A, but we can choose a proper value of A to fit the data of the curve in **Fig3-10**. We plot this equation in **Fig3-17** in a pressure range 0.9~6.4GPa to compare the experiment data as shown in **Fig3-10**. One can see when pressure is high; the curve tends to be smooth just as the experiment data shows. The smoothness comes from the polaron energy, and the smaller polaron energy comes from the lattice covalency. Thus, the lattice covalence effect makes the band edge-pressure curve in QDs become smooth at high pressure.

The polaron effective mass defined as  $m_{pol}^* \cong m^* \left( \frac{1 - 0.0008\alpha^2}{1 - \frac{1}{6}\alpha + 0.0034\alpha^2} \right)$ , and the plot it

versus pressure is shown in **Fig3-18**. One can easily see the higher the pressure the lighter the effective mass, which is another evidence that the lattice of QDs becomes more and more covalent while loading pressure.

Finally we compare both the Grüneisen parameter and el-ph coupling constant versus pressure, the former is deduced from the experiment and the later is deduced from the theorem, one can see both of them has the same tendency with adding pressure ; i.e. the lattice becomes more and more covalent. The figure is shown in **Fig3-19**.



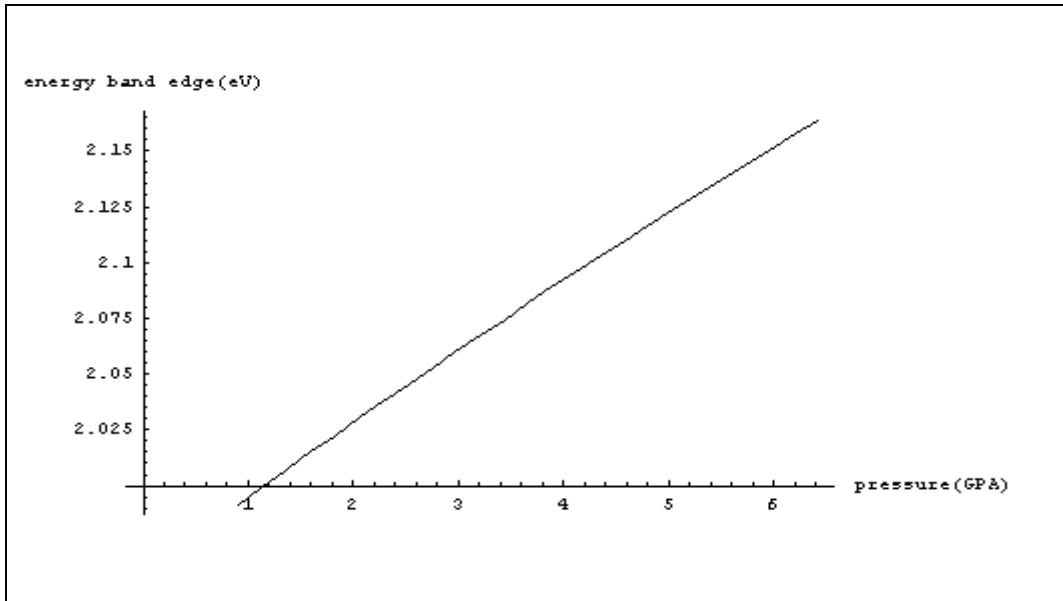


**Fig3-17 : The plot of formula (3.A)**  
**This curve tend to be smooth at high pressure, one can compare this cure to experiment data shown in Fig3-12.**

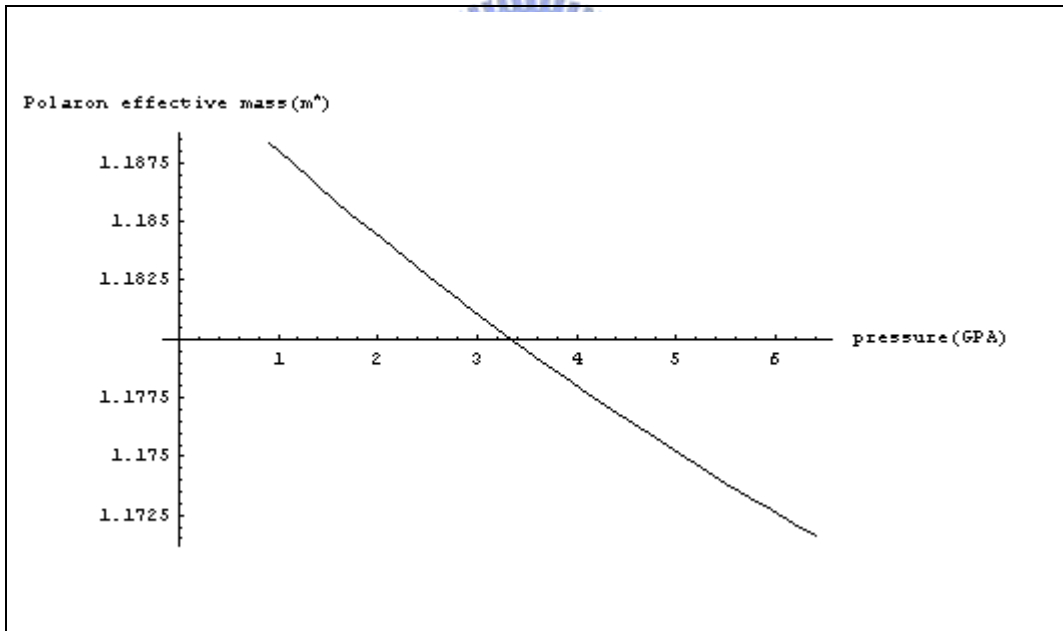


**Fig3-18 : Pressure dependence of polaron effective mass.**

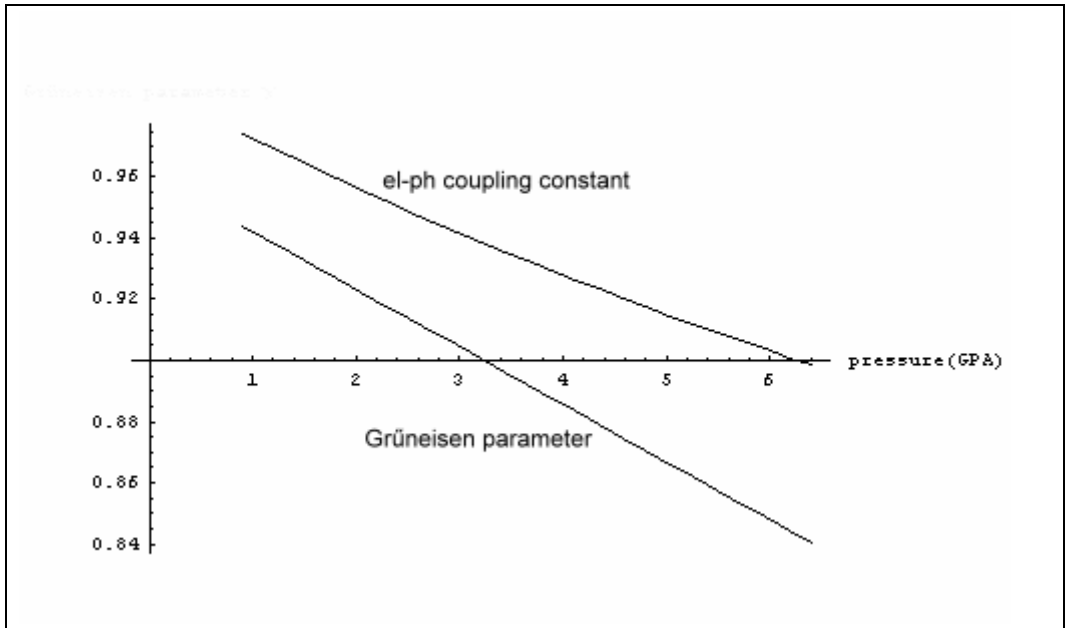


**Fig3-19 : Pressure dependence of Grüneisen parameter and el-ph coupling constant in our experiment.**

**Both of them show lattice become more covalency at high pressure.**

### 3-2-3 Life time discussion

In this chapter we also try to use a simple model to discuss our experiment data. From Einstein A coefficient which describes decay rate in a two level atom, we have (see chapter 4-4)

$$\frac{1}{\tau} = \frac{w_0^3 |d|^2}{3\pi\epsilon_0 \hbar c^3} \dots\dots\dots (3.8)$$

where  $1/\tau$  is the population decay rate, and  $\hbar w_0 = E_g$  is the gap between two lowest levels,  $d$  is the dipole moment formed by electron and proton in a atom.  $\epsilon_0$  is the dielectric constant in vacuum.

We assume that the decay behavior of every single electron in QD can be described by this formula.

This decay rate formula is not sufficient to describe the radiative decay rate of a QD system. Apply the exciton theorem to a case of spherical confirm potential in solid, we can derive another useful formula of radiative decay rate in QD.<sup>ref4</sup> Because the problem of an exciton in semiconductors with additional confirm potential can be solved by the envelope function approximation. (EFA) Use the envelope function method in a spherical confirm potential system, and solved an envelope function of an

exciton in this system can give as

$$\Psi_{nlm}(R, r) = F_{nlm}(R, \theta, \phi)\Phi_0(r)$$

where  $\Phi_0(r)$  denote the relative motion of electron and hole in the lowest exciton state and

$$F_{nlm} \text{ is the center of mass motion : } F_{nlm} = Y_{lm}(\theta, \phi) \frac{\sqrt{2}}{R_0 \sqrt{R}} \frac{J_{l+1/2}(k_{in} R)}{J_{l+3/2}(k_{in} R_0)}$$

$Y_{lm}$  : spherical function ,  $J_\nu$  : Bessel function of  $\nu$  th order.

The exciton-photon interaction Hamiltonian can be described by the dipole

approximation :  $\vec{d} \cdot \vec{E}(R, t)$  and the dipole moment  $\vec{d}$  of the optical allowed (n00) exciton is

$$\vec{d}_{00} = \langle \Psi_{n00} | \sum_i (-er_i) | \Psi_g \rangle = \mu_{cv} \Phi_0(0) \frac{2}{n} \left[ \frac{2}{\pi} \right]^{1/2} R_0^{3/2}$$

where  $\mu_{cv}$  is the transition dipole moment between relevant conduction band and valence band of bulk.  $R_0$  is the radius of QD. (or radius of the confining potential)

Using Fermi's golden rule as follow :

$$\Gamma = \frac{2\pi}{\hbar} \sum_k \left| \langle \Psi_g | H' | \Psi_{100} \rangle \right|^2 \delta(E_{100} - \hbar\omega_k) = 64\pi \left[ \frac{R_0}{a_B} \right]^3 \gamma_s \dots \dots \dots (3.9)$$

$H'$  :  $\vec{d} \cdot \vec{E}(R, t)$  Hamiltonian ,  $a_B = \frac{4\pi\epsilon_0\epsilon_b\hbar^2}{m_0m_e^*}$  : effective Born radius ,  $\gamma_s$  is a

constant. ( $\hbar\gamma_s \equiv 4|\mu_{cv}|^2 / 3\lambda^3$ ) where  $\lambda$  is the wavelength of emission ,  $\Gamma = \frac{1}{\tau}$  is the stimulated radiative decay rate of this model.

Combine the equation (3.8) and (3.9) , the real decay rate in a QD should be :

$$\Gamma_{total} = \Gamma_{spontaneous} + \Gamma_{stimulated}$$

where  $\Gamma_{spontaneous} = \text{formula (3.8)} \sim E_g^3$

$$\Gamma_{stimulated} = \text{formula (3.9)} \sim E_g^3 \left( \frac{R_0}{a_B} \right)^3$$

$$\text{Thus } \Gamma_{total} \sim E_g^3 \left[ 1 + B \left( \frac{R_0}{a_B} \right)^3 \right] \dots \dots \dots (3.10)$$

where B is a constant.

From this formula we can know the decay rate is roughly proportion to  $E_g^3$ .

Due to the effective born radius appearing in (3.10), we must explain this parameter. For wide band gap semiconductors it is useful to use the one band model(base on **k • p theorem**) to get the relation between  $E_b$  (band gap of semiconductor) and the effective mass of electron  $m^*$  :

$$m^* = \frac{m_0}{1 + E_p / E_b} \dots \dots \dots (3.11)$$

Where  $E_p \equiv \frac{2(P_{cv})^2}{m_0}$ ,  $P_{cv} = \langle c | \hat{p} | v \rangle$  is the momentum matrix element between the states of conduction band and valance band in solid. Notice that  $E_b$  is determined by electronic structure of lattice, not from the energy of PL peak. From formula (3.11), one can find that  $E_b \uparrow$ ,  $m^* \uparrow$  and  $E_b \downarrow$ ,  $m^* \downarrow$ .

Since  $E_b$  is the band gap determined from structure difference, when loading pressure we can substitute the formula of bulk  $E_b = A + 0.0175p$  into formula (3.11).

The  $R_0^3$  term appearing in formula (3.10) can also be replaced by pressure parameter too. Due to  $R_0$  is the range of the confinment potential:  $R_0^3 \sim V_{QD}$  and in principle we don't know how volume of QD changed with pressure; even though, we still can use a bulk parameter to substitute into.

The relation between pressure and volume of primitive cell in bulk CdSe<sup>ref5</sup> can be expressed as  $p = (B / B')[(V_0 / V)^{B'} - 1]$

where B is the bulk modulus of wurtzite CdSe and  $B'$  is the pressure derivative ( $= dB / dp$ ),  $V_0$  is the volume of primitive cell at atmospheric pressure.

Use the reported value  $B = 53 \text{GPa}$  and  $B' = 0.48$  as obtained by previous works [ref.5],

we get the Volume as an function of pressure as :  $V = \left( \frac{110.41}{p + 110.41} \right)^{\frac{1}{0.48}}$  in unit of

$$V_0^{0.48}$$

Because  $R_0^3 \sim V_{QD} \sim V$ , take all above result into account, we can rewrite (3.10) as :

$$\Gamma_{total} \sim E_g^3 \left[ 1 + B \left( \frac{R_0}{a_B} \right)^3 \right] = E_g^3(p) \left( 1 + c(m^*)^3 \left( \frac{110.41}{p+110.41} \right)^{\frac{1}{0.48}} \right)$$

$$= E_g^3(p) \left( 1 + c \left( \frac{m_0}{1 + E_p / E_b} \right)^3 \left( \frac{110.41}{p+110.41} \right)^{\frac{1}{0.48}} \right)$$

where c is an unknown constant.

Substitute  $E_b=A+0.0175p$  into this formula, thus the slope of the curve of decay rate versus  $E_g^3$  gives :

$$\left( 1 + c \frac{m_0^3}{\left( 1 + \frac{E_p}{A + 0.0175p} \right)^3} \left( \frac{110.41}{p+110.41} \right)^{\frac{1}{0.48}} \right), \text{ where } A \sim 1.7\text{eV} \dots \dots \dots (3.12)$$

The second term with 1/0.48 power in formula (3.12) can be ignored, because the pressure is increased from 0.9 GPa to 6.5GPa, in this range  $\left( \frac{110.41}{p+110.41} \right)$  can be approximated as 1.

From formula (3.12) one can easily see that when p is large enough, the term with power 3 in denominator dominates and the denominator becomes smaller while pressure increases ; thus show the slope becomes sharper.

In order to manifest the validity of the formula of the radiative decay rate derived above, the curve of  $1/\tau_1, 1/\tau_2$  versus  $E_g^3$  are plotted in **Fig3-14a** and **Fig3-14b** for 3.5nm radius QD. **Fig3-15** is for 5nm radius QD. The slope of the curve of  $1/\tau_1$  and  $1/\tau_2$  versus  $E_g^3$  are not the same; the latter is larger than the former.

One can see from **Fig3-14a** and **Fig3-15**, all of the fitting curves have positive square terms which make the curve sharper in high pressure. This phenomenon corresponds to our prediction.

If we compare the life times  $\tau_1$  and  $\tau_3$  come from the core state in two kinds of QDs; the slopes are not the same for different QD. ( See **Fig3-14a** and **Fig3-15** )

The slope of  $1/\tau - E_g^3$  curve in 3.5nm radius QD is about 0.10805 1/eV<sup>3</sup>ns and in 5nm radius QD is about 0.0151 1/eV<sup>3</sup>ns. This result is not so surprised due to our radiative decay rate prediction :  $\Gamma = \frac{1}{\tau} \sim E_g^3 \cdot m_e^{*3}$  Because the QD with 3.5nm radius

has more wide band gap than 5nm radius QD, thus the effective mass of 3.5nm radius QD is lager than it in 5nm radius QD. That is why the wide band QD ( 3.5nm radius

QD) has a sharper slope of  $1/\tau - E_g^3$  curve than narrow band QS.

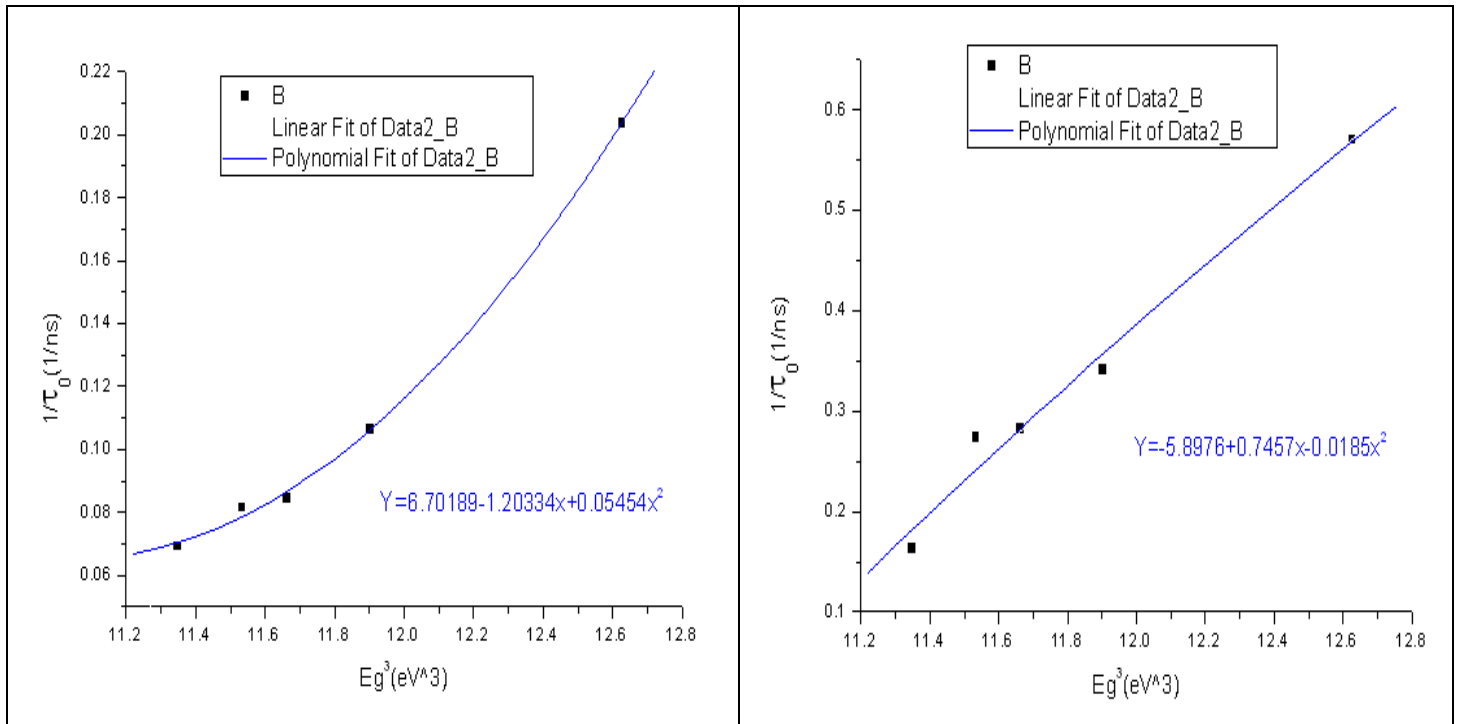


**Fig3-14a : Decay rate ( $1/\tau_1$ ) shift with of energy band edge<sup>3</sup> in 3.5 nm radius CdSe/ZnS QDs.**

**Fig3-14b : Decay rate ( $1/\tau_2$ ) shift with of energy band edge<sup>3</sup> in 3.5 nm radius CdSe/ZnS QDs.**

**This decay rate may come from the surface state.**

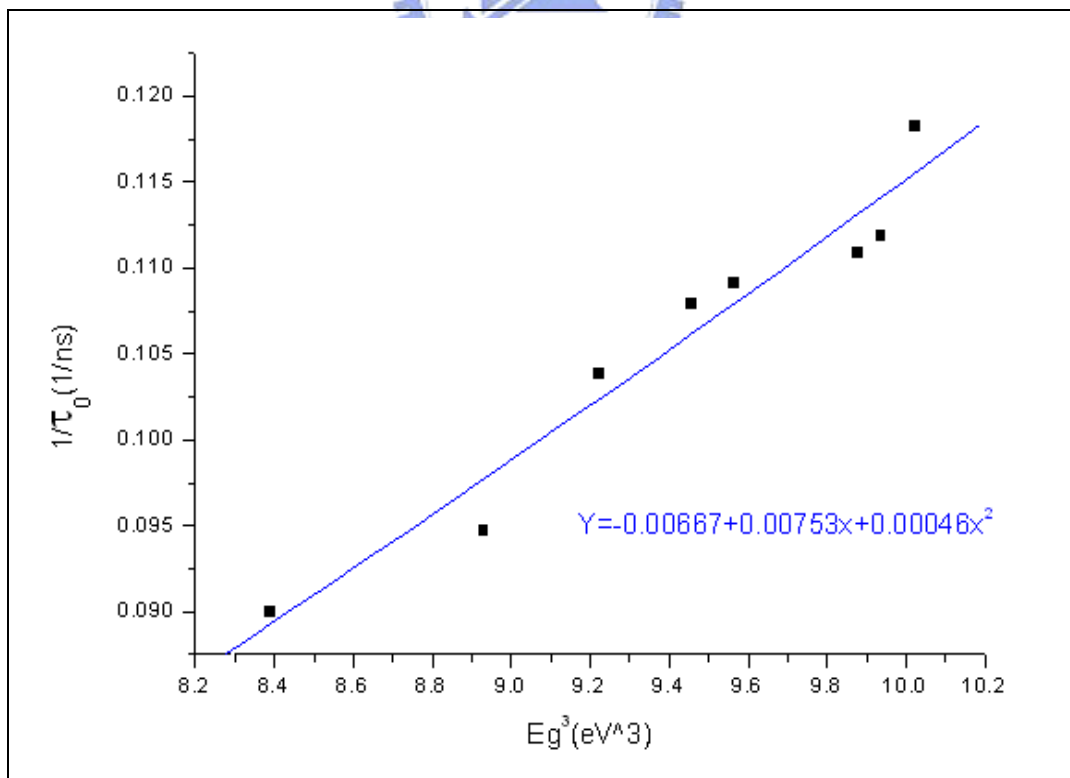


**Fig3-15 : Decay rate ( $1/\tau_3$ ) shift with of energy band edge<sup>3</sup> in 5 nm radius CdSe/ZnS QDs.**

## Part II : THEORETICAL CALCULATION

### Chapter4 : Electrons structure of QD

#### 4-1 The concept of constructing Diamond structure QD

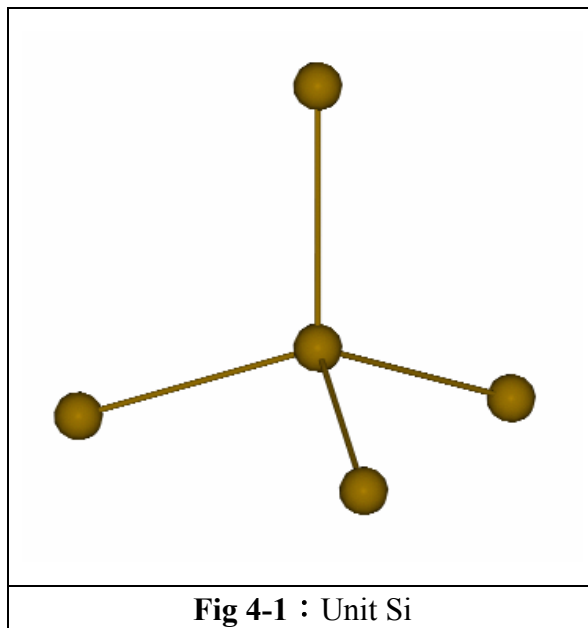
##### model

We follow Zhao's work proposed by ref. [6] of constructing the silicon QDs. From their work, the dodecahedron is taken as a core and is connect many colossal tetrahedrons (formed by many silicon units) on its 12 apexes and finally forms a giant "similar Icosahedra".

**Fig 4-1** is the silicon unit.

According to the ref. [6], procedure of constructing QDs is as follows :

1. Construct a polyhedron core.  
( they choose a dodecahedron in their work )
2. Build a giant silicon tetrahedron for a cell by piling silicon unit layer by layer.
3. Connect many cells on the apexes of core.





There are several constraints while constructing QD model as below :

- a. Apexes of the polyhedral core should have the body center symmetry
- b. Every atom in the apexes of the polyhedral core must bond to four atoms nearby and has  $109^\circ$  angle between each others. ( because silicon atom has four valence electrons ) ←**This would confine the structure of core.**

In the following we will discuss the structure of QD with a dodecahedron core.

### 4-1-1 Dodecahedron core

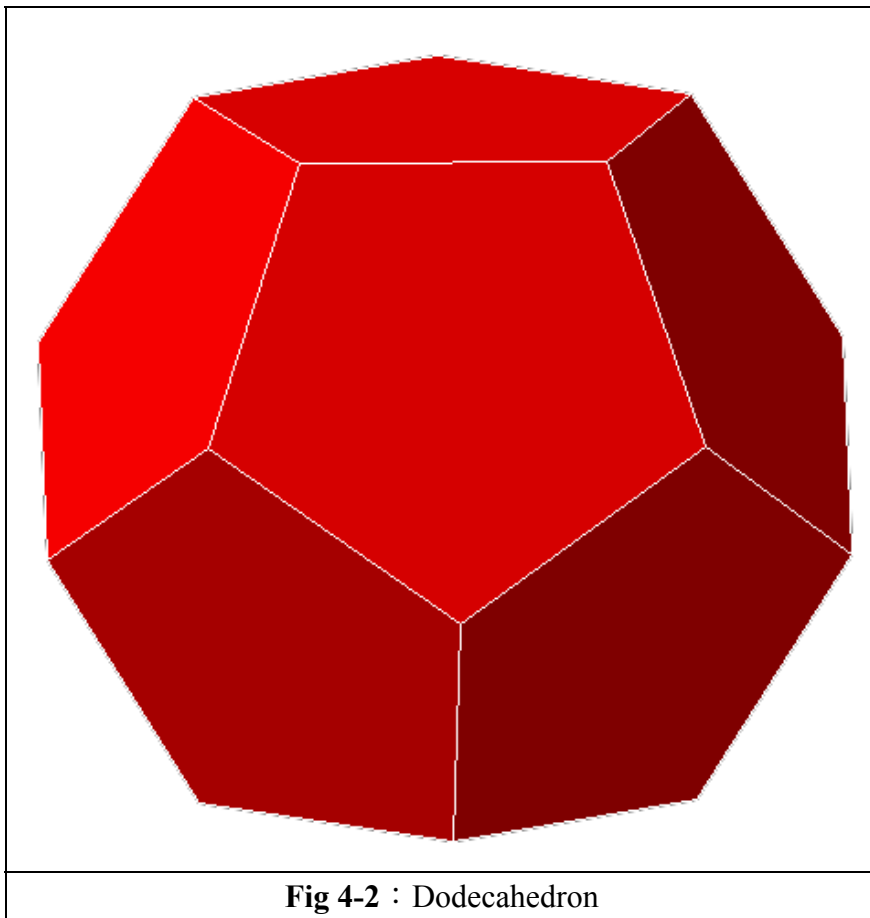


**Fig 4-2** is a dodecahedron. Let us discuss what would form when it is connected with different size tetrahedron cell on its apexes.

### 4-1-2 smallest size tetrahedron cell

When 20 apexes of the dodecahedron core are fully connecting with the smallest size tetrahedron cells, there are several properties that we need to remark.

First, this structure is a single layer QD with “similar Icosahedra” outward appearance which is formed by 20 silicon unit ( smallest size tetrahedron cell ) illustrate in **Fig 4-3**,

notice the black triangles in **Fig 4-3** form a Icosahedra. Secondly, this structure appears pentagon shape ( the red tape in **Fig 4-3** ) on the apexes of Icosahedra instead of a single atom on a real Icosahedron's. ( that is why it called “similar Icosahedra” ) . Finally, this structure has been a similar sphere shape in our first step.

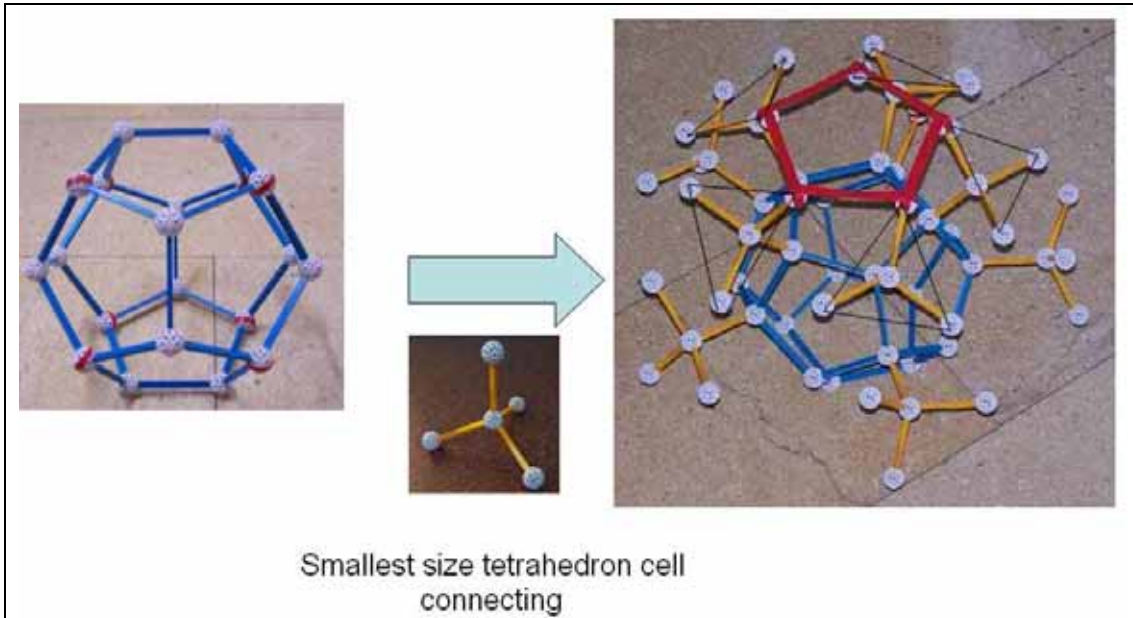


**Fig 4-3** : The upper part of core connects with many smallest size tetrahedron cell.

### 4-1-3 middle size tetrahedron cell

When the 20 apexes of dodecahedron core are fully connecting with middle size tetrahedron cells, it form a “similar Icosahedra” the same as the smallest size connecting case. This structure is also formed with 20 tetrahedrons (middle size now) and has pentagon shape on its apexes too. The blue tape in **Fig 4-4** is the outward appearance of the Icosahedra and the red tape is the pentagon shape in the apexes. Note that the size of pentagon ring is the same as it in Fig 4-3 ( single layer QD case ) . Finally, the size of this QD is bigger than the former because it is two layers thickness now. However these two QDs are with the same shape but different size.

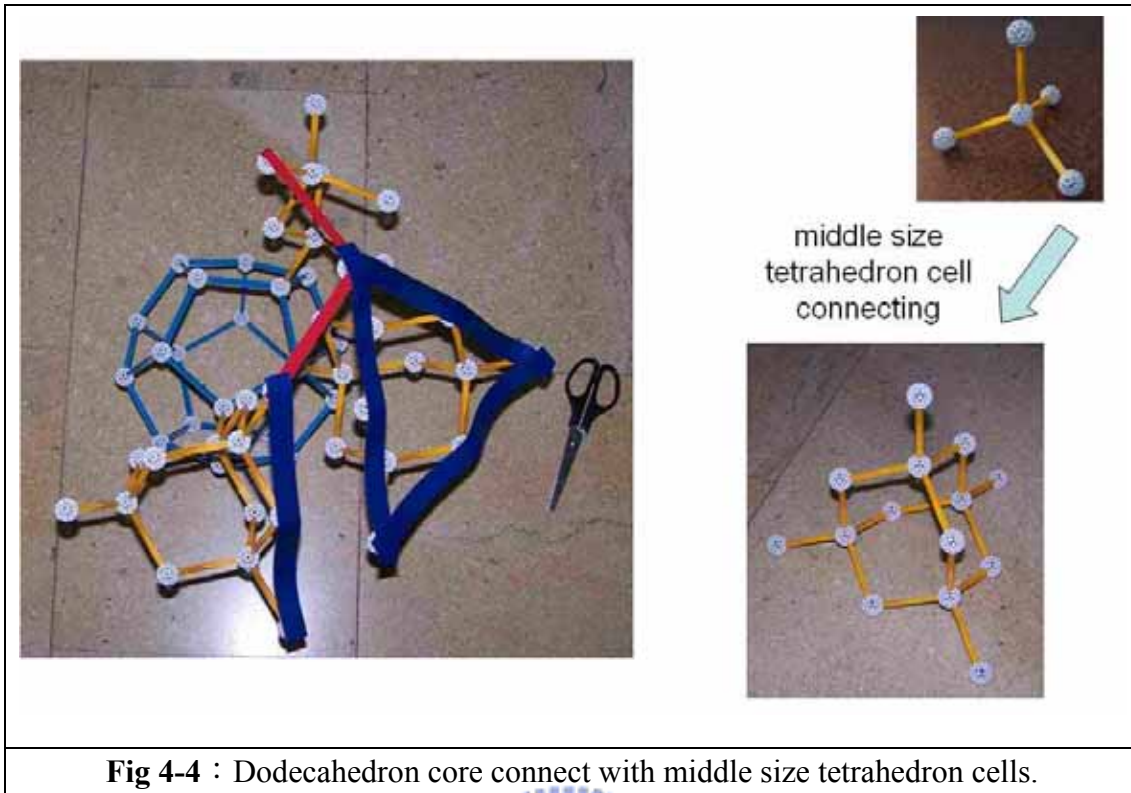


**Fig 4-4** : Dodecahedron core connect with middle size tetrahedron cells.

#### 4-1-4 giant size tetrahedron cell

In this PRL paper the giant size tetrahedron cell is chosen for constructing their QD. They take the giant size tetrahedron (three layers Si unit, **Fig 4-5c**) for a cell and connect it to core and finally formed a giant “similar Icosahedra” shown in **Fig 4-5a**. In **Fig 4-5b**, we see the final outward appearance of this structure. There are several advertences below :

1. Take care that in **Fig 4-5a**, the pentagon rings ( orange color ) are all equal size just as it being in one layer, two layer QD, and note that the red color shape in the center of Icosahedra is the dodecahedron core.
2. In Fig4-5c, the entire orange atoms form pentagon ring in Fig 4-5a and Fig 4-5b. The red atom in Fig4-5c form a core in Fig 4-5a and the blue atom form giant triangles in the exterior of the Icosahedra shown in Fig 4-5b.
3. Fig 4-6 shows a compositive comparison of the dodecahedron core connects with different size tetrahedron cells and form different size QDs.

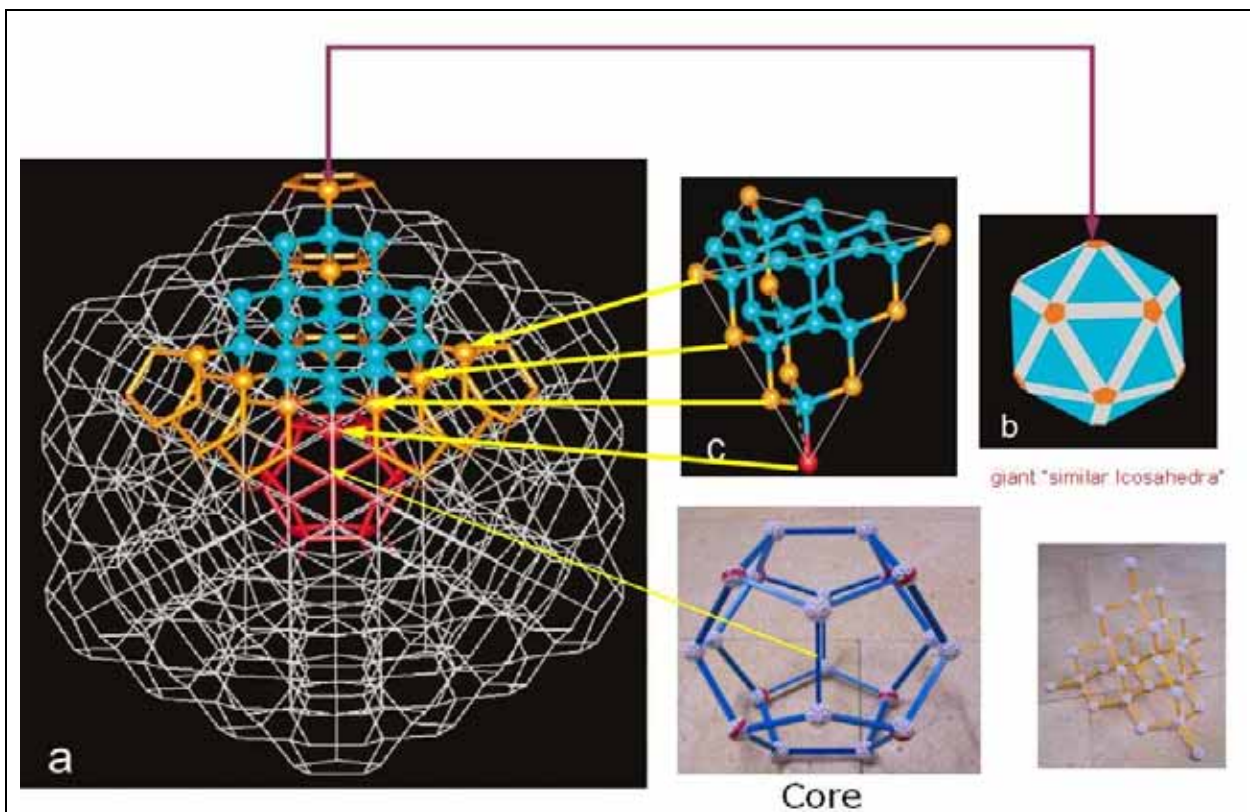


**Fig 4-5 :** Giant size tetrahedron cells (c) connect to core form a giant “similar Icosahedra” (a). And (b) is its outward appearance.

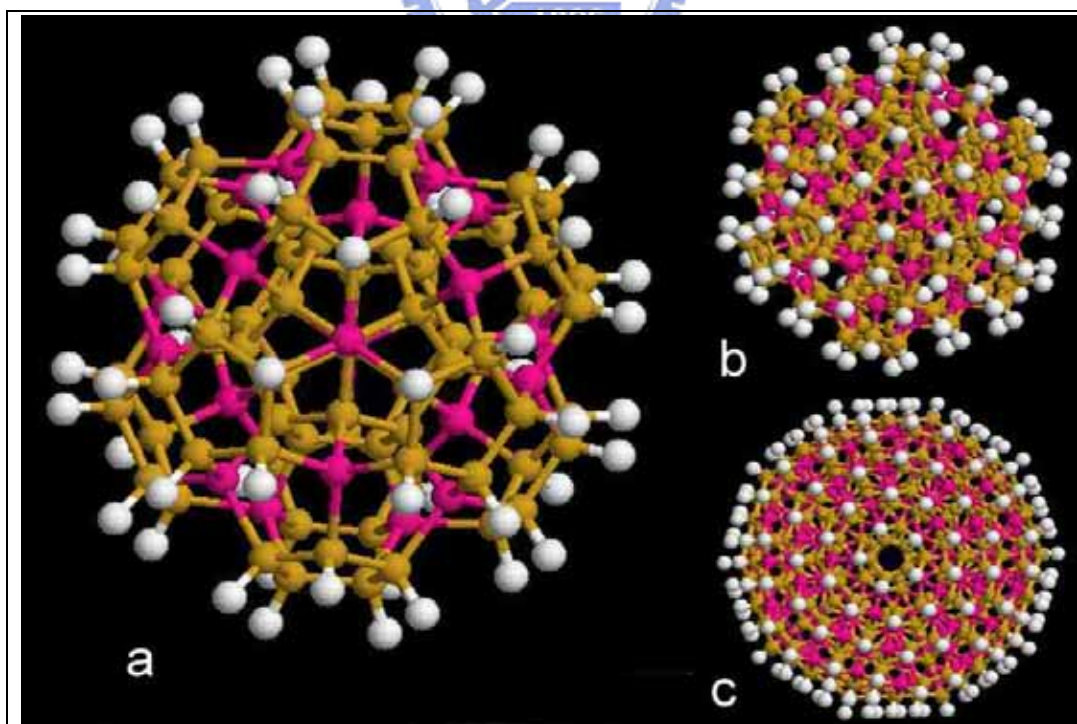


**Fig 4-6 :** The comparison of different size QD (connect H atoms).  
 Pink color : Cd atom    Yellow color:Se atoms    White color:H atoms  
 a:1 layer QD    b:2 layer QD    c:3 layer QD



## 4-2 Model a bulk like QD from small to big

Fig4-6 is the silicon quantum dot with the same shape but different size. Due to the structure constraint of CdSe QDs which is explained in Appendix D, i.e: the bulk like structure is the reasonable choice for CdSe QDs. For this reason, could we construct a bulk like QD with the same shape but different size? For this purpose we develop two types model of QDs. We label these two QDs as QDa and QDb.

Before our procedure of constructing QD model one need to know the primitive polyhedron we used to cut is the primary tetrahedron  $ijkl$  shown in **Fig 4-7**.

For QDa kind we cut four tetrahedrons on four apexes of the primary tetrahedron, then it formed a octahedron inside the original tetrahedron ( see  $a,b,c,d,e$  in **Fig 4-7** ), then we select all the middle point at eight sideline of this octahedron, and cut six pyramids along the wirings of these middle points ( ex : line  $fg,gh,hg\dots$  ) on six apexes of octahedron. Therefore it finally forms the yellow polyhedron in **Fig 4-7**.

There are something need to remark. See line  $ac$  in **Fig 4-7**, we should divide it into two parts, thus line  $ac$  is requested to be at least two units CdSe long to make sure that is dividable. For this reason, the length of line  $ij$  should be double of line  $ac$  ( being four unit CdSe long ) , thus the smallest cut able primitive tetrahedron is  $4\times 4\times 4$  unit CdSe tetrahedron. The next allowed lengths of line  $ac$  is 4, 6, 8, 10 and so on, all they can be divide into two parts. So the allowed cut able primitive tetrahedron is follow by  $8\times 8\times 8, 12\times 12\times 12, 16\times 16\times 16, 20\times 20\times 20$  unit CdSe.

**Fig 4-8** are the QD models cut from  $4\times 4\times 4$  and  $8\times 8\times 8$  primitive tetrahedron. We can easily see the size of QDa models growth up with the same shape ; completely accordance with our purpose.

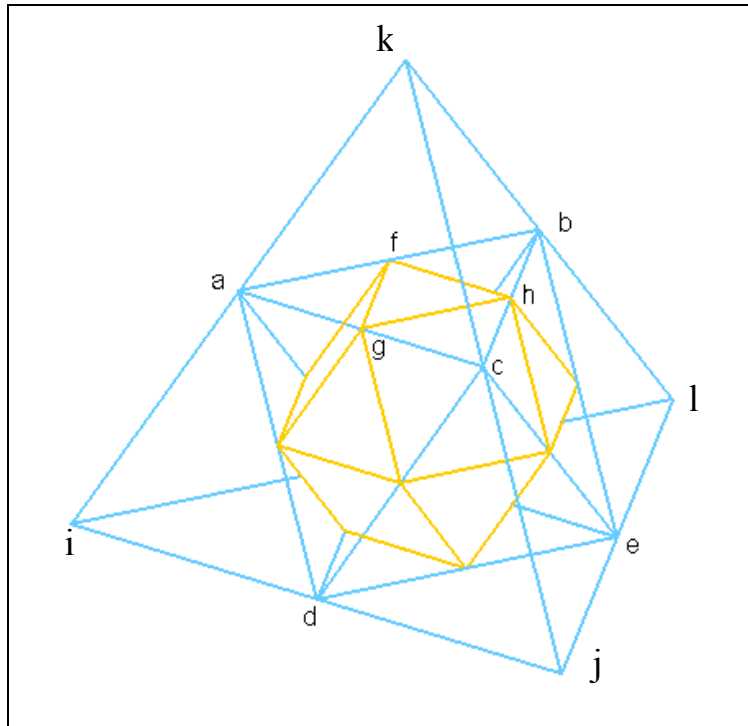


**Fig 4-7** : Polyhedron ijlk is the primitive tetrahedron which is used to cut. The yellow Polyhedron inside the primitive tetrahedron is the final bulk like QD called QDa.

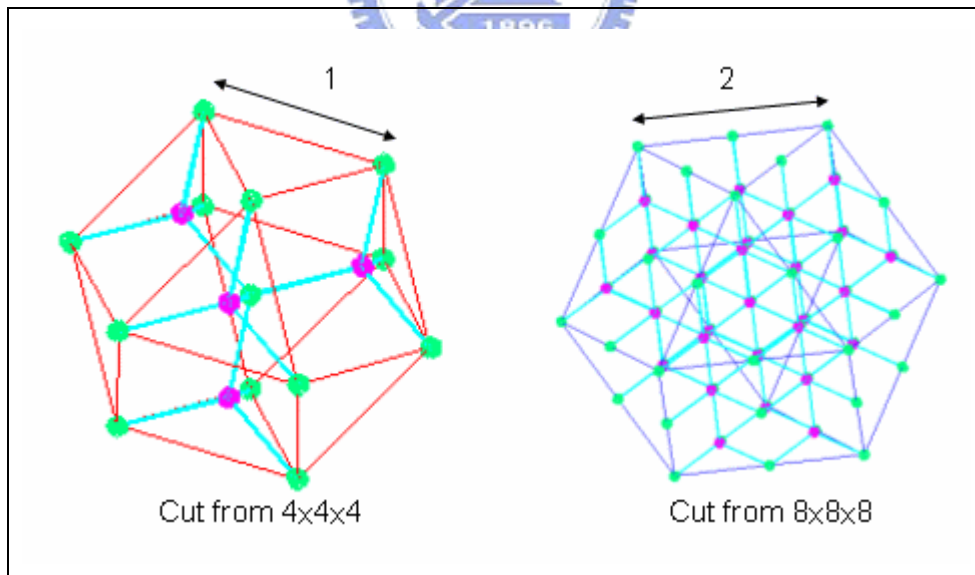


**Fig 4-8** : Left : The QDa cut from  $4 \times 4 \times 4$  unit CdSe primitive tetrahedron ; right : The QDa cut from  $8 \times 8 \times 8$  unit CdSe primitive tetrahedron

For QDb kind, it is much like the QDa kind, but after cut the tetrahedrons on four apexes of the primitive tetrahedron and form the octahedron, we pick up all the third

points on eight sidelines of the octahedron ( ex: points i,j in line ac shown in **Fig 4-9** ) and cut tetrahedrons at six apexes along the wirings of these third points to form the yellow shape in **Fig 4-9** which is a polyhedron with hexagon and square.

Because the line ac need to be dividing into three segments, the shortest length of line ac is at least three units CdSe long. And the length of line fg should be double of line ac ( being six unit CdSe long ) , so the smallest cut able primitive tetrahedron is  $6 \times 6 \times 6$  unit CdSe tetrahedron. Similarly, the next allowed lengths of line ac is 6, 9, 12, 15 and so on, all they can be divide into three segments. So the allowed cut able primitive tetrahedron is follow by  $12 \times 12 \times 12, 18 \times 18 \times 18, 24 \times 24 \times 24, 30 \times 30 \times 30$  unit CdSe.

**Fig4-10** are the QDb models cut from  $6 \times 6 \times 6$  and  $12 \times 12 \times 12$  primary tetrahedron. One can see that they have the same shape but different size.

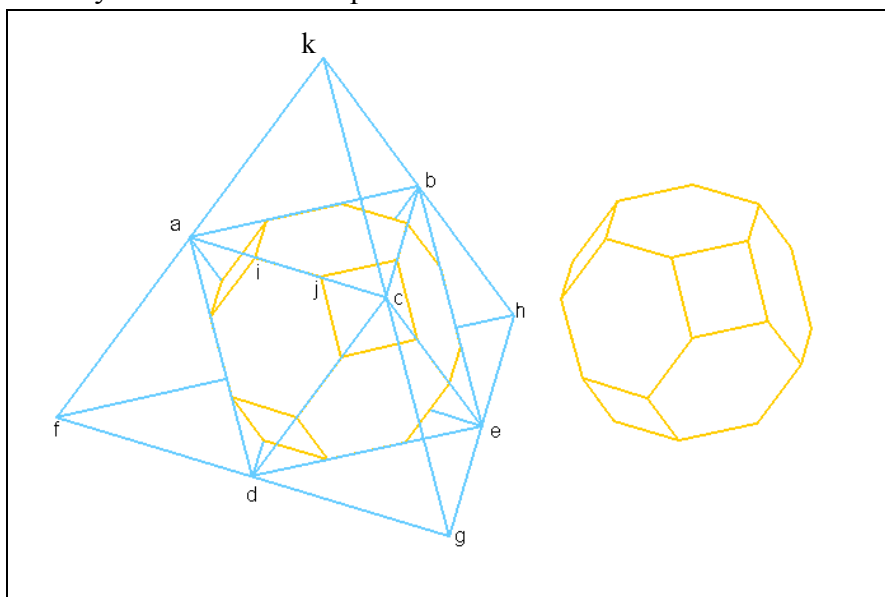


**Fig 4-9** : Left : Polyhedron fghk is the primitive tetrahedron which is used to cut. Right : The yellow color polyhedron is the final bulk like QD called QDb.



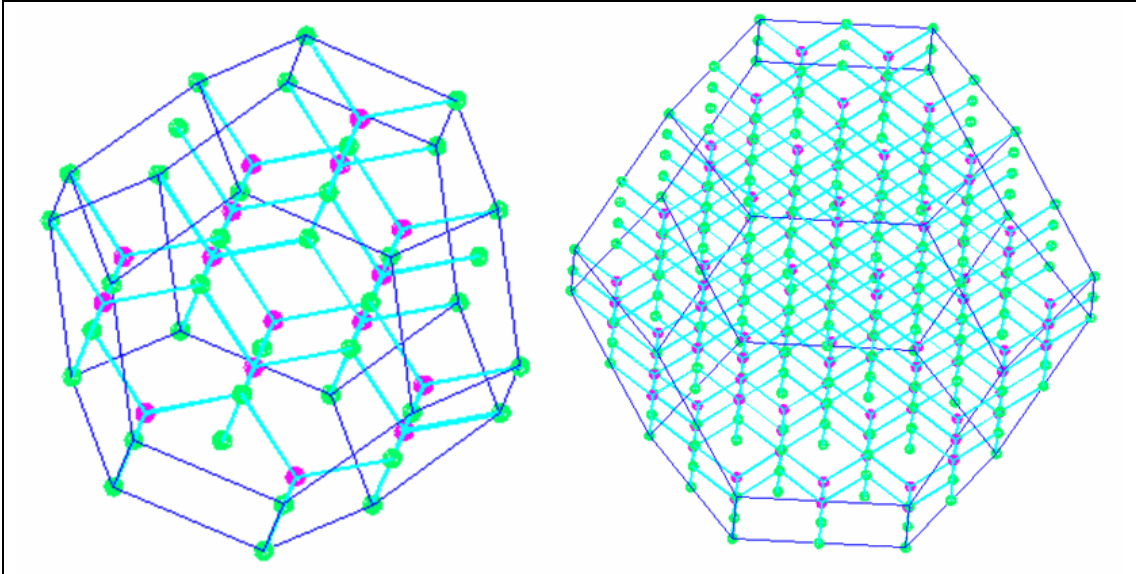


**Fig 4-10** : Left : The QDb cut from 6x6x6 unit CdSe primitive tetrahedron.  
 Right : The QDb cut from 12x12x12 unit CdSe primitive tetrahedron.

### 4-3 The introduction of first-principle calculation

#### 4-3-1 Hartree and Hartree-Fock Equations

When dealing with many-electron problem, Born and Oppenheimer ( 1927 ) suggested an approximation scheme that is employed quite universally throughout condensed matter physics. When the electrons in lattice are concerned, take the nuclei to be static, classical potentials (  $U_{ion}$  ), and solve the electronic problem without worrying about the nuclei further. Under Born-Oppenheimer approximation, the Hamiltonian of many-electrons system can be expressed :

$$\hat{H}\Psi = \frac{\hbar}{2m} \sum_{l=1}^N \nabla_l^2 \Psi + \sum_{l=1}^N U_{ion}(\vec{r}_l) \Psi + \sum_{l < l'}^N \frac{e^2}{|\vec{r}_l - \vec{r}_{l'}|} \Psi = \epsilon \Psi \dots\dots\dots(4.1)$$

Where  $\Psi$  is an antisymmetric wavefunction of the immense number  $N$  of electrons in a solid.

This equation is so hard to solved as it stand ( even  $N$  up to ten ) . In fact, all the computational difficulty arises from the coulomb interaction. Perhaps this term may some how be replaced by something more computationally tractable, such as an effective electron-electron potential  $U_{ee}(\vec{r})$  .

A first guess at such an effective potential in which to study the motion of electrons is that **each electron moves in a field produced by a sum over all the other electrons.**

That means:  $U_{ee}(\vec{r}) = \int d\vec{r}' \frac{e^2 n(\vec{r}')}{|\vec{r} - \vec{r}'|}$ , where n is the number density of electrons ,

$$n(\vec{r}) = \sum_j |\psi_j(\vec{r})|^2$$

This can let (4.1) a many-electrons equation becomes many single electron equations such as:  $\frac{-\hbar^2}{2m} \nabla^2 \psi_l + [U_{ion}(\vec{r}) + U_{ee}(\vec{r})] \psi_l = \epsilon_l \psi_l \dots \dots \dots (4.2)$

Note : l means l'th electron

Equation (4.2) is the **Hartree equation**. But the failing of the Hartree equation is that it does not recognize the Pauli principle. Because the true many-body wave function must vanish whenever two electrons occupy the same position, but the Hartree wave function cannot have this property. To solve this problem, Fock (1930) and Slater (1930) showed that the way to obey the Pauli principle is to work within the space of antisymmetric wave function . Absolutely the simplest possible type of antisymmetric wave function is obtain by taking a collection of orthonormal one-particle wave function and antisymmetrizing them :

$$\Psi(\vec{r}_1 \sigma_1 \dots \vec{r}_N \sigma_N) = \frac{1}{\sqrt{N!}} \sum_s (-1)^s \psi_{s1}(\vec{r}_1 \sigma_1) \dots \psi_{sN}(\vec{r}_N \sigma_N)$$

$$= \frac{1}{\sqrt{N!}} \begin{vmatrix} \psi_1(\vec{r}_1 \sigma_1) & \psi_1(\vec{r}_2 \sigma_2) & \dots & \psi_1(\vec{r}_N \sigma_N) \\ \vdots & \vdots & \ddots & \vdots \\ \psi_N(\vec{r}_1 \sigma_1) & \psi_N(\vec{r}_2 \sigma_2) & \dots & \psi_N(\vec{r}_N \sigma_N) \end{vmatrix} \dots \dots \dots (4.3)$$

The sum is over all permutations s of 1...N.  $\sigma_i$  is a spin index

This type of wavefunction is called a Slater determinant.

Because the wavefunction is not a simple product, but a sum of products, the particles are no longer independent. Thus the Pauli principle induces correlations among particles.

Now we can decompose wave function into two part ( As long as the Hamiltonian doesn't involve the spin explicitly. ) :

$$\psi_l(\vec{r}_i \sigma_i) = \phi_l(\vec{r}_i) \chi_l(\sigma_i)$$

The spin function  $\chi_l$  is either the "spin-up" function or the "spin-down" function.

To obtain the Hartree-Fock equations, we can use the variation principle to drive it.

( This principle is also a way to derive Hartree equation. )

There are three step :

A. Defines a function:  $F_H \{ \Psi \} \equiv \langle \Psi | H | \Psi \rangle$ , and constraint with  $\langle \Psi | \Psi \rangle = 1$

B. Take  $\Psi(\vec{r}_1 \sigma_1 \dots \vec{r}_N \sigma_N) = \frac{1}{\sqrt{N!}} \sum_s (-1)^s \psi_{s1}(\vec{r}_1 \sigma_1) \dots \psi_{sN}(\vec{r}_N \sigma_N)$  into it.

C. Do variation  $\frac{\delta F_H}{\delta \psi_l^*(\vec{r})} - \frac{\delta}{\delta \psi_l^*(\vec{r})} \sum_j \varepsilon_j \int d\vec{r}' \psi_j^*(\vec{r}') \psi_j(\vec{r}') = 0$  to get Hartree-Fock equation.

So the first step is to take the expectation value of the Hamiltonian with the wavefunction (4.3), and the next step is to require that its functional derivative with respect to each  $\psi_i$  vanish.

For expectation value of kinetic energy :

$$\begin{aligned} & \sum_{\sigma_1 \dots \sigma_N} \int d^N \vec{r} \frac{1}{N!} \sum_{ss'} (-1)^{s+s'} \left[ \prod_j \psi_{sj}^*(\vec{r}_j \sigma_j) \right] \sum_l \frac{-\hbar^2 \nabla_l^2}{2m} \left[ \prod_{j'} \psi_{s'j'}(\vec{r}_{j'} \sigma_{j'}) \right] \\ & \text{only } s=s' \text{ can survive ( orthonormal property )} \\ & = \sum_l \sum_{\sigma_l} \int d\vec{r}_l \frac{1}{N!} \sum_s \psi_{sl}^*(\vec{r}_l \sigma_l) \frac{-\hbar^2 \nabla_l^2}{2m} \psi_{sl}(\vec{r}_l \sigma_l) \\ & = \sum_{l=1}^N \int d\vec{r} \phi_l^*(\vec{r}) \left[ \frac{-\hbar^2 \nabla^2}{2m} \right] \phi_l(\vec{r}) \end{aligned} \quad (4.4)$$

Similarly, the expectation value of the potential energy yield :

$$\sum_{l=1}^N \int d\vec{r} \phi_l^*(\vec{r}) U_{ion}(\vec{r}) \phi_l(\vec{r}) \quad (4.5)$$

The next expectation value term is the electron-electron interaction term. For simply we adopt the notation  $\vec{r}_l \sigma_l$  by  $l$ . This term is :

$$\begin{aligned} & \sum_{\sigma_1 \dots \sigma_N} \int d^N \vec{r} \frac{1}{N!} \sum_{ss'} \sum_{i < j} \frac{e^2 (-1)^{s+s'}}{|\vec{r}_i - \vec{r}_j|} \left[ \prod_{l,l'} \psi_{sl}^*(l) \psi_{s'l'}(l') \right] \\ & \sum_{\sigma_1 \dots \sigma_N} \int d^N \vec{r} \frac{1}{N!} \sum_{ss'} \sum_{i < j} \frac{e^2 (-1)^{s+s'}}{|\vec{r}_i - \vec{r}_j|} \left[ \psi_{si}^*(i) \psi_{sj}^*(j) \times \psi_{s'i}(i) \psi_{s'j}(j) \times \prod_{l,l' \neq i,j} \psi_{sl}^*(l) \psi_{s'l'}(l') \right] \\ & = \dots = \int \frac{e^2 d\vec{r}_1 d\vec{r}_2}{|\vec{r}_1 - \vec{r}_2|} \sum_{i < j} \left[ |\phi_i(\vec{r}_1)|^2 |\phi_j(\vec{r}_2)|^2 - \phi_i^*(\vec{r}_1) \phi_j^*(\vec{r}_2) \phi_i(\vec{r}_2) \phi_j(\vec{r}_1) \delta_{x_i x_j} \right] \quad (4.6) \end{aligned}$$

The first term in (4.6) is called ‘‘Coulomb integral’’. The second term is more

noteworthy ; it is called the exchange integral and may be interpreted as saying that particle 1 and 2 flip places in the course of interaction.

So by collecting (4.4) (4.5) (4.6) , the total Hamiltonian expectation value is

$$\langle \Psi | H | \Psi \rangle = \sum_i \sum_{\sigma_1} \int d\vec{r}_1 \psi_i^*(1) \frac{-\hbar^2 \nabla}{2m} \psi_i(1) + U(\vec{r}_1) |\psi_i(1)|^2 + \int d\vec{r}_1 d\vec{r}_2 \frac{e^2}{|\vec{r}_1 - \vec{r}_2|} \sum_{\substack{i < j \\ \sigma_1 \sigma_2}} \left[ |\psi_i(1)|^2 |\psi_j(2)|^2 - \psi_i^*(1) \psi_j^*(2) \psi_i(2) \psi_j(1) \right] \dots \dots \dots (4.7)$$

Having found the expectation value, the next task is to vary the functional (4.7) with respect to every single-particle function  $\psi$  and require each variation to vanish subject to the condition that  $\psi$ 's be orthonormal.

The variation result is

$$\sum_j \varepsilon_{ij} \psi_j(1) = \frac{-\hbar^2 \nabla^2}{2m} \psi_i(1) + U(\vec{r}_1) \psi_i(1) + \psi_i(1) \int d\vec{r}_2 \sum_{\sigma_2, j=1} \frac{e^2 |\psi_j(2)|^2}{|\vec{r}_1 - \vec{r}_2|} - \sum_{j=1}^N \psi_j(1) \sum_{\sigma_2} \int d\vec{r}_2 \frac{e^2 \psi_j^*(2) \psi_i(2)}{|\vec{r}_1 - \vec{r}_2|} \dots \dots \dots (4.8)$$

This is the Hartree-Fock equation.

If one define a new wavefunction  $\tilde{\psi}_i = \sum_j W_{ij} \psi_j$ . Matrix W is a unitary matrix, and

we go through the same variation procedure above. There exists a basis which  $\varepsilon_{ij}$  is

diagonal. Thus the Hartree-Fock equation (4.8) can be expressed as (carrying out the spin sum in (4.8))

$$\varepsilon_i \phi_i(\vec{r}) = -\frac{\hbar^2 \nabla^2}{2m} \phi_i(\vec{r}) + U(\vec{r}) \phi_i(\vec{r}) + \phi_i(\vec{r}) \int d\vec{r}' \sum_{j=1}^N \frac{e^2 |\phi_j(\vec{r}')|^2}{|\vec{r} - \vec{r}'|} - \sum_{j=1}^N \delta_{\lambda_i \lambda_j} \phi_j(\vec{r}) \int d\vec{r}' \frac{e^2 \phi_j^*(\vec{r}') \phi_i(\vec{r}')}{\|\vec{r} - \vec{r}'\|}$$

This is the final form of Hartree-Fock equation

### 4-3-2 Density Functional Theory

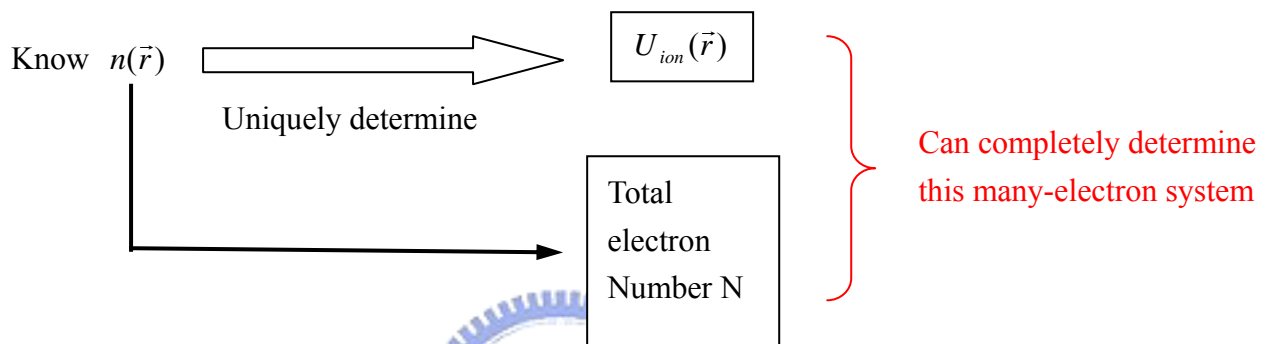
The starting point of the theory is the observation of Hohenberg and Kohn (1964) that electron density contains in principle all the information contained in many-electron wavefunction. The electronic density of a many-electron system at point  $\vec{r}$  is defined to be :

$$n(\vec{r}) = \langle \Psi | \sum_{l=1}^N \delta(\vec{r} - \vec{R}_l) | \Psi \rangle$$

Sum the contribution of every electron's density at point  $\vec{r}$ . ( $\vec{R}_l$  is the coordinate of  $l^{th}$  electron)

Hohenberg and Kohn point out that if one knows the density of the ground state of a many-electron system, one can deduce from it the external potential in which the electrons reside, up to an overall constant. How can you distinguish two different many-electron systems? After your deep thought you may find that the only ways they can differ are in the external potentials  $U_{ion}$  and in the number of electrons that reside in the potentials. According to this point, both of these external parameters are determined by the electron density. Thus one can say that the density completely determines the many body problems.

The concept of it :



To prove the claim, suppose that it is false, suppose that there exist two external potentials  $U_1(\vec{r})$  and  $U_2(\vec{r})$  that result in the same charge density.

Let  $\hat{H}_1 = T + U_{ee} + U_1$   $\longrightarrow$  Its ground state wavefunction is  $\Psi_1$

$\hat{H}_2 = T + U_{ee} + U_2$   $\longrightarrow$  Its ground state wavefunction is  $\Psi_2$

Then the ground state energy of  $\hat{H}_1$  is realized only by  $\Psi_1$ .

$$\text{So } \varepsilon_1 = \langle \Psi_1 | \hat{H}_1 | \Psi_1 \rangle < \langle \Psi_2 | \hat{H}_1 | \Psi_2 \rangle$$

$$\Rightarrow \varepsilon_1 < \langle \Psi_2 | \hat{H}_2 | \Psi_2 \rangle + \langle \Psi_2 | (\hat{H}_1 - \hat{H}_2) | \Psi_2 \rangle$$

$$\Rightarrow \varepsilon_1 < \varepsilon_2 + \int d\vec{r} n(\vec{r}) [U_1(\vec{r}) - U_2(\vec{r})]$$

However, you can switch indices 1 and 2 to obtain  $\varepsilon_2 < \varepsilon_1 + \int d\vec{r} n(\vec{r}) [U_2(\vec{r}) - U_1(\vec{r})]$

That gives  $\varepsilon_1 + \varepsilon_2 < \varepsilon_1 + \varepsilon_2$ , which is contradiction. Therefore the potential  $U_1$  and  $U_2$

must be the same. That proved the claim that  $n(\vec{r})$  uniquely determine the  $U_{ion}(\vec{r})$ .

In principle, one can write down this functional form to indicate the above fact :

$$\varepsilon[n] = T[n] + U[n] + U_{ee}[n] \dots\dots\dots (4.9)$$

Here  $n$  means  $n(\vec{r})$ ,  $T$  is the kinetic energy.  $U$  is the potential due to ions, and  $U_{ee}$  is the interaction between electrons.

**So if one can know the functional form  $\varepsilon[n]$ , then one can iterate  $n(\vec{r})$  routinely to minimize it** (to find the really ground state density  $n_1(\vec{r})$ ), subject only to the constraint  $\int d\vec{r}n(\vec{r}) = N$ .

By writing  $U[n] = \int d\vec{r}n(\vec{r})U(\vec{r})$  (functional form of  $U[n]$ ), one can write (4.9)

$$\text{as } \varepsilon[n] = \int d\vec{r}n(\vec{r})U(\vec{r}) + F_{HK}[n] \quad \text{where } F_{HK}[n] = T[n] + U_{ee}[n].$$

The functional  $F_{HK}[n]$  does not depend upon the potential  $U(\vec{r})$ , thus it constitutes a universal functional for all systems of  $N$  particles : **If one can know it's form, one can solve all many body problems for all external potential  $U$ .**

No one knows the true  $F_{HK}[n]$ , and no one ever will, so it is replaced by various uncontrolled approximations, ex: Thomas-Fermi theory and Kohn-Shan theory.

### 4-3-3 Kohn-Shan theory and Local Density Approximation

#### (LDA)

Kohn and Shan retreated slightly from the hope of writing all material properties as function of electron density, and proposed using instead a set of  $N$  single-electron wave function  $\psi_l(\vec{r})$  as the main ingredients, obtaining the density from them by

$$n(\vec{r}) = \sum_{l=1}^N |\psi_l(\vec{r})|^2 \quad \text{which means the electron density is contributed by sum of every}$$

wavefunction square at the local position  $\vec{r}$ , and this is the main spirit of local density approximation(LDA).

In this case, the kinetic energy term of the energy functional is

$$T[n] = \sum_l \frac{\hbar^2}{2m} (\nabla \psi_l)^2$$

Apart from the kinetic energy, the energy functional is just what it was for

Thomas-Fermi-Dirac theory : exchange and correlation energies are calculated by using results from the homogeneous electron gas. Varying the density functional form in Thomas-Fermi theory with respect to  $\psi_i^*$  gives

$$-\frac{\hbar^2}{2m}\nabla^2\psi_i(\vec{r}) + \left[ U(\vec{r}) + \int d\vec{r}' \frac{e^2 n(\vec{r}')}{|\vec{r} - \vec{r}'|} + \frac{\partial \varepsilon_{xc}(n)}{\partial n} \right] \psi_i(\vec{r}) = \varepsilon_i \psi_i(\vec{r}) \dots \dots \dots (4.10)$$

The function  $\varepsilon_{xc}(n)$  is the exchange-correlation energy of the uniform electron gas, and this equation is known as the **Kohn-Sham equation**.

The class of approximations of the form (4.10) is referred to as the local density approximation (LDA).

## 4-4 Relation between Eg and photon lifetime

It is well known that an atom in an excited state is not in a stationary state — it will eventually decay to the ground state by spontaneously emitting a photon. The nature of this evolution is due to the coupling of the atom to the electromagnetic vacuum field. The idea of spontaneous emission goes back to Einstein when he studied Planck's blackbody spectrum using the principle of detailed balance. The rate of spontaneous emission is still known as the "Einstein A coefficient". Victor Weisskopf presented a method for analyzing this interesting problem in his thesis work, together with his advisor Eugene Wigner. We will follow their treatment here.

Consider a two-level atom. Initially the atom is prepared in its excited state  $|e\rangle$  and the field is in vacuum state  $|\{0\}\rangle$ . We use

$$|\psi(0)\rangle = |e, \{0\}\rangle$$

to denote this initial state. Since this is not a stable state, the atom will decay to the ground state  $|g\rangle$  and give  $(k, s)$  photon in mode  $(k; s)$ . The state of the system after the decay is then  $|g, 1_{ks}\rangle$ . These state vectors form a complete set for expanding the time-dependent state of the system:

$$|\psi(t)\rangle = a(t)e^{-i\omega_0 t} |e, \{0\}\rangle + \sum_{k,s} b_{ks}(t)e^{-i\omega_k t} |g, 1_{ks}\rangle$$

Where  $\omega_0$  is the atomic transition frequency and  $\omega_k = ck$  is the frequency of the photon.



The total Hamiltonian under the rotating wave approximation is  $H = H_A + H_F + H_{\text{int}}$  with

$$H_A = \hbar\omega_0 \hat{\sigma}_{ee}$$

$$H_F = \sum_{k,s} \hbar\omega_k \hat{n}_{ks}$$

$$H_{\text{int}} = -\hat{d} \cdot \hat{E} = -\sum_{k,s} \hbar g_{ks} \hat{\sigma}_{eg} \hat{a}_{ks} + h.c$$

where the atom-field coupling coefficient is

$$g_{ks} = i \sqrt{\frac{\omega_k}{2\hbar\epsilon_0 V}} (d \cdot \epsilon_{ks})$$

The Schrodinger equation reads

$$H|\psi(t)\rangle = i\hbar \frac{\partial}{\partial t} |\psi(t)\rangle = i\hbar(\dot{a} - i\omega_0 a) e^{-i\omega_0 t} |e, \{0\}\rangle + i\hbar \sum_{k,s} (\dot{b}_{ks} - i\omega_k b_{ks}) e^{-i\omega_k t} |g, 1_{ks}\rangle$$

By multiply through this equation by  $\langle e, \{0\} |$  and  $\langle g, 1_{ks} |$ , respectively, we obtain

$$\dot{a}(t) = i \sum_{k,s} g_{ks} e^{-i(\omega_k - \omega_0)t} b_{ks}(t) \dots\dots\dots (4.11)$$

$$\dot{b}_{ks}(t) = i g_{ks}^* e^{i(\omega_k - \omega_0)t} a(t) \dots\dots\dots (4.12)$$

To solve these equations, we first formally integrate (14.12) as

$$b_{ks}(t) = i g_{ks}^* \int_0^t dt' e^{i(\omega_k - \omega_0)t'} a(t')$$

and put this back into (14.11), we have

$$\dot{a}(t) = -\sum_{k,s} |g_{ks}|^2 \int_0^t dt' e^{-i(\omega_k - \omega_0)(t-t')} a(t') \dots\dots\dots (4.13)$$

First let us concentrate on  $\sum_{k,s} |g_{ks}|^2$ . In the continuum limit (i.e., when the quantization volume  $V \rightarrow \infty$ ), we have

$$\sum_{k,s} \longrightarrow \sum_{s=1}^2 \int d^3k D(k)$$

where  $D(k)$  is the density of states in k-space. Since  $k = (2\pi n_1/L; 2\pi n_2/L; 2\pi n_3/L)$ , there is one state in volume  $(2\pi/L)^3 = (2\pi)^3/V$ , hence the density of states is  $D(k) = V/(2\pi)^3$ . Then using the spherical coordinates  $(k, \theta, \phi)$ , we have

$$\sum_{k,s} \rightarrow \sum_{s=1}^2 \frac{V}{(2\pi)^3} \int_0^\infty k^2 dk \int_0^\pi \sin \theta d\theta \int_0^{2\pi} d\phi$$

Thus

$$\sum_{k,s} |g_{ks}|^2 = \sum_{k,s} \frac{w_k}{2\varepsilon_0 V \hbar} (d \cdot \varepsilon_{ks})^2 = \int_0^\infty dk k^2 \frac{w_k}{2(2\pi)^3 \varepsilon_0 \hbar} \left[ \sum_{s=1}^2 \int_0^\pi \sin \theta d\theta \int_0^{2\pi} d\phi (d \cdot \varepsilon_{ks})^2 \right]$$

Here we assume that  $d$  is real, but the final result is more general and works also for complex  $d$ . First let us evaluate the quantity inside the square bracket using a simple trick:

$$\sum_{s=1}^2 \int_0^\pi \sin \theta d\theta \int_0^{2\pi} d\phi (d \cdot \varepsilon_{ks})^2 = \int_0^\pi \sin \theta d\theta \int_0^{2\pi} d\phi [(d \cdot \varepsilon_{k1})^2 + (d \cdot \varepsilon_{k2})^2] \dots \dots \dots (4.14)$$

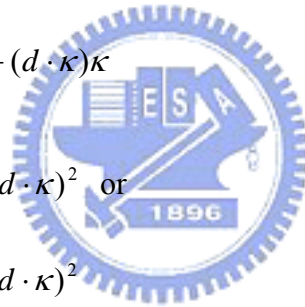
Since the triplet  $(\varepsilon_{k1}, \varepsilon_{k2}, \kappa)$  with  $\kappa = k/|k|$  forms an orthogonal set of unit vectors that we can use to expand any vector, so in particular

$$d = (d \cdot \varepsilon_{k1})\varepsilon_{k1} + (d \cdot \varepsilon_{k2})\varepsilon_{k2} + (d \cdot \kappa)\kappa$$

and thus

$$|d|^2 = (d \cdot \varepsilon_{k1})^2 + (d \cdot \varepsilon_{k2})^2 + (d \cdot \kappa)^2 \text{ or}$$

$$(d \cdot \varepsilon_{k1})^2 + (d \cdot \varepsilon_{k2})^2 = |d|^2 - (d \cdot \kappa)^2$$



We can choose the spherical axis in our integral in any direction that we like, so that we may as well choose it to lie along the direction parallel to  $d$ . So we have finally

$$(d \cdot \varepsilon_{k1})^2 + (d \cdot \varepsilon_{k2})^2 = |d|^2 (1 - \cos \theta)^2 = |d|^2 \sin^2 \theta$$

Now Eq. (4.14) can be easily evaluated to give

$$\sum_{s=1}^2 \int_0^\pi \sin \theta d\theta \int_0^{2\pi} d\phi (d \cdot \varepsilon_{ks})^2 = \frac{8\pi}{3} |d|^2$$

Therefore

$$\sum_{k,s} |g_{ks}|^2 = \int_0^\infty dk k^2 \frac{w_k}{2(2\pi)^3 \varepsilon_0 \hbar} \frac{8\pi}{3} |d|^2 = \frac{|d|^2}{6\pi^2 \varepsilon_0 \hbar c^3} \int_0^\infty w_k^3 dw_k$$

where we have changed the integration over  $k$  to over  $w_k = ck$ .

Next let us take a look at the time integral in (4.13):

$$\int_0^t dt' e^{-i(w_k - w_0)(t-t')} a(t')$$

The exponential oscillates with frequency  $\sim w_0$ . We assume that the excited state amplitude  $a(t)$  varies with a rate  $\Gamma \ll w_0$ . Therefore  $a(t)$  changes little in the time interval over which the remaining part of the integrand has non-zero value ( $t' \sim t$ ), and we can replace  $a(t')$  in the integrand by  $a(t)$  and take it out of the integral.

This is called the Weisskopf-Wigner approximation, which can be recognized as a Markov approximation: Dynamics of  $a(t)$  depends only on time  $t$  and not on  $t' < t$ , i.e., the system has no memory of the past.

Now the time integral becomes

$$\int_0^t dt' e^{-i(w_k - w_0)(t-t')} a(t') \approx a(t) \int_0^t d\tau e^{-i(w_k - w_0)\tau}$$

with  $\tau = t - t'$ . Since  $a(t)$  varies with a rate  $\Gamma \ll w_0$ , the time of interest  $t \gg 1/w_0$ , thus we can take the upper limit of the above integral to  $\infty$ , and we have

$$\int_0^{\infty} d\tau e^{-i(w_k - w_0)\tau} = \pi \delta(w_k - w_0) - iP \left( \frac{1}{w_k - w_0} \right)$$

where  $P$  represents the Cauchy principal part.

Because of the  $i$  before the second term, the Cauchy principal part leads to a frequency shift. This is in fact one contribution to the Lamb's shift. This shift diverges and has been dealt with through renormalization. Here we will neglect this part. Put things together into (4.13), we finally have

$$\dot{a}(t) = -\frac{\Gamma}{2} a(t)$$

where

$$\Gamma = \frac{w_0^3 |d|^2}{3\pi \epsilon_0 \hbar c^3}$$

The excited state amplitude thus decays exponentially as

$$a(t) = e^{-\Gamma t/2} a(0)$$

$\Gamma$  is then the population decay rate, also known as the **Einstein A coefficient**.

## Chapter5 : Conclusion

In this chapter we summarize all the work and discussion mentioned in this article and

get the following conclusion :

1. From Raman and PL spectrum we find QD also has the pressure induced phase transition. QD differs from bulk in the phase transition pressure, QD is at 7GPA while bulk CdSe is at 3GPA, and this may be due to the ZnS shell's protection of QDs. The luminescence of QD is no longer found after phase transition, thus we guess the core's structure of QD has become metal phase after phase transition. Because in the previous study, we know the band diagram of CdSe with rocksalt structure shows overlap of the conduction band and valence band ; ie. Metal phase of bulk CdSe. We also believe that CdSe QD is this structure after phase transition.
2. From Raman spectrum, after phase transition we find an undetermined mode appears in  $156\text{ cm}^{-1}$  with no pressure dependence. After phase transition the reducing pressure experiment shows when pressure comes back to less than 7GPA, CdSe LO mode appears again but 2LO mode never comes back and the undetermined mode at  $156\text{ cm}^{-1}$  still presents. For this result we guess core CdSe don't resume to the origin phase, in another word the phase transition is irreversible.
3. In the loading and unloading of pressure shows ZnS LO peaks are almost the same, thus we suggested ZnS appears no phase transition. and is only compressed/relaxed while adding/reducing pressure.
4. The Grüneisen parameter of CdSe LO and 2LO modes show that QDs are more and more covalent while pressure is increased. Our PL spectrum also shows that band edge shift with pressure becomes nonsensitive at high pressure. We think the phenomenon is due to the lattice covalency while loading pressure, thus the polaron is not easy to form or in another word, it will reduce the electron-phonon interaction energy. For this reason the polaron energy will decrease while pressure is higher, and this causes the pressure dependence of band edge in QD becomes smooth at high pressure.
5. In the time resolved spectrum we find the radiative decay becomes faster while pressure is increased. From quantum optic theorem prediction, radiative decay rate is proportion to the cubic power of the radiation energy. But our time resolved spectrum shows a nonconstant slope of  $\Gamma - E_g^3$  diagram, on the contrary the slope tend to be sharper while loading pressure. We doubt that it comes from the electronic structure difference induced electron effective mass change ( bigger ) in QDs while loading pressure. Predicted by formula ( 3.B ), one can see the slope of  $\Gamma - E_g^3$  diagram indeed becomes larger while pressure is increased, and the slope of the wide band QD is larger than the narrow band QD.
6. By following the report about first-principle calculation on silicon QD, we

employed the geometric method of constructing QD and developed a new method of constructing CdSe QD. We can construct QD by cutting zinc-blende structure and let QD to form a fixed shape but size from small to big ; these QDs are named by QDa and QDb. We also find out some constraints in constructing CdSe QD model, ie : it may only exist the bulk like QD in CdSe.

For future work : I hope by the raising of the ab-initio method, it is able to give an accurate knowledge of the dependence of electron behavior in QD on pressure. Thus pressure induced structure difference in bulk approximation of this article can be solved successfully.

I calculated the band edge and density of state changed with pressure in bulk CdSe. However, the calculation in QD needs a large order of computation volume due to the destruction of lattice periodicity. For this reason I regard this job as an extended work. Hope in the recent future, I can finish the calculation of suitable size QDs to compare our experiment data.

## **Appendix A : The preparation of non-colloid sample**

Take  $\text{Al}_{1-x}\text{In}_x\text{P}$  for example; which had been studied earlier in our lab, is grown on GaAs substrate, it is necessary to remove the epilayer away from the GaAs substrate so that when we take the spectra of the epilayer, we can avoid the signals of GaAs. It is also easier to analyze the phonon peaks of the samples. The procedures are as follow:

1. Use the heat wax to stick the sample face down on the glass, then stick the sample and glass polishing base.
2. Use the  $\text{Al}_2\text{O}_3$  powder ( $10 \mu\text{m}$  combined with  $1 \mu\text{m}$ ) to remove the substrate as mush as we can, but avoid the sample being broken.
3. Use the solution  $\text{H}_2\text{O}_2$ :  $\text{NaOH}$ :  $\text{H}_2\text{O}$  = 6 (g): 30 (g): 30 (g) to remove the rest of the substrate until the epilayer appears.
4. We can use the acetone to solute the heat wax and left the epilayer

## **Appendix B : Alignment of Raman Scattering System**

Here we talk about how to align our Raman Scattering system.

The procedure of alignment is followed by :

### **1. Laser adjustment**

**Four procedures:**

- a. Adjust mirror M1 to get the laser beam centered into the lenses.
- b. Closed the iris.
- c. Adjust mirror M2 if necessary to get the beam centered onto the iris.
- d. Open the iris.

**2. Final adjustment of the laser**

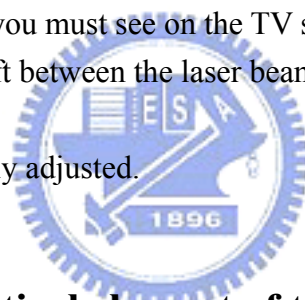
Focus the microscope onto the silicon sample delivered with the instrument by using the 100X objective. If you see a default in the focusing of the laser beam onto TV screen, adjust carefully the mirror M2 to obtain a symmetric focusing and defocusing for spot.

**3. Coupling between the confocal hole and laser beam**

To do the coupling between the hole and laser beam, you must respect the following points.

- a. Focus the microscope onto the silicon sample delivered with the instrument by using the 100X objective.
- b. Put a density filter (OD4 for example) onto laser beam.
- c. Send white lamp into the raman optical fiber and close the confocal hole to 100 microns. In these conditions, you must see on the TV screen the laser beam and the confocal hole. If there is a shift between the laser beam and the hole adjust the mirror M3 to do the coincidence.

Now the instrument is correctly adjusted.




**Appendix C : The optical element of time resolved system**

**Main Optical Unit**

All optics is used to achieve confocal excitation, detection and beam/focus diagnostics are installed together with the detectors in the self-contained main optical unit. The coupling to the inverted microscope body is achieved through the infinity beam port of the 1X 71 microscope body. This design allows easily coupling with external lasers and placing various optical elements from beam diagnostics to power monitoring in the main optical unit. Capability of various optical units is as follow.

1 : **Filter 1** is a filter just for laser coming, and strains all other light. **Filter 2** is for signal ( fluorescence from sample ) coming, and is mainly filter the laser accompany.

2 : Mirrors like  are all beam splitters or reflection mirrors which are use to control the light path to conform to our requirement.

3 : **Shutter 1** and **shutter 2**, the former stop laser coming to excite our sample, the latter stop signal light from sample come into detector 1 ( Time-Correlated Single

Photon Counting) . When measuring fluorescence, we let laser come from fiber 1 and excited signal left through port 2, so we open shutter 1 and closed shutter 2. While measuring lifetime we open both shutter 1 and shutter 2.

4 : Lens 1 and lens 2 are control the signal light pass through the confocal pinhole to make sure the excited signal is coming from a focal point of excitation source.

### **Sample Holder**

The Micro-Time 200 standard sample holder is designed to accommodate 20×20 mm<sup>2</sup> microscope cover slips. The sample holder will be mounted either directly on the microscope stage or inside the central hole of the optional piezo scanning table.

### **Detector**

The collimated beam from the basic confocal unit passes through the beam splitters and reaches the detector(s). Up to two of them can be mounted into the main optical unit. Each detector channel has its own dedicated filter holder and mechanical shutter. Currently, two types of single photon sensitive detectors are available : Single Photon Avalanche Diodes(SPAD) and Photomultiplier Tubes(PMT). SPAD detectors will be supplied with a sophisticated power supply DSN 100 with built-in protection circuits. By the way, the photodiode in the figure is a sensitive detector that counts incoming laser intensity; it can tell you much information such as : the excitation source intensity fluctuation, then you will know if the laser is in stable.

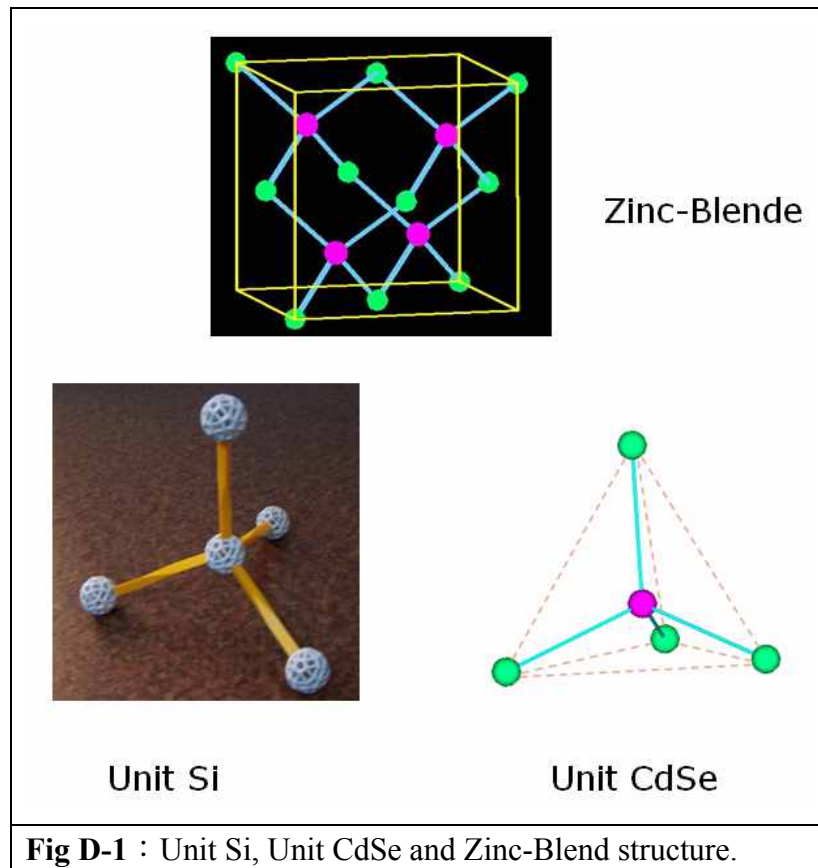
### **TCSPCD Data Acquisition**

For data acquisition the outstanding Time-Correlated Single Photon Counting board Time-Harp 200 is utilized. This highly integrated PCI-plug-in-board provides several measurements modes. One especially powerful mode is of pivotal importance for the design of the Micro Time system : in Time-Tagged Time-Resolved ( TTTR ) measurement mode each photon is recorded individually. The data stream is recorded continuously through fast Direct Memory Access ( DMA ) . Each photon record contains a picosecond timing of the photon relative to the laser pulse and coarser nanosecond timing with respect to the start of the experiment. This combination provides the performance of vastly different measurement tasks based on one fundamental data format, without any sacrifice of information available from every detected photon. It also allows all measurement data to be handled in a standardized and yet very flexible way.



## Appendix D : Construction of the QD model with Zinc-Blend

### structure



Here we want to construct the QD model of CdSe structure (or zinc-blende structure). Because CdSe is zinc-blende structure while silicon is diamond structure, basically they come from the same unit. ( See **Fig D-1** ) Can we construct QD model of CdSe by the same way of constructing silicon QD model? **Unfortunately, the answer is NO!**

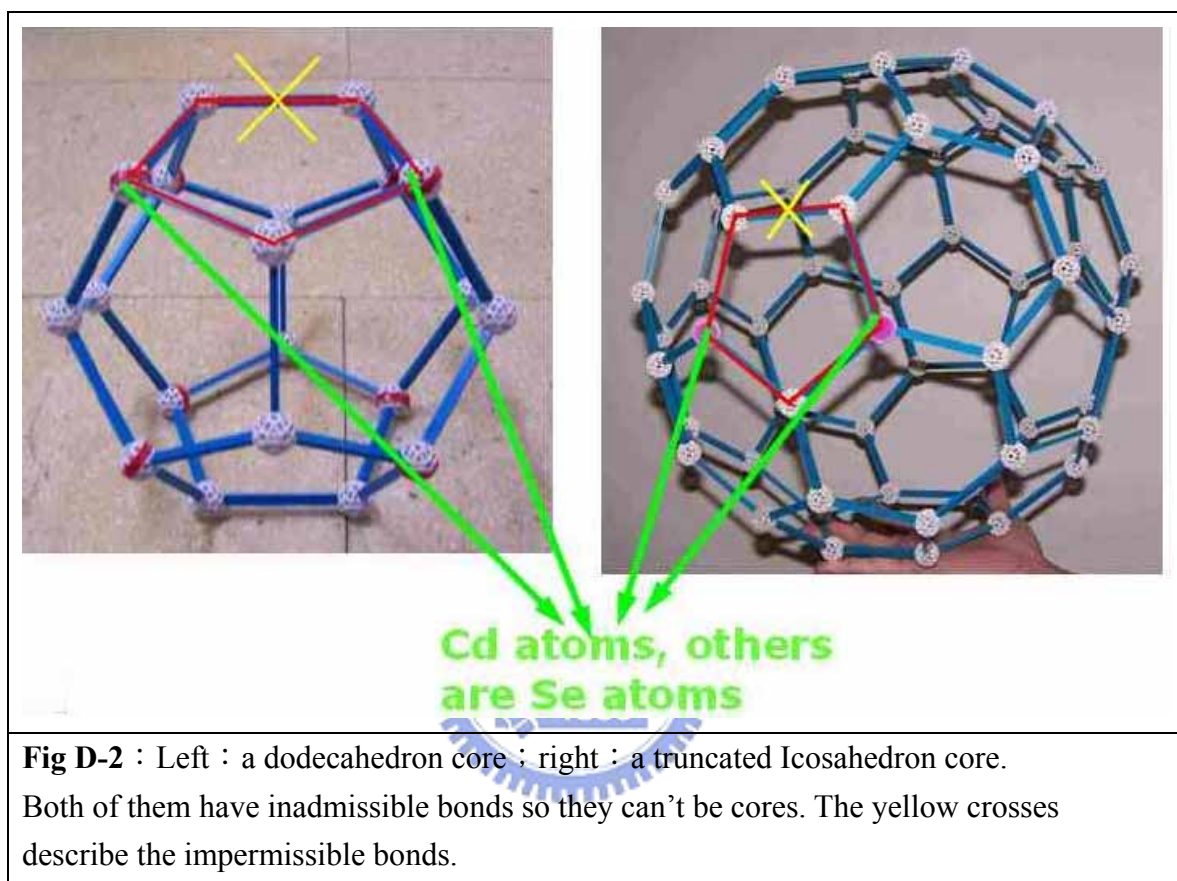
The reason is shown in Fig D-2; you can see both of the dodecahedron and truncated Icosahedrons have outward appearance of pentagons. But the atoms of CdSe structure should obey a bonding rule: **a Cd atom should bond to four Se atoms, and a Se atom should bond to four Cd atoms ; this means when you pick two adjacent atoms randomly in CdSe lattice, it must be requested that one atom is Cd atom and the other is Se atom.**

For this reason, any structure with pentagon outward appearance is not allowed being



a core. Because atoms in a pentagon should be at least two Cd atoms and that request two atoms adjacent to Cd atoms to be Se atoms, however these two Se atoms would bond to each other. In **Fig D-2** you can see two Se atoms bond together, and that is inadmissible. ( the yellow cross describe the impermissibility of this bond )

That is the reason why we can't imitate silicon to construct QD model of CdSe.



What should we do? Fortunately, there are one way to construct QD model for both silicon and CdSe structures. This model is so called “**Bulk like QD**”. Here we will briefly explain how to segment bulk to form the bulk like QD. The method of constructing this bulk like QD is described as below :

1. We piled unit CdSe until 7 layers to form a giant tetrahedron.(see **FigD-3**)
2. We cut four units on the apexes of tetrahedron and cut units along six sidelines. (**FigD-4a**)
3. Finally we cut units on four apexes again ( see **FigD-4b** ) , after that it formed the final structure.←**The Bulk like QD.** ( see **FigD-5** )

NOTE : If we use a sphere instead of a unit CdSe which with tetrahedron thus the picture is more explicit shown in **FigD-6**.

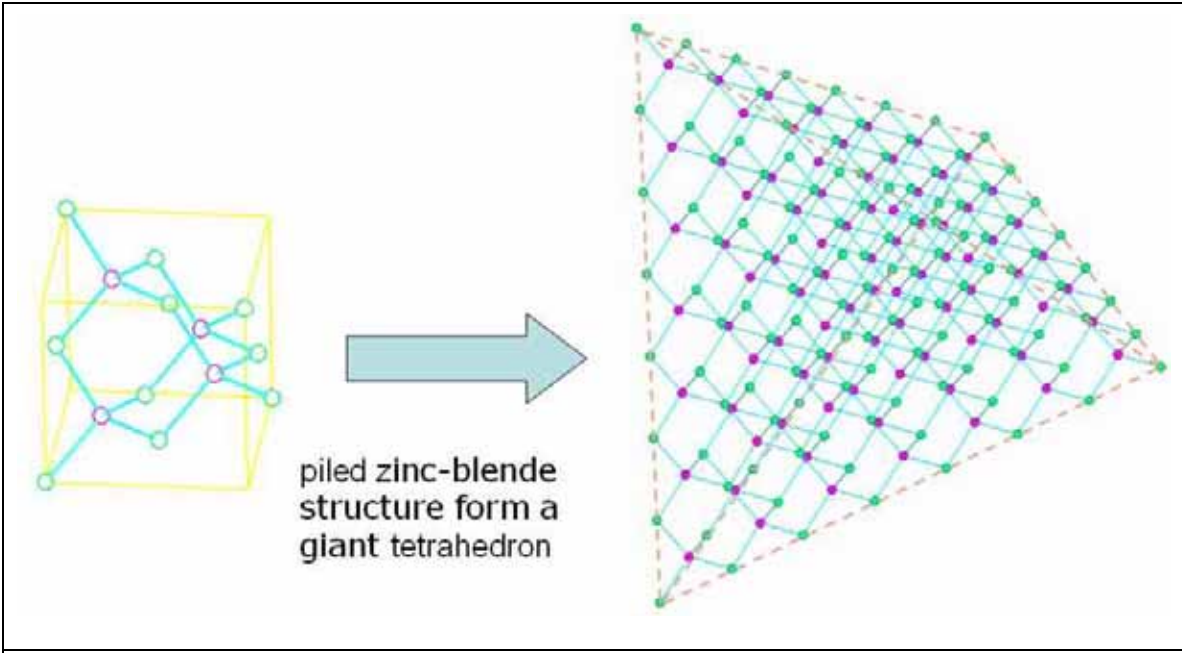


**Fig D-3** : Piling zinc-blende structure to form a 7 layers giant tetrahedron.

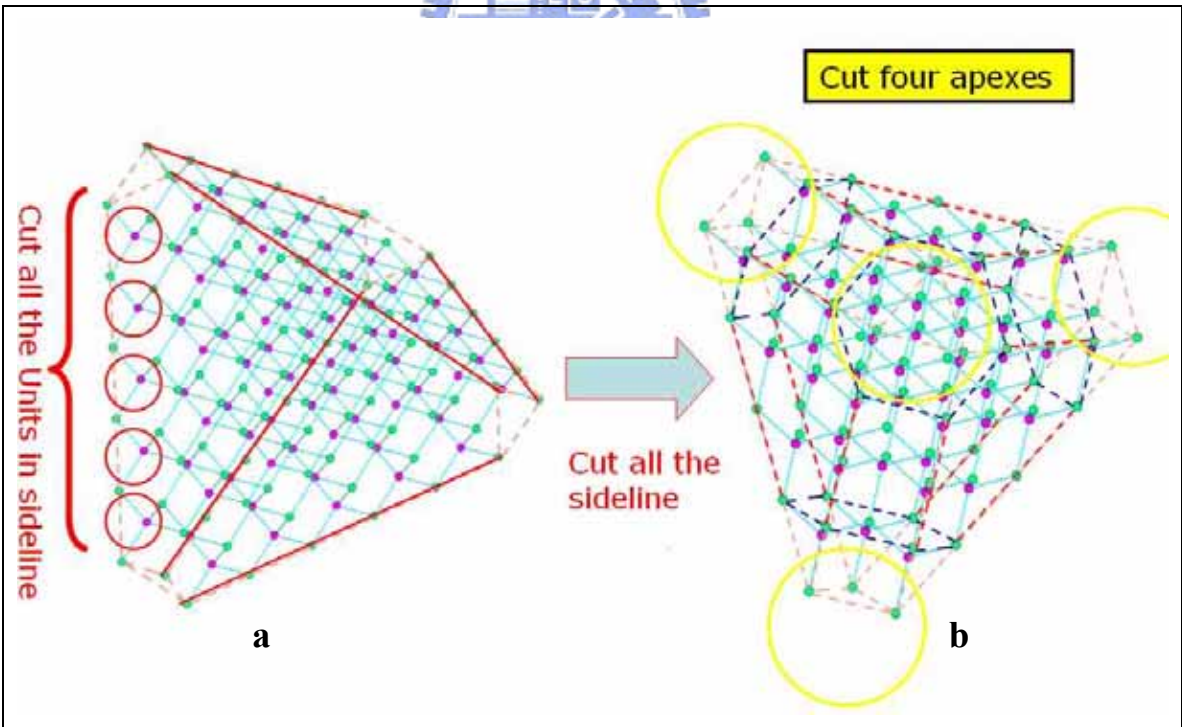


**Fig D-4** : Left: After cutting four units in apexes, we cut all units in the six sidelines. Right: We cut units in four apexes again. ( each apex has three units )

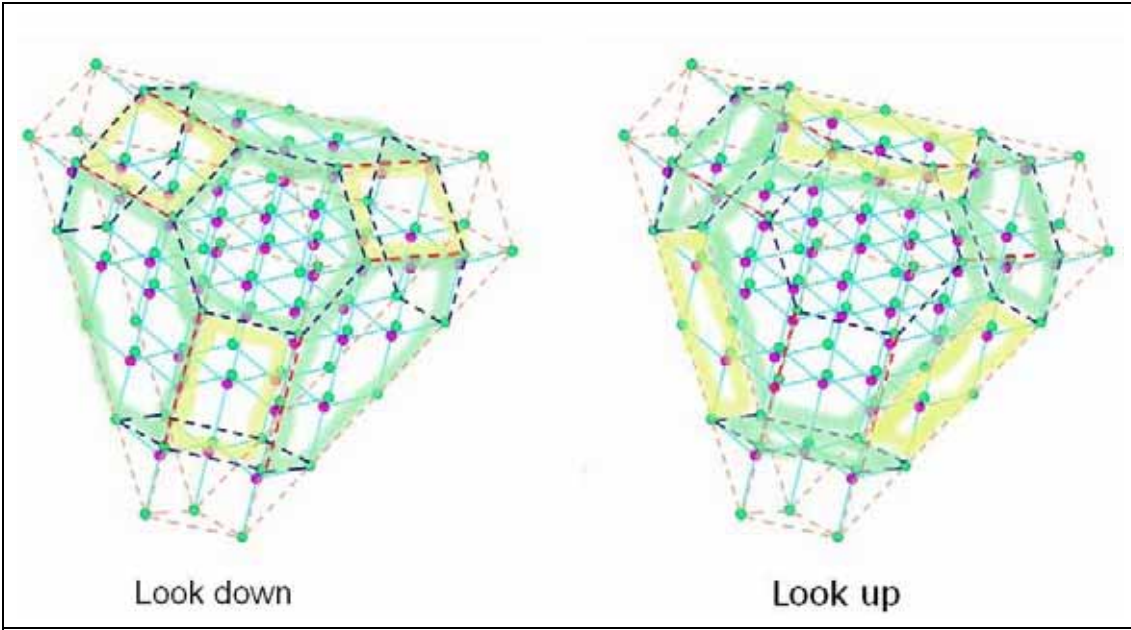


**Fig D-5** : The final bulk like structure. ( left: look down ; right : look up )

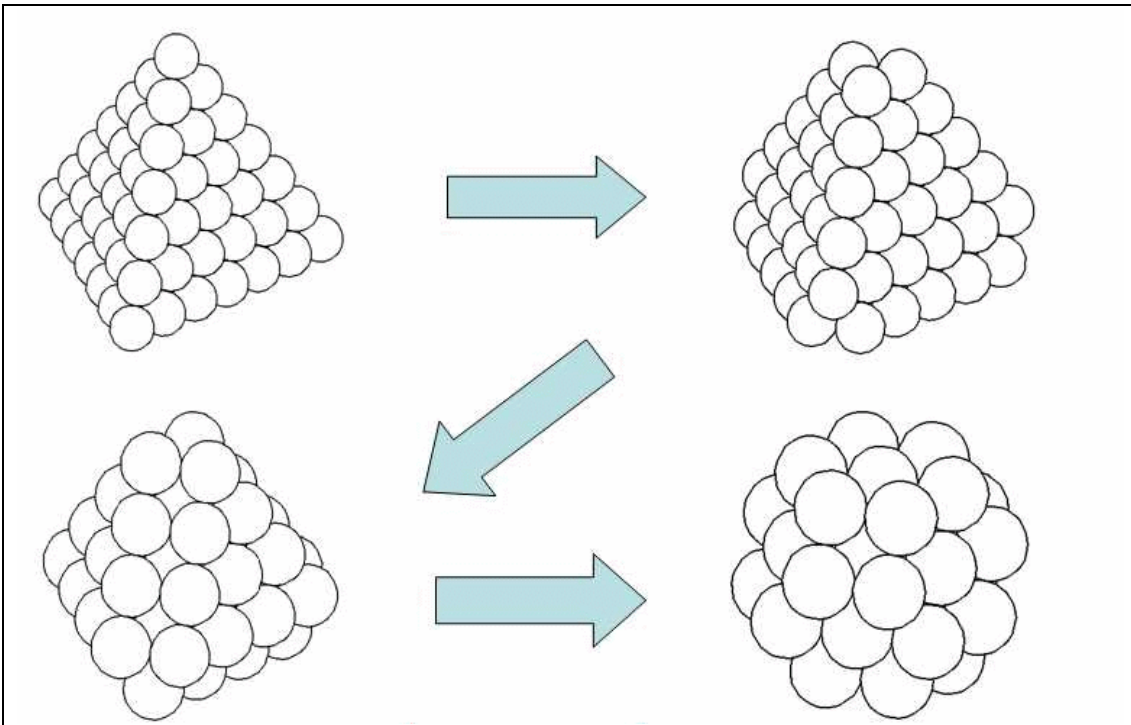


**Fig D-6** : The process of cutting bulk. ( sphere instead of a unit CdSe tetrahedron )

## Reference

- [1] A. V. Baranov, Yu. P. Rakovich\* and J. F. Donegan, T. S. Perova and R. A. Moore, Phys. Rev. B, 68. 165306(2003).
- [2] Robert W. Meulenberg and Geoffrey F. Strouse, Phys. Rev. B, 66. 035317(2002).
- [3] Robert W. Meulenberg, Phys. Rev. B, 70. 235311(2004).
- [4] Eiichi Hanamura, , Phys. Rev. B, 38. 2 (1988).
- [5] W. Shan, W. Walukiewicz, J. W. Ager III, K. M. Yu, and J. Wu, Appl. Phys. Lett.84, 94720(2004).
- [6] Yufeng Zhao, Yong-Hyun Kim, Mao-Hua Du, and S. B. Zhang, Phys. Rev. Lett. 93, 015502(2004).
- [7] Pingrong Yu, Matthew C. Beard, Randy J. Ellingson, Suzanne Ferrere, Calvin Curtis, J. Phys. Chem. B 2005, 109, 7084-7087
- [8] Konstantin B. Shelimov, Rinat O. Esenaliev, Audrew G, Rinzler, Chad B. Huffman, Richard E. Smalley, Chem. Phys. Lett. 282, 429(1998).
- [9] S. Bandow, S. saka, X. hao, Y. Audo, Appl. Phys. A, 67, 23(1998).
- [10] X. Zhao, M. Ohkohchi, M. Wang, S. Iijima, T. Ichihashi, Y. Ando, Carbon, 35, 775, 1997.
- [11] N. Hamada, S. Sawada, A. Oshiyama, Phys. Rev. Lett. 68, 1579(1992).
- [12] R. Saito, M. Fujita. G. Dresselhaus, M. S. Dresselhaus, Appl. Phys. lett. 60, 2204(1992).
- [13] Minami, N. , Kazaoui, S. Jacquemin, R. Yamawaki, H. Aoki, K. Kataura, H. Achiba, Y. , Synthetic Metals 116, no. 1-3 405(2001).
- [14] Odom, T. W. J-L, Huang, Kim, p. Lieber, C. M. , Nature, 391, no 6662, 62-4, 1998.
- [15] C. L. Kane, E. T. Mele, Phys. Rev. Lett. 78, 1932(1996).
- [16] M. Verissimo-Alves, R. B. Capaz, B. Koiller, E. Artacho, H. Chacham, Phys. Rev. Lett. 86, 3372(2001).
- [17] B. Ruzicka, L. Degiorgi, Phys. Rev. B, 61. 2468(2000).
- [18] A. G. Tinzler, J. Liu, H. Dai, P. Nikolaev, C. B. Huffman, F. J. Rodriguez-Maceas, P. T. Boul, A. H. Liu, D. Heymann, D. T. Colbeot, R. S. Lee, T. E. Fischer, A. M. Rao, D. C. Eklund, R. E. Smalley, Apply. Phys. A, 67,



29(1998).

[19] S. Kazaoui, N.Minami, R. Tacquemin, Phys. Rev. B, 60, 13339(1999).

[20] A. Ugawa, A. G. Rinzler, D. B. Tanner, Phys. Rev. B, 60, R11305(1999).

[21] S. Rols, Z. Beues, E. Anglaret, T. C. Sauvajol, D. Papauelc, J. E.

Fescher, G . Coddens, H.Schober, A. J. Dianoax, Phys. Rev. Lett. 85, 5221(2000).

[22] T. Pichler, M. Knupfer, M. S. Golder, J. Fink, Phys. Rev. Lett, 80, 4729(1998).

[23] Physical Properties of Carbon Nanotubes, p11 (R. Saito, G.Dresselhaus, M. S. Dresselhaus, 1998).

[24] O. Jost, A. A. Gorbunov, W. Pompe, Appl. Phys. Lett. 75, 2217(1999).

[25] R. Saito, M. Fujita. G. Dresselhaus, M. S. Dresselhaus, Appl. Phys. lett. 60, 2204(1992).

[26] N. Hamada, S. Sawada, A. Oshiyama, Phys. Rev. Lett. 68, 1579(1992).

[27] C. L. Kane, E. T.Mele, Phys. Rev. Lett. 78, 1932(1996).

[28] T. Pichler, M. Knupfer, M. S. Golder, J. Fink, Phys. Rev. Lett, 80, 4729(1998).

[29] F. Bommeli, L. Degiorgi, P.Wachter, W. S. Bacsa, W. A. de Heer, and L. Forro, Solid State Cmmun. 99, 513 (1996).